UNCONVENTIONAL ORDERING IN CORRELATED FERMI LIQUIDS AND GASES

a dissertation

by

JASON JACKIEWICZ

submitted in partial fulfillment of the requirements
for the degree of

Doctor of Philosophy
(Physics)

at

BOSTON COLLEGE

The Graduate School of Arts and Sciences

Department of Physics

August 2005

To my parents, for their undying selflessness, generosity, patience, and love.

ACKNOWLEDGMENTS

There are so many people to thank for all of their help and friendship throughout the years in making this modest dissertation possible (modest because of my limited capabilities, not theirs). I am unfortunately unable to acknowledge everyone, but they know who they are, and therefore, I will mention just a few names.

I thank my fellow graduate students, present and past, for all of the fun carousing about Boston and the physics-less conversations we have had over the years.

I thank the late Grant Balkema for allowing me to learn from his well-rounded knowledge of everything under the sun, and for allowing me to observe his wonderful, compassionate teaching style. He is dearly missed.

I thank heartily the physics department office staff, which has changed quite a bit over the years. In particular, I acknowledge Joan and Karen for just being good friends (and telling me all the gossip in the department). You are the hardest working people in the department by far, and I appreciate all the things you have done for me.

I acknowledge all of the professors in the Boston College physics department, and thank them for the help and insight they have provided me. I am eager and graciously awaiting one day to have them as distinguished colleagues.

I truly want to thank the rest of the Bedell family: Carmen, Christopher, (and Simba), for inviting me into their home many times and treating me with such kindness. I will miss our get-togethers very much, and hope that in the near future we may have time together again.

I give very special thanks to my advisor, more importantly my friend, Kevin Bedell. I think a great testament to his influence and guidance is that all of his students tend to take on an aspect of his calm personality and sharp physical insight, and I would be honored if I have done so as

well. He has taught me not only a lot of physics, but also how to present one's ideas to others. His generosity has played the biggest part in allowing me to complete this doctoral degree and begin my career, and I will always be indebted to him.

Finally, I want to thank Sara Youngblood Jackiewicz, not only for adamantly revising and editing this thesis to bring it from a mess of words to something legible, but more significantly, for giving me all the motivation in the world for getting it completed so that we could move on and live our lives together. Without her, I would not have been able to finish this research. Her love and support will always be reciprocated.

TABLE OF CONTENTS

Page

LIST OF TABLES

LIST OF FIGURES

Figure Page

Appendix
Figure Page

Appendix
Figure Page

Appendix
Figure Page

Appendix
Figure Page

UNCONVENTIONAL ORDERING IN CORRELATED FERMI LIQUIDS AND GASES

JASON JACKIEWICZ

Under the supervision of Department Chairperson Kevin S. Bedell

At Boston College

ABSTRACT

In this thesis I study the roles of magnetic and superconducting phenomena in strongly correlated electron systems. Much of the focus is on the coexistence of ferromagnetism and superconductivity which has only been experimentally observed in the last five years. Therefore, most of the theoretical work presented here is directed towards elucidating the current experiments and predicting the results of future ones.

I will review the history of this rich field in both theoretical and experimental frameworks, and try to cast light on the various viewpoints that are held with respect to the phenomenon of coexistent superconductivity and ferromagnetism. In that regard, I will argue that a theory based on s-wave superconductivity is quite relevant and explains several important experiments, and cannot be discounted from explaining several more, particularly in the case of the well-studied material UGe_2.

The theoretical foundation used in this thesis to examine UGe_2, in particular Fermi liquid theory, is then applied to the intriguing ultracold Fermi gases. These materials are quite rich experimentally, and the fundamental quantum physics that they display, such as matter waves and Bose-Einstein condensation, is amenable to theoretical calculations. The results of the study of these gases in our model will be shown to agree very well with many of the experimental observations that have until now not been understood thoroughly.

ABSTRACT

In this thesis I study the roles of magnetic and superconducting phenomena in strongly correlated electron systems. Much of the focus is on the coexistence of ferromagnetism and superconductivity which has only been experimentally observed in the last five years. Therefore, most of the theoretical work presented here is directed towards elucidating the current experiments and predicting the results of future ones.

I will review the history of this rich field in both theoretical and experimental frameworks, and try to cast light on the various viewpoints that are held with respect to the phenomenon of coexistent superconductivity and ferromagnetism. In that regard, I will argue that a theory based on s-wave superconductivity is quite relevant and explains several important experiments, and cannot be discounted from explaining several more, particularly in the case of the well-studied material UGe_2.

The theoretical foundation used in this thesis to examine UGe_2, in particular Fermi liquid theory, is then applied to the intriguing ultracold Fermi gases. These materials are quite rich experimentally, and the fundamental quantum physics that they display, such as matter waves and Bose-Einstein condensation, is amenable to theoretical calculations. The results of the study of these gases in our model will be shown to agree very well with many of the experimental observations that have until now not been understood thoroughly.

Chapter 1

Introduction

As early as the 1950's, when the Bardeen-Cooper-Schrieffer (BCS) [13] theory of superconductivity (SC) was still being formulated and ferromagnetic correlations in solids were being treated in a (Weiss) mean-field manner, theories about the competition and/or coexistence of these two phenomena in materials had begun surfacing [14]. This is somewhat surprising given that it had always been taught and known that magnetic fields always suppress superconductivity. Nevertheless, proposed theories and speculations continued in the following decades but it was not until around 2000 when superconductivity and ferromagnetism were found to coexist in the material UGe_2 [15]. Superconductivity had not yet been observed in UGe_2 because it does not become superconducting until the temperature is lowered below about $0.7K$ at an optimal pressure of $13kbar$, experimental conditions only available in the best laboratories. Following this discovery, SC was also found to coexist with ferromagnetism (FM) in the well-known compound $ZrZn_2$ and also in $URhGe$ [4, 16].

This brief introduction will focus on the history of the physics of the magnetic ordering in itinerant ferromagnetic metals and the interplay with superconductivity. Itinerant ferromagnetic systems are somewhat more complex than ferromagnetic insulators in that there are extra degrees of freedom due to charge mobility, however Fermi liquid theory has successfully dealt with these systems for several decades. For a nice review of antiferromagnets coexisting with superconductivity, especially in the high temperature superconductors and certain heavy fermion systems like $CePd_2Si_2$ and $CeIn_3$, see [17] and references therein.

1.1 Early theories

One of the first people to look at the ferromagnetic-superconducting possibility was Ginzburg [14] in the Soviet Union, simultaneously with the development of the BCS theory of superconductivity in the late 1950's . The concept of superconductivity that Ginzburg was working with was that due to the London brothers mainly [18], which dealt with the electrodynamics of superconductors, particularly the behavior of a magnetic field response [19]. He also utilized his theory of phase transitions developed at that time in collaboration with Landau [20]. He considered the question of how an internal magnetic field could disrupt or promote superconductivity in a thin film. The issue considers the important relation between an internal field and the critical external field H_c of a superconductor. The work of Clogston [21] gives us some answers to this problem, as will be shown later.

Once it was realized that it was possible that Cooper pairing could come from non-phononic sources, unlike in the conventional BCS superconductors, there were theories put forth of spin fluctuation mediated superconductivity by Berk-Schreiffer and Doniach-Engelsberg [22, 23]. The focus of this work was to show that in certain transition metals, the paramagnetic susceptibility is strongly enhanced indicating strong ferromagnetic exchange forces. They thus argued that s-wave pairing is highly unlikely since most spins are aligned rather than anti-aligned, leaving the possibility open for triplet pairing.

In the late 1970's, Enz and Matthias were studying the weak ferromagnet $ZrZn_2$ [24] and predicted that p-wave triplet superconductivity should be observed. Fay and Appel [25] looked at this closely alongside the previous work by Berk-Schrieffer mentioned above. Using the random-phase approximation (RPA), they found that the exchange of longitudinal spin fluctuations near a magnetic critical point leads to attractive p-wave coupling. The equal spin pairing (ESP) that they considered is like the A1 phase of Helium-3 in a magnetic field. The calculations predicted the existence of p-wave superconductivity on both sides of the transition, i.e., in the paramagnetic phase *and* in the ferromagnetic phase, with a critical temperature T_C for the SC higher on the paramagnetic side. See Figure 1.1 for an explanation.

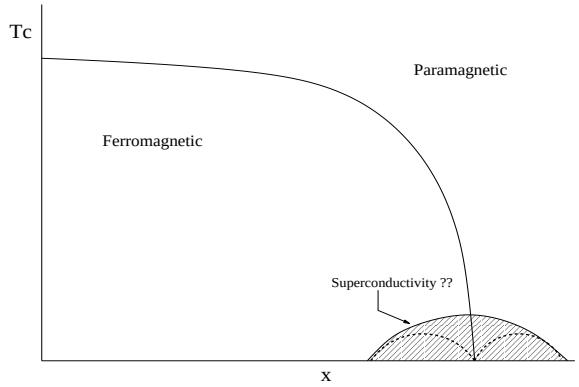

Figure 1.1 A generic phase diagram for some of the theories discussed in the text. T_c is the critical (Curie) temperature of the magnetization and x can be any control parameter, usually pressure or density. The superconducting dome may come in many shapes and sizes, and the ones shown here are just examples. One theoretical prediction, denoted by the dotted line is the SC dome being suppressed at the $T = 0$ magnetic transition, giving 2 domes, one on either side, likely having different maximal T_c's (not shown here) as in the Fay/Appel theory.

Another important contribution to the theory of ferromagnetism was made in 1976 by Hertz using a Renormalization Group (RG) approach at zero temperature [26]. This handled the fluctuations around the critical point of a continuous magnetic phase transition in an itinerant ferromagnet in a consistent manner. Later, Millis extended this theory to account for finite temperatures [27]. These complimentary papers studied the behavior of the order parameter as it goes to zero at a quantum critical point, and are the foundations of the coexistent theories that came about later when superconductivity was considered, as will be seen below.

The future Nobel laureate A.A. Abrikosov had also published calculations in which he considered superconductivity arising within a background of ferromagnetic ordering [28]. He showed that coexistence of SC/FM can indeed occur for certain values of the coupling parameters, and his model is somewhat similar to the one which will be studied here. The main difference between Abrikosov's model and the one studied in this thesis, is that he did not consider the order parameters as being 'coupled', and the equations therefore were not solved self-consistently as we have done. [1]

[1] He did actually admit this fact to us on a visit to Boston College.

1.2 More daring theories and experimental triumph

In 1984, a paper by Lei *et al*. [29] entertained a mean-field model of coexistent s-wave singlet superconductivity and ferromagnetism. In this paper they predicted that the BCS state or the ferromagnetic state are independently the most energetically favorable ones, never the coexistent state.

Then, in the late 1990's, two papers by Blagoev *et al*. showed, using Fermi liquid theory, that under certain circumstances, s-wave superconductivity can arise within a ferromagnetic background [5, 7]. The results are exact only if the liquid is *local* and that the temperatures are low enough. In this approximation, *only* s-wave SC is possible, and the pairing amplitude for triplet SC is strictly zero.

Around this time, almost all theories posited that if superconductivity was to be found in the weak ferromagnetic systems, it would most likely be in the paramagnetic state. Hence, most experiments looked in that region. It had been known for a while that in some systems like $ErRh_4B_4$ and $HoMo_6S_8$, superconductivity was suppressed as soon as ferromagnetic order set in, so these two phases seemed exclusive and incompatible. The big surprise was that SC was finally found on the *ferromagnetic side* - in UGe_2! Then, soon after, the same general phenomenon was found in two more materials, $ZrZn_2$ and $URhGe$.

1.3 *S*-wave supporters and *p*-wave *p*roponents

The theoreticians then went to work. The ones predicting p-wave superconductivity, which was the majority, could not reconcile why the SC did not show up on both sides of the ferromagnetic-paramagnetic transition. Their theories worked to predict it in the FM, but always allowed and/or demanded it on the other side as well, albeit sometimes with a lower T_C, such as in Figure 1.1. For instance, using strong-coupling Eliashberg theory, it can be shown that the p-wave triplet superconducting critical temperature is slightly higher on the ferromagnetic side than on the other side, due to coupling enhancement with the transverse spin fluctuations [30, 31, 32]. However, the T_c is expected to remain finite even at the critical magnetic point. An important point to mention

is that the theory makes predictions assuming a *continuous* magnetic transition, so its application to a material such as UGe_2, which is first order (as explained later), may not be accurate.

Using a more elaborate field-theoretic treatment, Kirkpatrick and others have obtained essentially the same results as above, in that they show how the ferromagnetic state is more conducive to triplet superconductivity [33, 34]. Another prevailing model incorporates the Ginzburg-Landau theory of phase transitions with a group-theoretical treatment of the nature of the SC order parameter, which in these cases is constructed as a triplet. The critical temperatures are then readily calculated. This treats the coexistence in UGe_2 [35], and in $ZrZn_2$ [36]. For $ZrZn_2$, some theorists argue that the stabilized state is due to an exchange interaction between the magnetization density and the magnetic moments of the triplet Cooper pairs. Also, an LDA+U band structure calculation has a been done for UGe_2, and it shows that the coexistence could be due to a quasi-2D sheet of the Fermi surface, consisting of mostly majority spins that would seem to favor triplet SC pairing [1].

However, there were a few theorists who predicted singlet s-wave SC in these weak ferromagnets. The first paper of this cabal was one by Karchev *et al*. [37], who was motivated by the earlier papers of Blagoev mentioned above. They constructed a mean-field model of a single band ferromagnetic superconductor. The Karchev theory supposes that the electrons responsible for the ferromagnetism are the same as those that contribute to the superconducting pairing, an idea suggested by the experimental evidence in UGe_2 that shows the ferromagnetism and the superconductivity arising at exactly the same point, i.e., at $T \approx 0$ and at a critical pressure p_c. A detailed analysis of this model will be given in Chapter 3.

Two other very interesting papers were published in that same year that also advocated s-wave superconductivity. Harry Suhl [38] proved that under certain conditions (low T, large effective mass) in a system that exhibits an inverse RKKY-like behavior, i.e., where one localized magnetic spin can mediate the interaction of two conduction electrons instead of vice-versa, these two said electrons can attractively bind to form a singlet Cooper pair. Shortly thereafter, Abrikosov, motived by Suhl's idea, showed that if one sums up all of the spins and conduction electrons, the entire system is unstable to s-wave superconductivity, and becomes a ferromagnetic superconductor [39].

He was also motivated by the fact that UGe_2 retains its superconductivity even in a dirty polycrystalline sample [40], indicating a very noteworthy characteristic of only s-wave superconductors. Another recent paper [41] by Cuoco et al. takes an approach similar to Karchev in that it is mean-field and single band, arguing that the most favorable ground state is the s-wave/ferromagnetic one (compared to the pure ferromagnetic or pure BCS or the normal state), and that the ferromagnetism is due to a kinetic exchange mechanism. The model shows that a tuning of the effective masses, or bandwidths, of the minority and majority spin species lowers the kinetic energy while gaining condensation energy, producing a stable SC/FM state.

What this thesis aims to show in part is that considerations need to be taken for *all* of the possibilities mentioned above to make the case that further experimentation needs to be carried out, but that there are convincing arguments that the SC pairing symmetry is specifically s-wave in nature.

The remainder of the thesis will be organized as follows: Chapter 2 will review with some of the general experimental data that have been published over the last few years concerning weak ferromagnets and coexistent FM/SC systems. The details of certain measurements will later be compared to our theoretical work, particularly in UGe_2. More data and analysis will be introduced in the corresponding chapters as well. Then Chapter 3 will contain the solution of the mean-field model mentioned above and its various comparisons with the experimental data. I will also include some detail as to how this model came to be from earlier work. Chapter 4 includes more calculations dealing with another seemingly general aspect of the weak ferromagnets - that they display first-order phase transitions at low temperatures and high pressures. To study this we employ some ideas from the 1960's that were applied to nuclear matter by Gerald Brown and later Kevin Bedell and collaborators. The simplicity of these techniques and the fact that they yield non-trivial results make it a very convenient way to look at many similar systems. Then a very short chapter is included on recent work that predicts in a general way a spin-density wave/charge-density wave transition in weak ferromagnetic metals based on the local Fermi liquid ideas, and in light of recent experiments. Finally, in Chapter 6, the discussion is turned towards the topic of atomic physics, and the study of ultracold, dilute Fermi gases that display Bose-Einstein condensation *and*

BCS superfluidity, with just a simple sweep of an external magnetic field. The theory developed in Chapter 4 will be modified slightly and applied to these systems and compared to several recent experiments.

Chapter 2

Experiments

In this chapter three materials will be examined that generally show robust coexistence of superconductivity and ferromagnetism: UGe_2, $ZrZn_2$, and $URhGe$. These are the only materials that exhibit this bulk phenomenon so far, and I would like to categorize some of their unique physical properties. I will cover UGe_2 in more detail than the other two since it has received the most experimental attention recently and there is a wealth of good data available. Even though these materials have been studied for a long time, I will focus on the developments of the past five years or so on the crystals in which the coexistence was first observed. Therefore, I will not provide a comprehensive experimental history, but one that is pertinent to the theories to come later.

2.1 $\mathbf{UGe_2}$

The experimental data shown here are mainly taken from refs. [2, 15, 40] and the references within these. I will not cite each one specifically unless where appropriate, since they are all in relative agreement except for the polycrystalline sample studied in reference [40].

2.1.1 Crystal structure

The crystal structure of UGe_2 is base-centered orthorhombic and it has full inversion symmetry. A drawing of this structure is shown below. Inversion symmetry basically means that the environment around a point (x, y, z) in the crystal is the same as that around a point $(-x, -y, -z)$. There is also a very high magnetocrystalline anisotropy, two orders of magnitude stronger than in

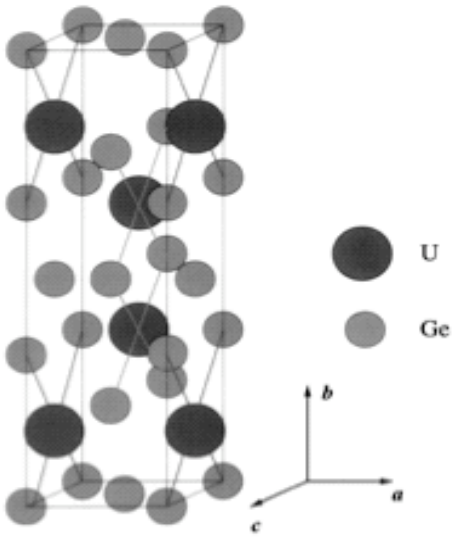

Figure 2.1 Crystal structure of UGe_2 for two primitive cells, adapted from ref. [1].

most transition metal magnets, with the easy axis of magnetization along the $\hat{a}$ direction of the figure.

2.1.2 Electronic properties

In most compounds that contain uranium we find large effective masses of 100 to 1000 times the electron mass, such as in UPt_3, and these are called heavy fermion systems. UGe_2, on the other hand, has a measured effective mass of about $20m_e$. Thus, the 5 f-electrons of uranium that are usually highly localized and 'heavy' have more of an itinerant character, as in $3d$-electron transition metals. This is an extremely important property because the magnetization cannot be looked at in a local moment sense, and because the mobility or hybridization of these magnetic electrons gives them the opportunity to form the superconducting Cooper pairs. Furthermore, the ferromagnetic state has an ordered moment of $1.4\mu_B/U$, while the paramagnetic state has an effective moment of $2.7\mu_B/U$, typical of the observed behavior in $3d$ magnetic metals. The calculated paramagnetic moment for an isolated atom has a value of $3.62\mu_B/U$, much higher than the observed one in UGe_2, which further proves that the real system has a strong hybridization with conduction states.

The phase diagram of UGe_2 is shown in Figure 2.2. One important feature is that there is no superconductivity at ambient pressure where the Curie temperature T_c is about $54K$. As the pressure is increased to $8 - 9kbar$ the first signs of superconductivity become apparent and the SC is strongest at about $11kbar$ with a $T_{sc} \lesssim 1.0K$. On further increasing the pressure, the superconductivity is suppressed along with the ferromagnetism and they both disappear at a pressure of $\sim 16kbar$, giving way to the paramagnetic state. Currently, there appears to be a consensus that the coexistent phase is a homogeneous bulk phenomenon, one reason being that neutron studies inside the SC dome have shown robust ferromagnetic order [42].

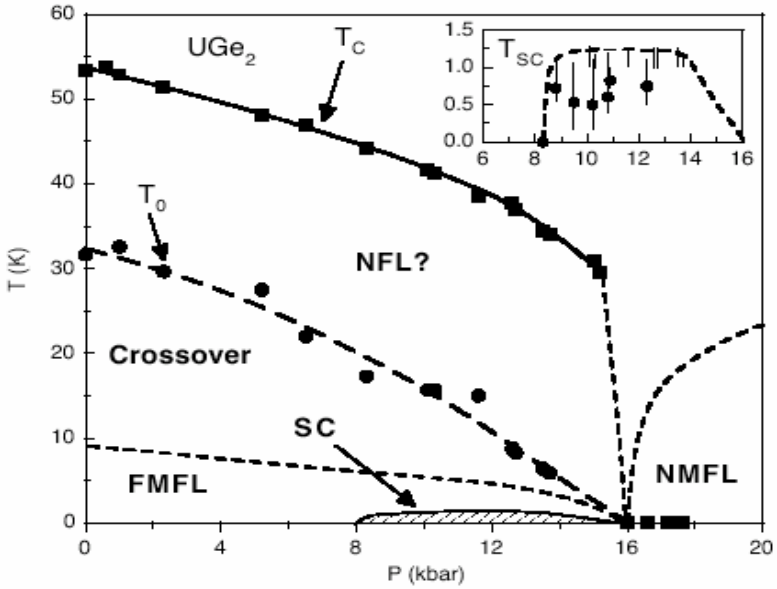

Figure 2.2 Phase diagram of UGe_2 taken from ref. [1]. This was measured on a polycrystalline sample, but has the same overall features as the single crystal phase diagram. The inset shows the superconducting transition temperature (filled circles) versus pressure.

As will be seen in section 2.1.5, the magnetic transitions in the high pressure regime are actually first order phase transitions. Also in that section, it will be shown that the temperature scale set by T_0 in Figure 2.2 is not only a crossover from a Fermi liquid to a non-Fermi liquid, but also one from a large moment ferromagnet to a small moment ferromagnet. Furthermore, there is strong evidence from recent experiments that the T_0 line is only an experimental artifact of something else, and that at slightly lower temperatures there is a real spin density/charge density wave transition.

Another important signature of the superconductivity is the electronic specific heat, shown in Figure 2.3 for a single crystal sample.

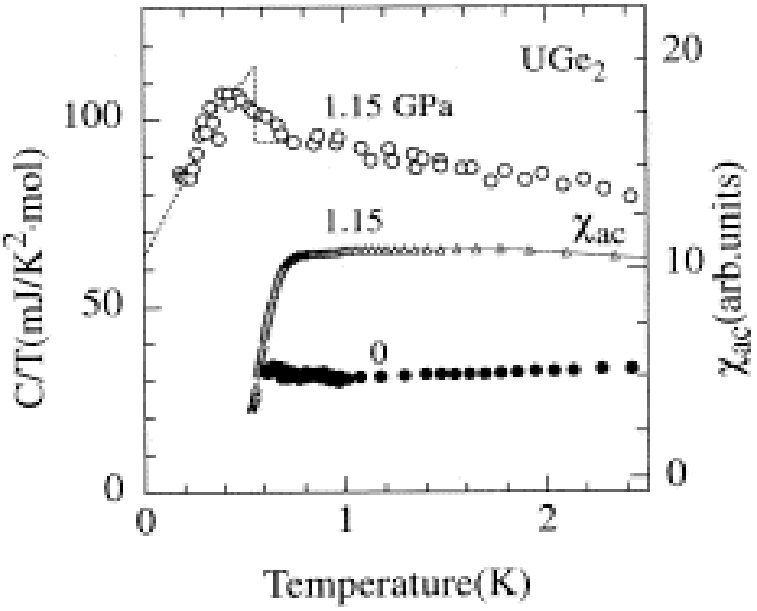

Figure 2.3 Specific heat of UGe_2 from ref. [2]. The pressure of $1.15GPa = 11.5kbar$ is just below the pressure at which T_{sc} is maximal. Also shown on the right hand scale is the ac susceptibility at this high pressure and at ambient pressure, indicating the superconducting diamagnetic response (Meissner effect) at the transtition temperature.

In a BCS superconductor, the jump in the specific heat is $(C_{sc}-C_n)/C_n = \Delta C/\gamma T_{sc} = 1.43$, or 143% ($\gamma = 2\pi^2/3N(0)k_B^2$). One sees that the jump in UGe_2 is much smaller, about $20-30\%$. This could be explained if there is a finite density of states at the Fermi level, i.e., gapless excitations where $N(0) \neq 0$, which do not exist in the BCS theory since all of the quasiparticles are gapped at E_F. One scenario for this to occur is if the SC order parameter is p-wave with nodes on the Fermi surface which would give a finite DOS in the gap. We will show in our theoretical treatment that a finite density of states can also arise from a particular s-wave model, and these extra quasiparticles do not take part in Cooper pairing. The large value of γ, the coefficient of the linear term in the specific heat $\gamma = C/T$ should also be noted. At ambient pressure $\gamma(P = 0) = 30mJ/K^2$, and as shown above, $\gamma(P = 11.3kbar) \approx 70mJ/K^2$. These large values are a characteristic of a somewhat heavy fermion system.

2.1.3 Crossover anomaly or spin-density wave?

An interesting feature of the phase diagram in Figure 2.2 is the line labeled by the temperature $T_0 \simeq 0.6T_c$ at zero pressure. It separates the ferromagnetic Fermi liquid (FMFL) and crossover region from the non-Fermi liquid (NFL) region. A Fermi liquid shows a temperature-dependent resistivity of the form

$$\rho(T) = \rho_0 + AT^n, \tag{2.1}$$

where $n = 2$ and A is a measure of the scattering of conduction electrons. In the FMFL and non-magnetic Fermi liquid (NMFL) regions, the exponent is exactly 2 for temperatures up to about $20K$ for $P = 0$ and $P \gtrsim P_c$. It is important for our theory that at low temperatures there exists a Fermi liquid. As the temperature is raised and/or the pressure is increased, the exponent n slowly decreases from its Fermi liquid value to $n = 1.5$ in the non-Fermi liquid region. At higher pressures, the crossover temperature is reduced to about $8K$ at the pressure where T_{sc} is maximal (p_x) in the polycrystal, and to near zero temperature in the single crystal at p_x [15, 2].

Possible explanations for this are limited, but I will posit one here. One prior scenario was that a charge-density wave or spin-density wave forms because the Fermi surface shape is prone to nesting [43], but this had been shown erroneous because no magnetic signature such as static order is observed that would indicate this. Also, as will be seen in section 2.1.5, there is some evidence that it has to do with the behavior of the magnetic moment [3]. Recently however, an experiment shows a well-defined transition at about $22K$, never seen before due to the very slow cooling rates in this experiment. We believe that in fact it is a spin or charge-density wave as has been suggested for some time now, but just in a different region than originally considered. A short explanation of this is provided in Chapter 5, and a publication is forthcoming [44].

2.1.4 Single vs poly crystal

Studying the differences in the measurements on single crystals and polycrystals could give important insights into the superconducting order parameter symmetry. It is well known that defects and impurities strongly suppress superconductivity in systems that have odd angular momentum

pairing, i.e, $l = 1, 3, ...$ (p-wave, f-wave, ...). On the other hand, isotropic, or s-wave pairing is rather unaffected by such pair-breaking mechanisms for reasonable concentrations. Table 2.1 shows some important information on two different samples of UGe_2.

$\mathbf{UGe_2}$	$T_c(P=0)$	$P_c(M \to 0)$	SC range	$\rho_0(\mu\Omega cm)$	max T_{sc}
single crystal	$53K$	$16-17kbar$	$10 \lesssim P \lesssim 15kbar$	≈ 0.26	$\approx 0.8K$
polycrystal	$54.5K$	$16kbar$	$8.8 \lesssim P \lesssim 14kbar$	$1-3$	$0.5 \sim 0.8K$

Table 2.1 Comparison of values for a single and poly crystal of UGe_2.

What one notices immediately is that there is not really much difference between the single or the polycrystal for the values of the critical temperatures, which is a particularly important fact for T_{sc}, even though the residual resistivities ρ_0 can differ by as much as an order or magnitude. This observation is what led Abrikosov [39] to claim that the superconductivity must be s-wave.

More quantitatively, the usual criterion for establishing say, the likelihood of s-wave or p-wave SC, is the ratio of the superconducting coherence length ξ and the electron mean free path l. For systems with a long mean free path and a small coherence length, i.e., a 'clean' superconductor where $\xi/l \ll 1$, p-wave is possible. An example of this is Sr_2RuO_4 [45]. For the other limit when $\xi/l \gtrsim 1$, s-wave symmetry is much more likely than p-wave. One quick way to calculate the mean free path l is from the formula [46]

$$l = \frac{3}{e^2 N(E_F) v_F \rho_0}, \tag{2.2}$$

which holds for a spherical Fermi surface (which is not the case in UGe_2, but we are taking a first guess). This gives $l \sim 150$Å for $\rho_0 = 1\mu\Omega cm$. A more accurate way to determine the mean free path is from de Haas-van Alphen measurements which have yielded an $l \sim 300$Å; however, at a somewhat lower pressure than where ρ_0 is largest and SC is still present (see [40] for a discussion). For the single crystals, the mean free path has been estimated at $1300-1400$Å. From upper critical field measurements, the superconducting coherence length is estimated at $\xi = 130 - 200$Å, which

is calculated from the formula

$$H_{c2} = \frac{\Phi_0}{2\pi\xi^2}. \tag{2.3}$$

So for the single crystal, $\xi/l \ll 1$ and the circumstances for p-wave pairing are surely possible; but as the sample gets dirtier, the mean free path gets reduced by about an order of magnitude, and as seen in the table, T_{sc} hardly is affected. This leads one to believe that only an s-wave pairing symmetry could survive such an increase of the ξ/l ratio, especially when one considers that the (supposed) p-wave SC is completely suppressed in Sr_2RuO_4 when a similar change in this ratio is observed after impurity doping [45].

2.1.5 First order transitions

One final very interesting property that has been observed quite clearly in UGe_2 has to do with the magnetic phase transitions for small temperatures and large pressures. It had previously been suspected that the transitions from the ferromagnetic to the paramagnetic phase were of first order at p_c in the limit of $T \to 0$ [15]. This has been verified by recent experiments, and is also true at low but finite temperatures [3]. In addition, it is seen that there is another set of first order transitions from a large magnetic moment (FM2) to a smaller magnetic moment (FM1) *within* the ferromagnetic phase. This transition corresponds to the crossover phase referred to earlier in section 2.1.3. Details can be seen in Figure 2.4.

These experiments distinctly show the magnetic moment discontinuously changing at two different pressures corresponding to p_x and p_c (it can also be observed when the pressure is fixed and the temperature is varied). The crossover temperature T_x (previously mentioned as T_0) approaches zero at p_x which is precisely the pressure at which T_{sc} is largest (this data is from single crystal measurements - it is not clear what happens to T_x in the polycrystal at very low T). Thus, it has been postulated that the superconductivity is highly correlated with this crossover scale, in fact, the superconducting transitions are much sharper for $p_x < p < p_c$. I will not address this aspect here, however in Chapter 4 I present a theory that yields a first order phase transition, and its implications are very important also for the superconductivity. It must be noted that there has been a theoretical attempt to explain these experiments that uses a band structure argument to show how

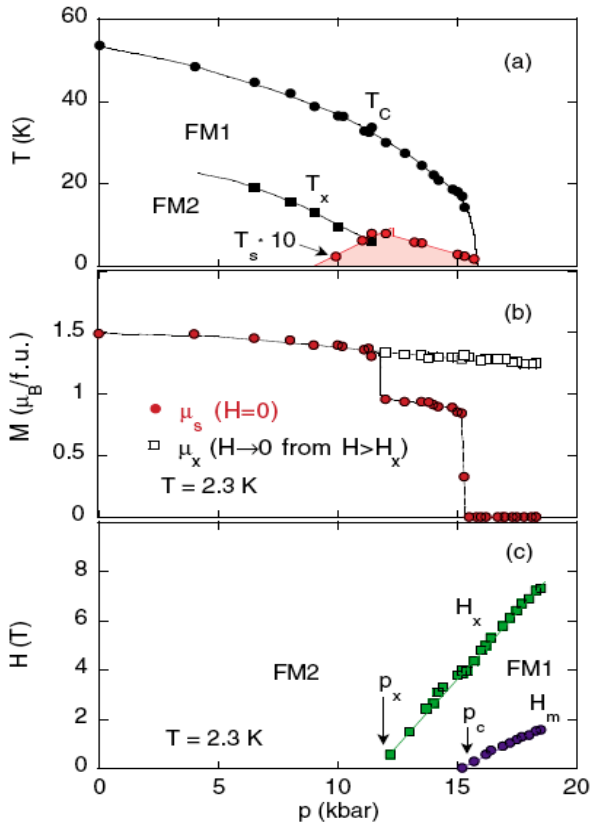

Figure 2.4 Magnetic behavior of UGe_2. (a) Shows the phase diagram with the large (FM2) and small (FM1) moment regions labelled. (b) Two first order transitions in the magnetization as the pressure is increased, from FM2 to FM1, and then from FM1 to a paramagnet. (c) The behavior of p_x and p_c with an external field present. Taken from ref. [3].

two first order phase transitions can arise [47]. The authors use a zero temperature Stoner model with a double-humped density of states that is tuned by the magnetic coupling constant to give the requisite jumps in the magnetization.

2.2 $ZrZn_2$

Another material that has received much experimental attention but had never been observed to be superconducting is $ZrZn_2$, a weak itinerant ferromagnet in which none of its constituents are actually ferromagnetic on their own. It had been postulated to be an excellent candidate for

displaying p-wave superconductivity [24], but it was not until 2001 that this was discovered, co-existent with the magnetism [4]. The itineracy is manifest in the Zr 4d-electons, which makes it already a very different system than UGe_2 which has f-electron character. It also is a weaker ferromagnet, with an ambient Curie temperature of about $29K$ and a moment of only $0.17\mu_B/f.u.$.

The most striking difference between $ZrZn_2$ and UGe_2 is that in the former the superconductivity spans the whole pressure range, i.e., for $0 \leqslant P \leqslant P_c$, which is seen in its phase diagram in Figure 2.5.

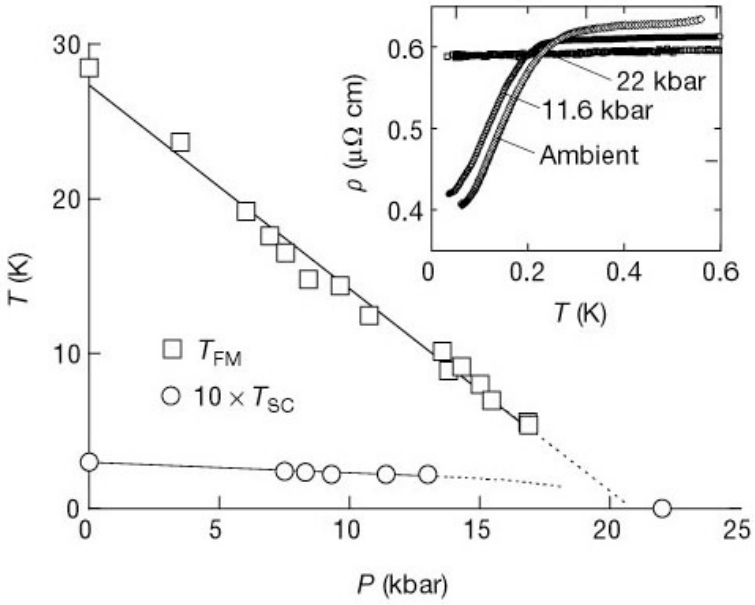

Figure 2.5 Phase diagram for $ZrZn_2$ from ref. [4]. The inset shows the resistivity for different pressures.

The key to the superconductivity in $ZrZn_2$ is the purity of the crystal, and the crystal that becomes superconducting has a residual resistivity of $\rho_0 = 0.62\mu\Omega cm$, while samples of five times this value show no superconductivity whatsoever. This sensitivity to impurities makes it a strong candidate for p-wave pairing, and in fact the mean free path is several times as large as the coherence length, and the ratio $\xi/l \ll 1$ thus allows for this possibility. A theory invoking the p-wave triplet scenario and using a Ginzburg-Landau mean-field analysis was recently shown to reproduce the phase diagram shown above quite well [36]. There is, however, still a question as to whether the superconductivity is a robust bulk property of the material since a jump in the specific

heat has not been observed. Since the SC has so far only been seen in one single crystal, it is still too early to make any definite proclamations, and with newer and cleaner samples currently in production, we will have to wait for further experiments to verify this phenomenon. At the moment, the consensus is that the superconductivity can be described accurately as being inhomogeneous [48].

2.3 URhGe

The last material I will mention very briefly in this experimental introduction is the superconducting ferromagnet $URhGe$. Unfortunately, there have not been studies of the superconductivity at high pressures as in the other two systems, but at ambient pressure it is found that $T_{sc} = 0.25K$ [16]. It does appear to be bulk superconductivity because there is a definite specific heat increase as the temperature is lowered below T_{sc}, yet it is lower than the BCS value. As in many other uranium based compounds, the specific heat coefficient γ is large $\sim 160mJ/K^2$ in the normal state, indicating its heavy fermionic nature. It is assumed that the coexistent phase diagram will evolve similarly to what we have seen in $ZrZn_2$ as more experiments are performed at high pressures (there are ones looking solely at the FM order in a very similar compound [49]).

In summary, I would like to present a reference table to the various experimental quantities of these three important materials which will be referred to throughout the text.

	$\mathbf{T_c}(K)$	$\mathbf{T_{sc}}(K)$	$\mathbf{P_c}(kbar)$	$\mathbf{\Delta C/C}$	$\mathbf{H_{c2}}(T)$	$\xi(\mathring{A})$	$\mathbf{M}(\mu_B/f.u.)$
$\mathbf{UGe_2}$	53	0.8	17	$0.2-0.3$	1.9	130	1.4
$\mathbf{ZrZn_2}$	28.5	0.29	21	0	0.4	290	0.17
$\mathbf{URhGe}$	9.5	0.25	$-$	$0.3-0.4$	0.71	180	0.42

Table 2.2 Comparison of 3 superconducting ferromagnets. The UGe_2 and $ZrZn_2$ data is for the single crystal and the $URhGe$ data is on a polycrystal. Note that $\mathbf{M}$ is the magnetic moment in Bohr magnetons per formula unit.

Chapter 3

Mean field theory for a superconducting ferromagnet

In this chapter I present the full analysis of our ideas of a superconducting ferromagnet. I start with a review of the preliminary work that was a motivation for the development of the model studied here, and then go into the full details of the calculations, including analytical results, numerical results, and emphasizing comparison to experiments and predictions for future experiments. I also add a section on a p-wave calculation that can be directly compared with the s-wave predictions and some experiments on SC/FM materials. Concluding the chapter will be a discussion of the criticisms and comments concerning this theory which is appropriate due to the controversial response some of this work has received, and many comments concerning approximations and suppositions will be postponed until this section.

3.1 Background - local Fermi liquids

The mean field model studied in this chapter, particularly its s-wave nature, only became relevant because of previous calculations of a local Fermi liquid [50]. To give a brief introduction, a local Fermi liquid (LFL) is a Fermi liquid which assumes a momentum-independent electron self-energy: $\partial\Sigma/\partial\mathbf{p} = 0$. A local self-energy implies a local irreducible 4-point vertex function, $\Gamma^{IR}_{\omega,\omega'}(q)$, and a local irreducible vertex function then implies a local *full* vertex function, $\Gamma_{\omega,\omega'}(q)$ [50]. The full vertex function is very important in Landau Fermi liquid theory because from it one can derive the very important scattering amplitudes $a(\mathbf{p},\mathbf{p}')$ and the Fermi liquid interaction parameters $f(\mathbf{p},\mathbf{p}')$. These two quantities describe the interactions between two particles within

an interacting many-body medium. These derivations of f and a depend on the order in which the limits on the momentum $\mathbf{q}$ and frequency ω are taken, and these are given by

$$\begin{aligned} a(\mathbf{p},\mathbf{p}') &= \lim_{|\mathbf{q}|\to 0}\lim_{\omega\to 0} z^2\Gamma_{p,p'}(q) \\ f(\mathbf{p},\mathbf{p}') &= \lim_{\omega\to 0}\lim_{|\mathbf{q}|\to 0} z^2\Gamma_{p,p'}(q), \end{aligned} \tag{3.1}$$

with z being the quasiparticle residue. In general, f and a are related to each other after making use of a spherical harmonic expansion by

$$A_l^{s,a} = \frac{F_l^{s,a}}{1+F_l^{s,a}/(2l+1)}, \tag{3.2}$$

where $A_l^{s,a}$ and $F_l^{s,a}$ are defined throught the relations

$$A^{\sigma\sigma'}(\mathbf{p},\mathbf{p}') = N(0)a^{\sigma\sigma'}(\mathbf{p},\mathbf{p}') = \sum_l \left(A_l^s + \vec{\sigma}\cdot\vec{\sigma}' A_l^a\right) P_l(\hat{p}\cdot\hat{p}') \tag{3.3}$$

$$F^{\sigma\sigma'}(\mathbf{p},\mathbf{p}') = N(0)f^{\sigma\sigma'}(\mathbf{p},\mathbf{p}') = \sum_l \left(F_l^s + \vec{\sigma}\cdot\vec{\sigma}' F_l^a\right) P_l(\hat{p}\cdot\hat{p}'). \tag{3.4}$$

The most important consequence of the local full vertex function is that the scattering amplitudes and Landau functions become independent of momentum angles and are s-wave, so that $A_l^{s,a} = F_l^{s,a} = 0$ for $l \geqslant 1$. This results in a simplified forward scattering sum rule, which is basically an equation that imposes the constraint that no two identical particles can scatter into the same state (see [51] page 84). This is just the Pauli principle, and is written as:

$$\sum_l A_l^{\uparrow\uparrow} = \sum_l (A_l^s + A_l^a) = 0. \tag{3.5}$$

However, in the context of a LFL, this relation simplifies to just $A_0^s + A_0^a = 0$, which greatly reduces the number of terms from infinity to just two. Plugging this into (3.2) gives

$$F_0^{s,a} = \frac{-F_0^{a,s}}{1+2F_0^{a,s}}, \tag{3.6}$$

which is a useful relation between the symmetric and antisymmetric F's.

The scattering amplitudes and Landau functions are important because they give information about physical quantities of the Fermi liquid. For example, the F's are related to the effective mass, the susceptibility, and the compressibility. The scattering amplitude A is akin to a coherence length, in that when it displays a divergence, it indicates some instability in the system, such as a phase transition. It also can give information on the superconducting pairing strength in a given momentum channel.

It is evident how the constraint of a LFL directly affects the physics of certain systems. The main interest in this chapter is the weak ferromagnet LFL and discussion of the paramagnetic LFL can be found in [50].

A weak ferromagnet can be characterized by a small equilibrium magnetization m_0. In this limit, the magnetization depends on the Landau parameter F_0^a, calculated by expanding the free energy in terms of m_0 to fourth order and then minimizing it [5]. This dependence is expressed as

$$m_0 \sim |1 + F_0^a|^{1/2}, \tag{3.7}$$

and the requirement for the minimum of energy is when $F_0^a < -1$. One sees then that the magnetization goes to zero as $F_0^a \to -1^-$. Therefore, at $F_0^a = -1$ a ferromagnetic instability is encountered which is seen from (3.2) where $A_0^a \to \infty$. As a consequence of $F_0^a \to -1$, from (3.6) $F_0^s \to -1^+$ and a charge instability also occurs since $A_0^s \to -\infty$.

The importance of these results becomes clear when one calculates the pairing amplitudes for superconductivity *inside* this local ferromagnetic state. The two pairing channels of interest are the singlet and triplet channels, whose potentials are given by [51]

$$A^{sing} = A_0^s - 3A_0^a = -4A_0^a = -4\frac{F_0^a}{1 + F_0^a} \tag{3.8}$$

and

$$A^{trip} = A_0^s + A_0^a = 0. \tag{3.9}$$

Notice that the triplet amplitude is just the Pauli principle again for the local case and is strictly zero. However, the singlet amplitude, for $F_0^a < -1$, is negative and thus attractive! In other words,

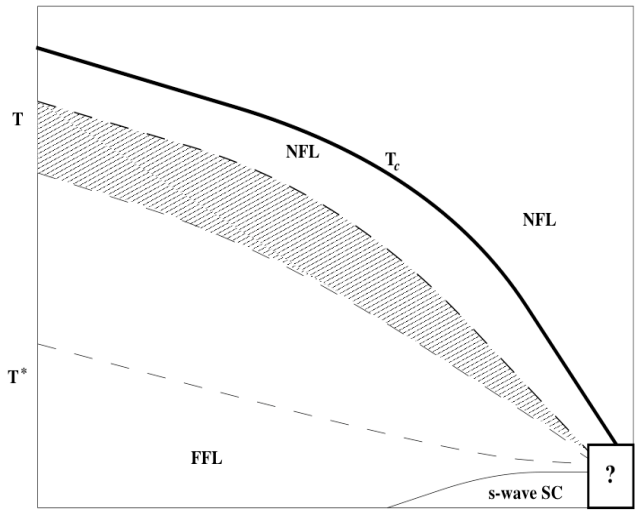

Figure 3.1 Phase diagram prediction taken from Blagoev *et al*. [5], describing a weak ferromagnetic metal in the LFL picture. The box around the phase transition shows the uncertainty in the crossover regime at small T. The T^* line indicates a temperature below which exists a (ferromagnetic) Fermi liquid. This was published before UGe_2 was found to have a strikingly similar phase diagram.

in a weak local ferromagnet, the only channel available for pairing is the s-wave singlet channel. If superconductivity could exist, it should be of this conventional type. Naively, one would expect triplet pairing in a ferromagnet, but in this local sense the same spin electrons must be far apart and only opposite spins can pair. This prediction is nicely represented in Figure 3.1.

One may question if a weak ferromagnetic metal can be characterized as local, but it can be shown that near the critical point, the vertex corrections are small and the self energy is very weakly momentum dependent [7]. In fact, the effective coupling increases in this area which enhances the s-wave pairing. On the paramagnetic side, ferromagnetic fluctuations suppress s-wave pairing [22], but on the ferromagnetic side, they actually enhance it.

In summary, a local Fermi liquid theory has been introduced that predicts ferromagnetism coexistent with s-wave superconductivity. This is the motivation that leads to the development of a model Hamiltonian for the study of coexistent superconductivity and ferromagnetism.

3.2 Model

The model is explained briefly here, and the reader is referred to the original publication [37] for full details. The model Hamiltonian is written as two interaction terms; one is the spin-spin magnetic operator and the other is the BCS-like pairing term. The magnetic coupling is described by a constant J which mediates the ferromagnetic strength. This term is the consequence of the spin rotation symmetry being spontaneously broken explicitly. The BCS interaction strength is measured by the coupling g. To arrive at the effective mean field Hamiltonian, one needs to perform a mean field transformation. An example of this is a transformation of the BCS term:

$$-g \sum_{p} c^{\dagger}_{p\uparrow} c^{\dagger}_{-p\downarrow} c_{-p\downarrow} c_{p\uparrow}. \tag{3.10}$$

This is a four-fermion interaction which is difficult to work with, and it would be convenient to make it quadratic in the fermion operators. To do this, one can take two of these operators and define

$$c^{\dagger}_{p\uparrow} c^{\dagger}_{-p\downarrow} = < c^{\dagger}_{p\uparrow} c^{\dagger}_{-p\downarrow} > + \left(c^{\dagger}_{p\uparrow} c^{\dagger}_{-p\downarrow} - < c^{\dagger}_{p\uparrow} c^{\dagger}_{-p\downarrow} > \right), \tag{3.11}$$

which is obviously true, and can be interpreted as the operator $c^{\dagger}_{p\uparrow} c^{\dagger}_{-p\downarrow}$ equal to its average $< ... >$ plus the fluctuations about its average, denoted by the term in parentheses. The same equation can be written out for the 2 non-dagger terms in (3.10). Upon multiplication of $c^{\dagger} c^{\dagger} cc$, terms that are quadratic in the fluctuations can be dropped because they can be shown to be small, especially in systems with many particles, as in a superconductor. Collecting the remaining terms, (3.10) becomes

$$\sum_{p} \left(\Delta c^{\dagger}_{p\uparrow} c^{\dagger}_{-p\downarrow} + \Delta c_{-p\downarrow} c_{p\uparrow} \right) + \frac{\Delta^2}{g}, \tag{3.12}$$

where the fluctuations have been thrown away and $\Delta = -g < c_{-p\downarrow} c_{p\uparrow} >$. This is the superconducting order parameter, or energy gap. This mean field transormation is used very often in many-body problems. A 'real' superconducting gap is assumed that is not momentum-dependent. The full effective Hamiltonian is then

$$
\begin{aligned}
H &= \sum_{\vec{p}} \epsilon_p (c^{\dagger}_{\vec{p}\uparrow} c_{\vec{p}\uparrow} + c^{\dagger}_{\vec{p}\downarrow} c_{\vec{p}\downarrow}) + \frac{JM}{2} \sum_{\vec{p}} (c^{\dagger}_{\vec{p}\uparrow} c_{\vec{p}\uparrow} - c^{\dagger}_{\vec{p}\downarrow} c_{\vec{p}\downarrow}) \\
&- \sum_{\vec{p}} (\Delta c^{\dagger}_{\vec{p}\uparrow} c_{-\vec{p}\downarrow}^{\dagger} + H.c.) + \frac{1}{2} JM^2 + \frac{|\Delta|^2}{g}. \qquad (3.13)
\end{aligned}
$$

The diagonalization of this Hamiltonian is carried out with the use of a particular Bogliubov transformation given in matrix form as

$$
\begin{pmatrix} \alpha_p \\ \beta_p \end{pmatrix} = \begin{pmatrix} u_p & v_p \\ -v_p^* & u_p \end{pmatrix} \begin{pmatrix} c_{p\uparrow} \\ c^{\dagger}_{-p\downarrow} \end{pmatrix}, \qquad (3.14)
$$

with the inverse transformation given by

$$
\begin{pmatrix} c_{p\uparrow} \\ c^{\dagger}_{-p\downarrow} \end{pmatrix} = \begin{pmatrix} u_p & -v_p \\ v_p^* & u_p \end{pmatrix} \begin{pmatrix} \alpha_p \\ \beta_p \end{pmatrix}. \qquad (3.15)
$$

The complex conjugate of the fermion operators can be taken to find the necessary remaining relations, but only real quantities without a phase argument will be considered, so $v_p^* = v_p$. The coherence factors u_p, v_p are constrained by $u_p^2 + v_p^2 = 1$ and are equal to

$$
u_p = \sqrt{\frac{1}{2}\left(1 + \frac{\xi_p}{E_p}\right)}; \quad v_p = \sqrt{\frac{1}{2}\left(1 - \frac{\xi_p}{E_p}\right)}. \qquad (3.16)
$$

Note that $E_p = \sqrt{\xi^2 + \Delta^2}$ which is the usual BCS dispersion. Making use of these formulae and diagonalizing (3.13) gives the mean field Hamiltonian

$$
H_{MF} = E_0 + \sum_{\vec{p}} \left(E_p^{\alpha} \alpha^{\dagger}_{\vec{p}} \alpha_{\vec{p}} + E_p^{\beta} \beta^{\dagger}_{\vec{p}} \beta_{\vec{p}} \right), \qquad (3.17)
$$

where

$$
\begin{aligned}
E_0 &= \sum_{\vec{p}} \epsilon^{\downarrow}_{\vec{p}} + \frac{1}{2} JM^2 + \frac{|\Delta|^2}{g}, \\
\epsilon^{\downarrow\uparrow}_{\vec{p}} &= \frac{p^2}{2m^*} - \mu \mp \frac{JM}{2}.
\end{aligned}
$$

The quasiparticle energy dispersion relations for the alpha and beta fermion are

$$\begin{aligned} E_p^\alpha &= \frac{JM}{2} + \sqrt{\xi_p^2 + |\Delta|^2}, \\ E_p^\beta &= \frac{JM}{2} - \sqrt{\xi_p^2 + |\Delta|^2}. \end{aligned} \tag{3.18}$$

These are the expressions for the excitations of the system. There is one very important difference between the excitations here and the excitations in a conventional superconductor with energy $E_p = \sqrt{\xi_p^2 + |\Delta|^2}$. In the latter case the quasiparticles are completely gapped at the Fermi level by an energy of 2Δ. However, in the former case there exists *gapless* excitations due to the magnetization. This is not due to nodes in the pairing symmetry or from impurities. The alpha fermion is fully gapped, but the beta fermion has energies within the gap since at $T = 0$ the energy $E_p^\beta < 0$ (3.18). This effectively means that there is a subset of the particles that behave as they would in a normal metal, and this alters the physical properties in a corresponding fashion.

The final step of this initial process is to minimize the effective free energy F of the system to produce the mean field equations. There are two order parameters, the magnetization M and the superconducting gap Δ. The appropriate minimization then requires that $\delta F/\delta M = 0$ and $\delta F/\delta \Delta = 0$. Carrying this out, one finds that

$$M = \frac{1}{2} \int \frac{d^3p}{(2\pi)^3} (1 - n_p^\alpha - n_p^\beta), \tag{3.19}$$

and

$$|\Delta| = \frac{|\Delta| g}{2} \int \frac{d^3p}{(2\pi)^3} \frac{n_p^\beta - n_p^\alpha}{\sqrt{\xi_p^2 + |\Delta|^2}}, \tag{3.20}$$

where

$$n_p^{\alpha,\beta} = \frac{1}{e^{\beta E_p^{\alpha,\beta}} + 1}. \tag{3.21}$$

These are three very important equations, and as can be seen from (3.18), each one is coupled in M and Δ and will have to be solved self-consistently. These order parameters will be calculated below for two different cases; zero temperature and finite temperature.

3.3 $\mathbf{T = 0}$

The three equations above can be simplified somewhat at $T = 0$. It is seen from the dispersion relations (3.18) that E_p^α is always positive for any value of the momentum because the magnetization M is positive, as is J. Thus there are no α-quasiparticle excitations at zero temperature. On the other hand, the energy of the beta fermion is negative in the range of momenta $p < p_F^+$ and $p > p_F^-$, where

$$p_F^\pm = \sqrt{2m^*\mu \pm m^*\sqrt{(JM)^2 - 4|\Delta|^2}}. \tag{3.22}$$

JM must be greater than 2Δ which is an inequality that is assumed for the rest of the calculations. For the values of momenta where $E_p^\beta < 0$, it is clear from (3.21) that $n_p^\beta = 1$. One then sees that (3.19) is only nonzero for $n_p^\beta = 0$, where $p_F^- < p < p_F^+$, and after carrying out the simple integration the magnetization becomes

$$M = \frac{1}{12\pi^2}\left[(p_F^+)^3 - (p_F^-)^3\right]. \tag{3.23}$$

3.3.1 Order parameters

Examining (3.23) with the superconducting gap $\Delta = 0$, the solution can be found by a simple, iterative algorithm. The solution gives a ferromagnetic $T = 0$ curve as a function of J, and the plot is shown in Figure 3.2.

The magnetization is defined such that it is zero at $J = 1$. This is a rescaled J that is in fact the Stoner factor $JN(0)/2$, which signals the onset of magnetic order when it takes a value greater than 1. The J appearing in all of the calculations is scaled to be this Stoner factor. An approximate analytic expression can also be derived after expanding (3.23) to order $(JM/\mu)^3$ to find

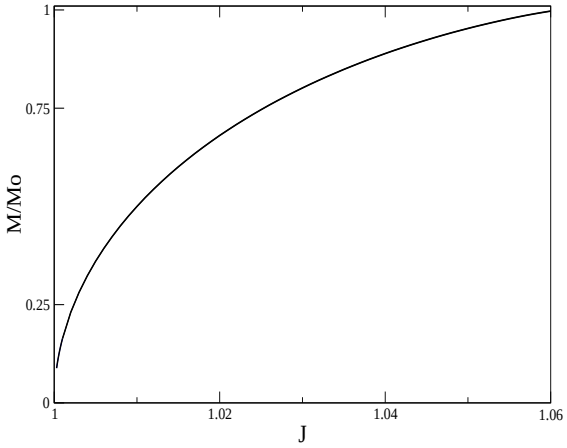

Figure 3.2 The magnetization curve at zero temperature and $\Delta = 0$, rescaled by $M_0 = 238$, the value of the magnetization at $J = 1.06$. All of the quantities in the plots are scaled to be unitless. The quantities in the text, however, are not scaled. J will generally take values for which $J \gtrsim 1$, which puts the magnetization in the weak ferromagnetic regime.

$$M = \frac{2\mu}{J}\sqrt{24\left(1 - \frac{2}{JN(0)}\right)}. \tag{3.24}$$

The gap equation, (3.20), is first examined by setting the magnetization to zero. For consistency, this should reduce to the BCS equation for the superconducting gap. In this limit, with the integration explicitly shown, (3.20) becomes

$$\frac{1}{g} = \frac{1}{(2\pi)^2}\left(\int_{p_F-\lambda}^{p_F+\lambda}\frac{d^3p}{(2\pi)^3}\frac{1}{\sqrt{\xi_p^2+\Delta^2}} - \int_{p_F^-}^{p_F^+}\frac{d^3p}{(2\pi)^3}\frac{1}{\sqrt{\xi_p^2+\Delta^2}}\right), \tag{3.25}$$

where λ is the Debye cutoff in momentum space, corresponding to the energy ϵ_D[1]. Solving this equation numerically for the gap Δ as a function of the coupling g results in the curve in Figure 3.3.

An analytical expression can also be found for (3.25) which gives the well-known BCS result,

[1]The cutoff is handled numerically in these integrals by assuming a value which is a fraction of the Fermi energy as is usually done in the BCS case. This fraction is about 10%.

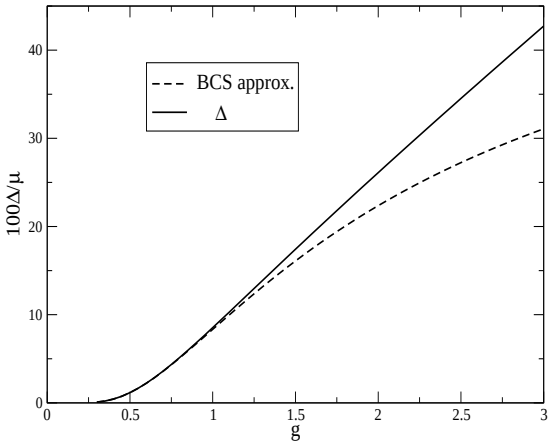

Figure 3.3 Superconducting curve ($M = 0$) at zero temperature from the numerical solution of (3.25), labeled as Δ, along with the weak coupling curve of equation (3.26) given as the dashed line.

$$\Delta = \frac{\epsilon_D}{\sinh\left(1/N(0)g\right)}, \tag{3.26}$$

which, in the weak coupling limit for small $N(0)g$, is $\Delta_0 \approx 2\epsilon_D \exp^{-1/N(0)g}$. The solution to (3.25) as well as the weak coupling curve (3.26) are plotted in Figure 3.3. The two curves converge for small g, but differ by several percent at larger g.

With the single phase solutions found, I now study the non-trivial solutions of the coexistent state. Equations (3.23 and 3.25) are solved *self-consistently*. As a first approximation, it is possible analytically to decouple these equations in the limit where $JM \gtrsim 2\Delta$ and the two order parameters are proportional to each other. In other words, one can derive

$$\begin{aligned} M &= \frac{2}{J}\frac{r}{r+1}\Delta_0 \\ \Delta &= \sqrt{\frac{r-1}{r+1}}\Delta_0, \end{aligned} \tag{3.27}$$

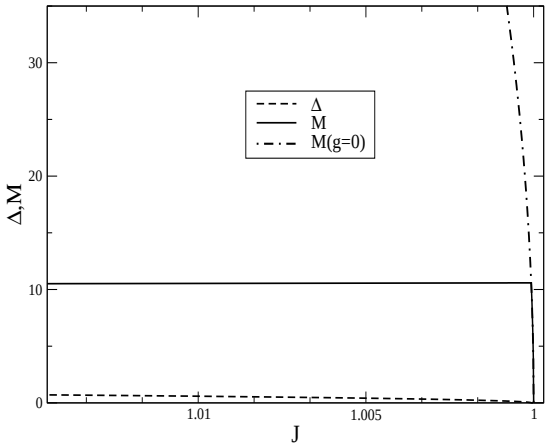

Figure 3.4 Coexistent magnetic and superconducting solution at zero temperature, with $g = 1$. The saturation magnetization plot is calculated with $g = \Delta = 0$ (dash-dot line). Note that the x-axis is inverted.

where $r = JN(0)/2$ and Δ_0 is defined above. This approximation works well for a broad range of the $g - J$ coupling constant space, however, it misses some of the important physics as evidenced shortly. Fortunately, this approximation is not necessary, since the numerical solutions to the full equations are reasonably easy to calculate [52].

There are 2 sets of solutions to the coupled equations, one as a function of J, and one as a function of g. In Figure 3.4 the order parameters are shown plotted as a function of J with a fixed $g = 1$. Also shown on the plot is the full magnetization curve ($\Delta = 0$) from Figure 3.2 as a reference. Note the dramatic decrease in the magnetization that results from introducing the superconducting pairing. For very small J where the superconducting gap is very close to zero, the magnetization is basically indistinguishable from the 'parent' curve, as one would expect, and the slope here is quite steep. The order parameters vary very little with respect to J and the approximate equations (3.27) model these curves quite well when plotted in this parameter range. The effect of varying g only shifts the curves up or down the y-axis and does not alter the qualitative behavior.

In Figure 3.5 the coexistent solutions are plotted as a function of g with a small $J = 1.001$. Since the main interest is weak ferromagnetism, small values of J will be used. At $g = 0$, no solutions are found numerically due to the self-consistency condition. As g is increased, the order parameters grow smoothly, but at a certain $g = g_{max}$, the gap begins to decrease for larger g and eventually gets suppressed to zero[2]. Once this happens, the magnetization levels off because M is not an explicit function of g, only an implicit one through Δ. Thus, if $\Delta = 0$, M is constant vs. g for any finite J. As mentioned earlier, the approximate equations (3.27) do not capture this very important feature of the gap being suppressed to zero, and so the approximate gap from (3.27) is plotted as a reference. The numeric solution and the analytic Δ agree for small g, but then they split off and the analytic solution behaves an an exponential function of g. For large g, the Δ of (3.27) approaches a constant. Furthermore, (3.27) is only valid for small g. Although not shown in Figure 3.5, the magnetization from (3.27) continues to increase as g is increased, since M is a function

[2]I have not rescaled the order parameters M and Δ here since it would be inconvenient in that each one would have a different normalization factor. It should be noted however that the numbers on each axis are unitless. The magnetization and the gap are made unitless by factors of the chemical potential and/or Fermi momentum. Similar to what was mentioned for J, the parameter g is also scaled by a density of states factor.

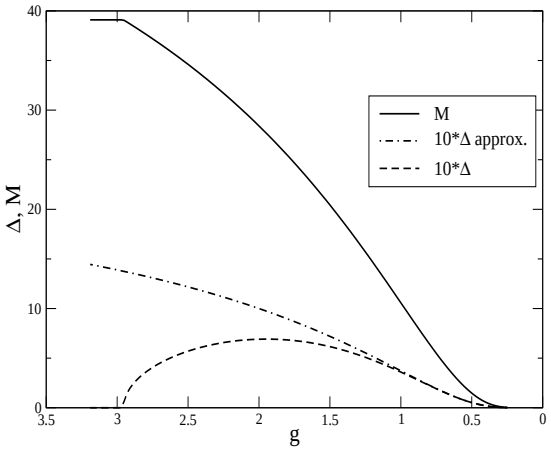

Figure 3.5 Coexistent magnetic and superconducting solution at zero temperature for $J = 1.001$. The gap parameters are multiplied by a factor of 10 for distinguishability. The approximate curve (dash-dot line) is taken from equation (3.27).

of g through Δ_0, whereas M in the numerical result remains constant after the superconductivity disappears.

3.3.2 Energy

In constructing the Hamiltonian of this system, the procedure was to break the spin rotation symmetry and then introduce the superconducting pairing. It is important to understand that initially there is a ferromagnetic state, within which the superconductivity arises. To determine the lowest energy state, which any good theory must do, we will consider the energy difference between the ferromagnetic and the coexistent FM/SC state. There has been some confusion about this in the literature and it will be addressed at the end of the chapter. For instance, if there is first a normal state with no ferromagnetism or superconductivity, and the coupling constants are changed, the lowest energy state that arises is always the BCS superconducting state. That is known [29, 53, 54]. The question to pose in the present case however is the following: In a weak ferromagnetic metal, are there a range of parameters in which superconductivity would appear and subsequently lower the total energy? This is the question that will be answered in this section.

The energy can be calculated easily by taking the expectation value of the Hamiltonian (3.17) at zero temperature. The alpha quasiparticle energy does not contribute at zero temperature. There are several quantities that are important for this calculation, and the first one is the energy of the normal, paramagnetic state. Since it is used often, it is given here explicitly as

$$E_N = \langle H(M = \Delta = 0) \rangle_N = \frac{2}{(2\pi)^3} \int_0^{p_F} d^3p \left(\frac{p^2}{2m^*} - \mu \right), \tag{3.28}$$

with the factor of 2 in front accounting for the spin. This can be calculated to give $E_N = \frac{-8}{15\pi^2} N(0)\mu^2$. The next very important quantity is the energy of the ferromagnetic state which, as explained above, is the reference energy with which the coexistent state will be compared. The FM energy is calculated by taking the expectation value of the Hamiltonian and setting $\Delta = 0$ in the expression. After a little algebra an integral equation can be found of the form

$$E_{FM} = \langle H(\Delta = 0)\rangle = \int_0^{p_F} \frac{d^3p}{(2\pi)^3}\,(\xi_p - |\xi_p|) - \int_{p_F^-}^{p_F^+} \frac{d^3p}{(2\pi)^3}\left(\frac{JM}{2} - |\xi_p|\right) + \frac{JM^2}{2}. \quad (3.29)$$

Numerically, this energy equation is solved quite easily, but (3.29) also reduces to a nice approximate analytic expression to second order in $(JM/2\mu)$ given by

$$E_{FM} \simeq -12N(0)\mu^2(1 - \frac{1}{r})^2, \quad (3.30)$$

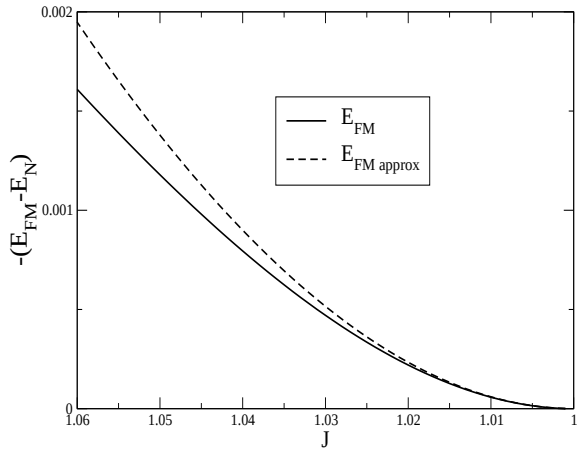

Figure 3.6 Ferromagnetic state energy. The y-axis shows the *negative* of the energy difference between the FM state and the normal state (E_N). This convention will be used throughout the text. The dashed curve corresponds to the analytic equation (3.30), and the solid one to (3.29).

where r was defined previously and the normal state energy has been subtracted off. To give an idea of the validity of the approximation, Figure 3.6 shows the energy of the ferromagnetic state $(\Delta = 0)$ for the numerical and the approximate solution. The curves agree well for small J, but as J grows larger, the approximate solution overestimates the energy difference. In all of the calculations below, I use the non-approximate equation. Additionally, from Figure 3.6, one sees that the ferromagnetic state has a lower energy that the normal state at zero temperature as expected.

The ferromagnetic energy is therefore accurately modeled, and the coexistent state is now studied. To do this, one needs to generate M, Δ pairs as functions of g or J, and then plug them into the energy equation. The energy equation in this case is (3.29) with the gap parameter reinserted.

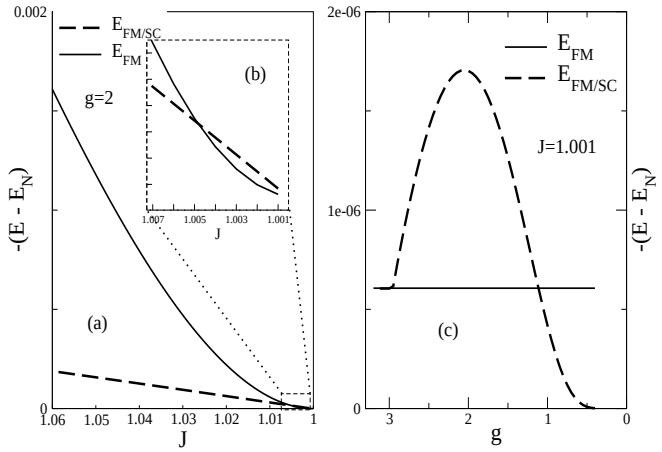

Figure 3.7 The energy difference between the coexistent (FM/SC) and ferromagnetic (FM) states. In (a), the energy difference varies with J, and the inset is the zoom of the region where the coexistent state is the lowest in energy. (c) is the energy difference as a function of g.

Figure (3.7) shows the main result of the zero temperature energy analysis. The coexistent state, in a certain parameter range, exhibits the lowest energy state, which answers the question posed before. The energy difference between $E_{FM/SC}$ and E_{FM} is plotted versus each of the coupling constants g and J. In part (a), the energy of the coexistent state is seen to be lowest only for very small values of J, the regime of weak ferromagnetism, and the inset (b) zooms in on this region. Then the value of $J = 1.001$ is taken and a sweep of g is made in panel (c). The energy difference varies widely as a function of g. The coexistent energy is lowest for $g \sim 2$, which is where the superconductivity is 'strongest', i.e., where the gap Δ has the greatest value. This can be seen referring back to Figure 3.5, where the maximal value of the gap corresponds to $g \sim 2$ in the coexistent state.

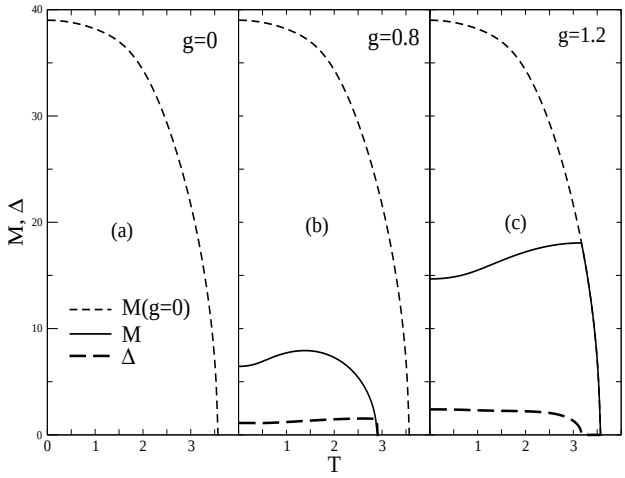

Figure 3.8 Temperature-dependence of the magnetization and the gap for $J = 1.001$. In (a) is shown the pure ferromagnetic Curie behavior, which is subsequently reproduced in all three plots for reference. (b) comprises the coexistent solutions for a small g, where the T_c of each parameter coincides. (c) shows a plot for $g > g_c$ where $T_{SC} < T_{FM}$ and M joins the Curie curve.

3.4 $\mathbf{T \neq 0}$

The unexpected behavior at $T = 0$ leads to very interesting behavior at finite temperatures. The equations which simplified nicely (3.19, 3.20) before, will be much more difficult to solve now, and one cannot rely on many analytical solutions. Thus, there are two coupled, integral equations which again are solved numerically and self-consistently as a function of temperature, while keeping everything else fixed. A phase diagram is then generated from the solutions. A schematic of the numerical method is given in Appendix A and B.

The temperature-dependence of the order parameters are given in Figure 3.8 for three characteristic plots. The first one, (a), is the ferromagnetic curve when no superconductivity is present. This gives the Curie temperature for $J = 1.001$, which here is $T_c \approx 3.5$, and, after taking out our scaling factors gives $k_B T_{FM} \approx \mu/100$. For a comparison, a typical Fermi energy in UGe_2, is in the range of $0.1 - 1ev$, which gives a Curie temperature in our model of about $10 - 100K$; on the order of what is seen in the superconducting ferromagnets (see Chapter 2). Having established a rough

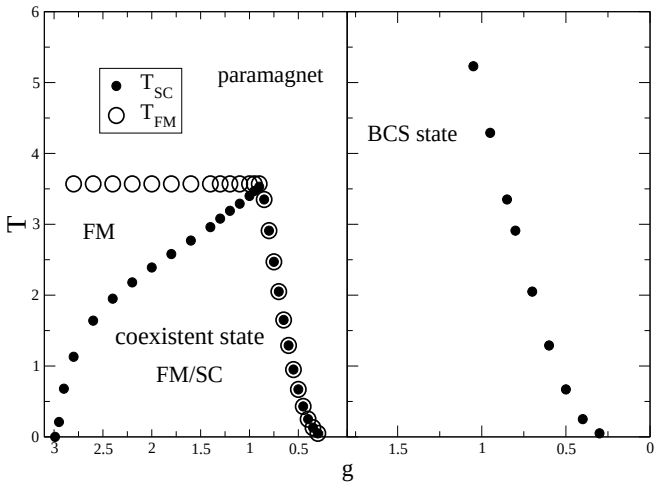

Figure 3.9 The phase diagram for this model for $J = 1.001$ in $T - g$ space. The different regions are labeled accordingly. Also shown is the BCS phase diagram in the right panel to emphasize the difference when there is magnetic order present.

qualitative accuracy, the superconducting pairing is turned on and the results are shown in (b) and (c) of Figure 3.8. For a small value of g, the superconducting and magnetic transition temperatures of the coexistent state are equal, $T_{FM} = T_{SC}$, as is shown in (b). In this range, as the gap gets suppressed to zero, so does the magnetization. This behavior occurs up until a critical $g = g_c$, at which point the coexistent T_c's and the pure ferromagnetic critical temperature are all equal. For $g > g_c$, T_{SC} is lowered again since $\Delta \to 0$ while M remains finite, and once this happens, the magnetic parameter joins the 'parent' curve because at this temperature point, g is effectively zero since there is no finite gap Δ. In words, T_{SC} goes from zero for $g = 0$ to a maximum value for $g = g_c$, and then back to zero for $g \approx 3g_c$.

Finding the transition temperatures for each value of g gives a way to map out a phase diagram, and this has been done in Figure 3.9. For $0 < g \lesssim 1$, $T_{FM} = T_{SC}$, and the points fall on the same curve. T_{SC} and T_{FM} reach their maximal value for $g = g_c \approx 1$. For $g > g_c$, the superconductivity goes to zero more quickly for larger and larger g and thus $T_{SC} \to 0$, while T_{FM} remains constant since it is not an explicit function of g. For comparison, in the right panel the pure BCS superconducting critical temperature is plotted versus g, to show how T_{SC-BCS}

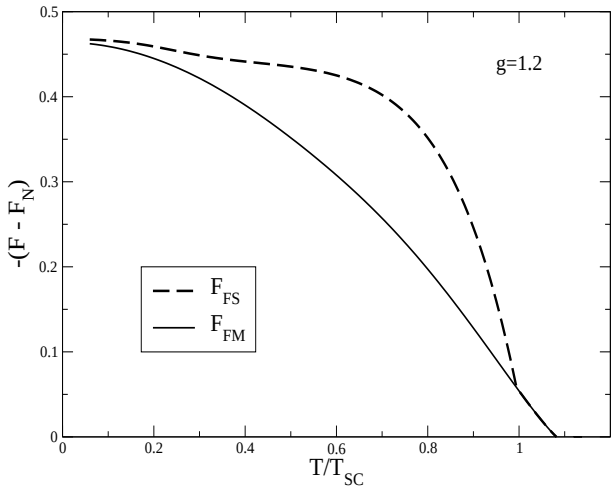

Figure 3.10 The temperature-dependent free energy difference between the coexistent and ferromagnetic state, plotted vs the scaled superconducting transition temperature for $g = 1.2$ and $J = 1.001$.

increases without limit when there is no magnetization. This phase diagram resembles what is seen experimentally in UGe_2 at high pressures in that the superconductivity has a dome-like feature. To reproduce the 'pressure' axis would require some combination of J and g, not just plotting one or the other on the axis. Doing this might enable one to reproduce even more clearly the experimental phase diagram.

The final thing to consider is the *free energy* which takes into account the entropy at nonzero temperatures. At high enough temperatures the entropy dominates, and thus the paramagnetic state is preferred. In between, however, there is competition between the magnetic state and the coexistent state. The free energy is generally given by

$$F = \langle H \rangle - TS,$$

where, in the case of the coexistent solution, the $-TS$ part is given by

$$-TS = k_b T \sum_p \left[\beta E_p^\alpha (1 - n_p^\alpha) - \ln\left(1 + e^{\beta E_p^\alpha}\right) + \beta E_p^\beta (1 - n_p^\beta) - \ln\left(1 + e^{\beta E_p^\beta}\right) \right],$$

which comes from the standard definition of the entropy applied to the two different types of quasiparticles that are present at finite temperature. The $< H >$ part is the same as before except the alpha quasiparticle is excited for finite temperature and therefore $n_p^\alpha \neq 0$. Calculating the free energy, one finds that the coexistent state is favorable throughout the temperature range, as seen in Figure 3.10. The value $g = 1.2$ is chosen because it gives the highest T_{SC} after the $g = g_c$ point in the phase diagram of Figure 3.9, i.e., at the top of the superconducting dome where $T_{SC} \neq T_{FM}$. As T_{SC} goes to zero, the coexistent free energy curve joins the magnetic free energy curve as expected, and at about $T \cong 1.1T_{SC} = T_{FM}$, the normal state is recovered. To reiterate, the coexistent state is energetically favorable to the FM state, and the Fermi liquid analysis which predicted s-wave pairing SC is confirmed in this model.

3.5 Specific heat

Since one of the main interests in this chapter is to show that an s-wave pairing scheme is a possible solution to the problem of the superconducting ferromagnets, it is important to be able to describe experimental data with the model derived above. One of the most important experiments in UGe_2 has been the measurement of the specific heat. In a normal BCS superconductor, the specific heat has a very pronounced jump as the temperature is lowered through the critical temperature. In fact, it can be calculated exactly as

$$\frac{C_{SC} - C_N}{C_N} = \frac{\Delta C}{C_N} = 1.43. \tag{3.31}$$

The jump in the specific heat as the system becomes superconducting is 143%, which is very dramatic and observable. Another important property is that the superconductor is completely gapped below T_{SC}, so that the specific heat goes exponentially to zero at zero temperature.

A system that is not fully gapped differs from this behavior in two important ways. Gapless excitations, which exist in our model, produce a normal component with some quasiparticles remaining near the Fermi surface, so the decrease is not exponential anymore, but linear at low T. Fermi liquid theory predicts $C = \gamma T$, where γ is a measure of the effective mass. Also, the gaplessness results in a decrease in the specific heat jump, since not all particles participate in

the superconductivity at its onset at T_C. The gapless fermions remain 'normal', and increase the entropy somewhat.

Experiments in UGe_2 on the specific heat [2] have shown that the jump is in fact small, about $15-20\%$, much lower that 143%. This might very well be due to gapless excitations, which our model contains intrinsically due to the presence of the magnetic ordering. There can be many other causes of gaplessness, from impurities to nodes on the Fermi surface from different types of pairing. These are important, but since one cannot easily determine the source of the gapless excitations, one cannot rule out any of these possibiltites.

The specific heat is calculated starting from the expression

$$C = T\frac{dS}{dT}. \tag{3.32}$$

The entropy is already defined above in the discussion of the free energy. A standard calculation [46] is used to find the specific heat in this model, in which a few difficulties arise and are discussed in Appendix C. The difficulties are due to the presence of the magnetic terms. The only approximation used in the calculation is that the temperature variation of the superconducting gap around T_{SC} is given by the BCS expression, which is $\Delta(T) \approx \Delta(0)(1-T/T_{SC})^{1/2}$. This is a good approximation when checked numerically in the model. The final result [52] can be conveniently expressed as

$$\Delta C = \frac{\beta}{T}\frac{d\Delta^2}{d\beta}N(0)\left[1+\frac{\beta}{16}JM\int\frac{d\varepsilon}{\varepsilon}\left[sech^2\frac{\beta}{2}\left(\frac{JM}{2}+\varepsilon\right)-sech^2\frac{\beta}{2}\left(\frac{JM}{2}-\varepsilon\right)\right]\right]. \tag{3.33}$$

The most important thing to notice in this equation is the first term on the right hand side (the prefactor multiplied by 1). This term is exactly the BCS expression for the change in the specific heat, and it factors out naturally. The rest of the terms constitute a *reduction* from this value, in that they are negative. Therefore, clearly the BCS jump present is reduced due to the presence of the magnetization in these terms.

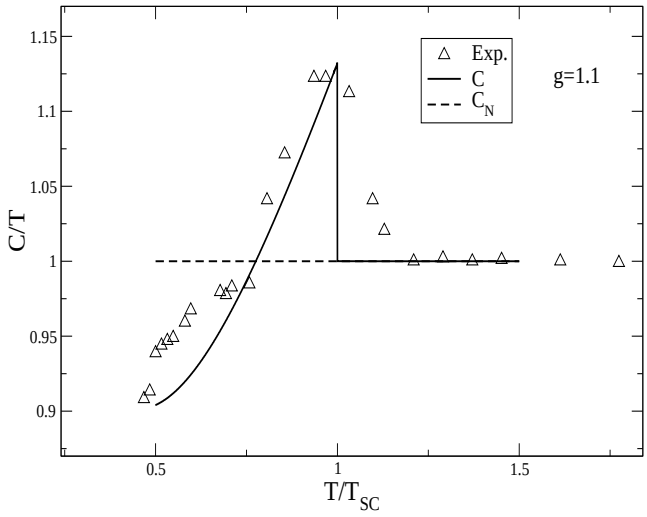

Figure 3.11 The specific heat jump from the calculation, compared to the (rescaled) data of [2] on UGe_2. One sees that the magnitude of the jumps agrees quite well. T_{FM} is at a much higher temperature. Also, note that the y-axis is C/T, which for small temperatures in both curves becomes a constant, as is the case in systems with 'normal' excitations.

It is then possible to 'tune' this decreased specific heat jump by varying the parameters of the system. The best circumstance is when there is a sizable magnetization compared to the superconducting gap, and the jump is reduced considerably from the BCS value. One example of this is given in Figure 3.11, where I plot data from a specific heat experiment on UGe_2 and the calculation. One notices that the 15% or so jump in the experiment can be easily attained from the theoretical model, and that the low temperature behavior is consistent with the Fermi-liquid like linear T-dependence. Furthermore, since several of the superconducting ferromagnets show no jump at all, the model can be tuned to accommodate this by increasing J and subsequently M, which reduces the jump even more, eventually to zero.

3.6 Transition probability effects

To understand the calculations of the next few sections, it is important to understand the role of the gapless excitations. In the specific heat, the gaplessness is responsible for the reduced BCS jump. The nuclear relaxation, electromagnetic absorption, and ultrasonic attenuation studied in this chapter are similarly affected.

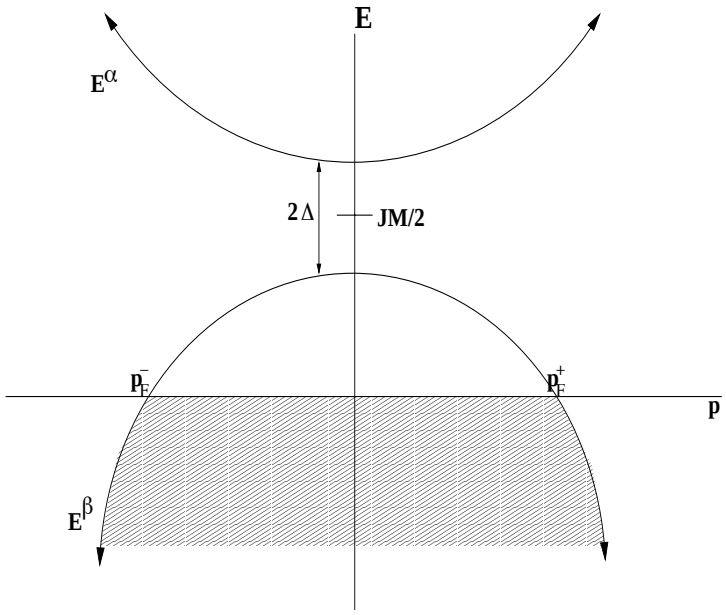

Figure 3.12 Schematic of the energy dispersion for the quasiparticles at $T = 0$. The shading corresponds to filled states. The y-axis is $E = \sqrt{\xi^2 + \Delta^2}$. The expressions for $p_F^{\pm}$ are given in (3.22). Note how the beta band only requires an infinitesimal amount of energy to cross the Fermi level.

For a clearer picture of what is happening, we look more carefully at the energy dispersion relations (3.18) for the quasiparticle excitations. A schematic of them is presented in Figure 3.12 at $T = 0$. One can think of the two different quasiparticle energies as two bands, and at zero temperature the alpha band is empty since its energy is always positive. The beta band, however, has a negative energy range, as shown in the figure, where the shading denotes filled energy levels. Overall, compared to a BCS superconductor, the curves are shifted (upward), and instead of being centered at $E = 0$, the Fermi level, they are centered at $E = JM/2$. The gap is still 2Δ since the

bottom of the alpha band is $E = JM/2 + \Delta$ and the top of the beta band is $E = JM/2 - \Delta$. However, the beta band is not constrained by the energy gap because it only takes an infinitesimal amount of energy to excite a beta particle above the Fermi energy, different from the BCS case where it takes 2Δ of energy. At any finite temperature, there will be normal excitations across the Fermi level, and it is not until a higher energy that the 2Δ is important.

Another way to see this is in the density of states, schematically shown in Figure 3.13. The Fermi level of the normal system is the zero of energy, and there is a finite density of states there. The density of states diverges at the energies indicated, which are centered around $E = JM/2$.

In examining the effects of external fields or perturbations on our system, it is necessary to consider the coherence factors again briefly (for a more thorough discussion see [55], and more generally, [46]). The coherence factors u and v (3.16), which were a result of the Bogoliubov transformation, arise in expressions of the transition probabilities as coefficients of the matrix elements in a superconductor. The possible combinations are

$$(uu' \mp vv')^2 = \frac{1}{2}\left(1 \mp \frac{\Delta^2}{EE'}\right) \tag{3.34}$$

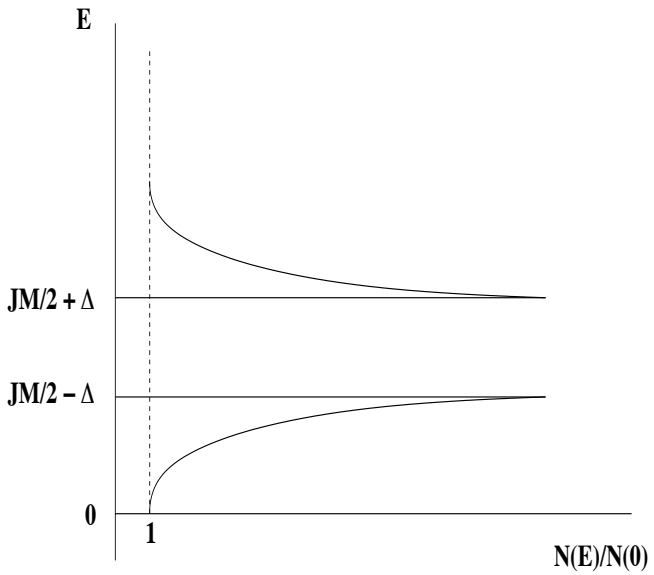

Figure 3.13 The density of states of the coexistent state, scaled with the normal state value, where E measures the energy with respect to the Fermi energy.

for quasiparticle scattering, and

$$(vu' \pm uv')^2 = \frac{1}{2}\left(1 \pm \frac{\Delta^2}{EE'}\right) \tag{3.35}$$

for the creation or annihilation of a pair of quasiparticles. This can conveniently be truncated into one function [46] given by

$$F(\Delta, E, E') = \frac{1}{2}\left(1 \mp \frac{\Delta^2}{EE'}\right). \tag{3.36}$$

The E and E' can be any function, and they will be either E^α or E^β. The upper sign corresponds to what is called case I coherence factors, and will be used for the ultrasonic attenuation calculation. The lower sign is case II, which will be used in the nuclear relaxation studies, and both cases need to be used to study the electromagnetic absorption. The calculations will involve the relaxation rate $1/T_1$, where T_1 is the characteristic relaxation time. It is also convenient to scale the rates with the normal state rate, $1/T_n$.

3.6.1 Ultrasonic attenuation

As mentioned above, the attenuation of longitudinal sound waves uses case I scattering coherence factors at low frequency external perturbations. The full expression [55]) for T_1 is given by

$$\begin{aligned}\frac{T_n}{T_1} = &\int_{-\infty}^{\frac{JM}{2}-\Delta}\left(1 - \frac{\Delta^2}{\left(\frac{JM}{2} - E\right)^2}\right)\left(\frac{N^\beta(E)}{N(0)}\right)^2\left(\frac{-\partial f(E)}{\partial E}\right)dE \\ &+ \int_{\frac{JM}{2}+\Delta}^{\infty}\left(1 - \frac{\Delta^2}{\left(E - \frac{JM}{2}\right)^2}\right)\left(\frac{N^\alpha(E)}{N(0)}\right)^2\left(\frac{-\partial f(E)}{\partial E}\right)dE,\end{aligned} \tag{3.37}$$

where $f(E)$ is the Fermi function and $N^{\beta,\alpha}$ corresponds to the density of states expression for the appropriate band, as seen in Figures 3.12 and 3.13. This ratio is plotted as a function of temperature in Figure 3.14. The critical temperature shown is that of the superconducting transition. The dashed line, which is the ultrasonic attenuation curve for the BCS superconductor, is practically off the scale and goes to zero at zero temperature. All excitations get 'frozen out' since the gap opens up

around the Fermi level as the system becomes superconducting. However, in the coexistent state, there are normal fermionic excitations, even at zero temperature, and the rate behaves accordingly, restoring to just below the normal value ($T_n/T_1 = 1$) at $T = 0$. As the temperature is increased from zero, the rate drops slightly as the presence of the gap becomes more important at higher excitation energies. But then at a temperature around $T = 0.8T_c$, the alpha band begins to be populated by transitions from below, and the rate increases again until it reaches the transition temperature into the normal state. Again, the gapless excitations have profound effects on the low T properties of the coexistent state.

3.6.2 Nuclear relaxation rate

One of the signatures of an s-wave superconductor is a rapid rise in the nuclear relaxation rate above the normal value as the system is cooled through T_c, called the Hebel-Slichter peak. The curve then decreases to zero in a conventional superconductor. This peak, however, does not exist in a p-wave superconductor, and hence it is a good signature of the pairing symmetry. Experimentally, there is still much debate about the existence of a Hebel-Slichter peak in UGe_2, since the data

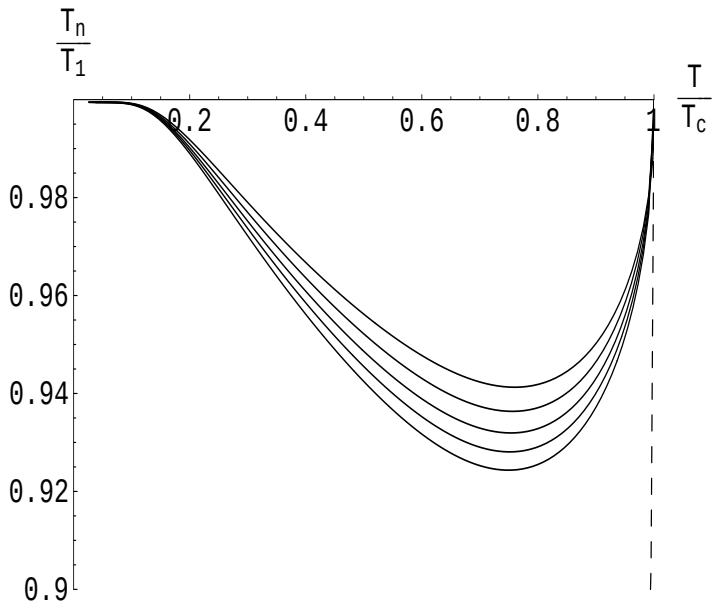

Figure 3.14 Ultrasonic attenuation for case I coherence factor absorption (low frequency). T_c is the superconducting critical temperature (T_{SC}).

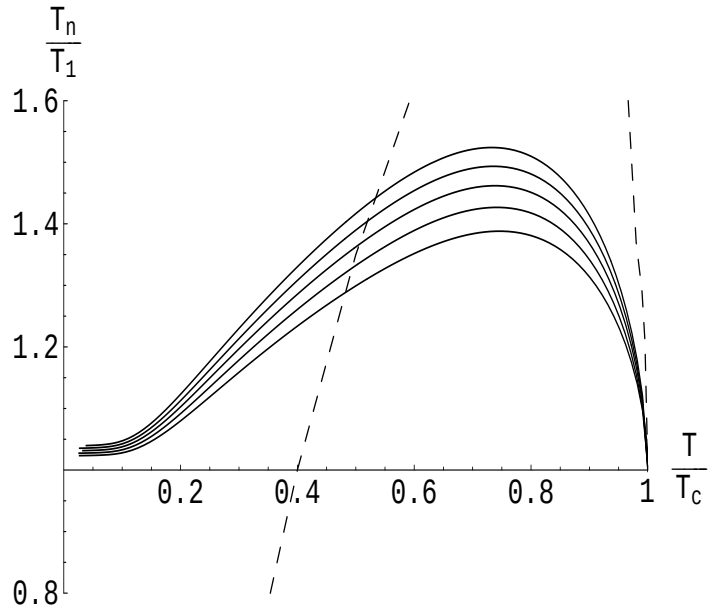

Figure 3.15 The nuclear relaxation rate ratio. The increasing value of the Hebel-Slichter peaks corresponds to increasing values of the magnitude of the superconducting gap, from varying the values of J and g.

is very difficult to take and the interpretations are subtle. It does seem as though there is a small one, or better put, it seems as though one cannot make the statement that a peak categorically *does not* exist. The calculations in this section show that the presence of the magnetization reduces the value of the Hebel-Slichter peak, and in extreme cases, can suppress it completely, even within the singlet pairing scheme. This is similar to the results of the specific heat.

The nuclear relaxation takes the case II coherence factors in the low energy scattering processes. A plot of the rate with respect to the normal state is shown in Figure 3.15. The different curves have different values of the energy gap Δ; the increasing peak height corresponding to increasing gap. The dashed line is the BCS value, which has a much higher peak, but also goes to zero at zero temperature when all of the excitations are frozen out. Since there is a finite magnetization for all of the curves, the peak value is reduced from what the non-magnetic case shows. At zero temperature, the coexistent state is not much different that the normal state, with a ratio slightly greater than one due to coherence factor effects [55].

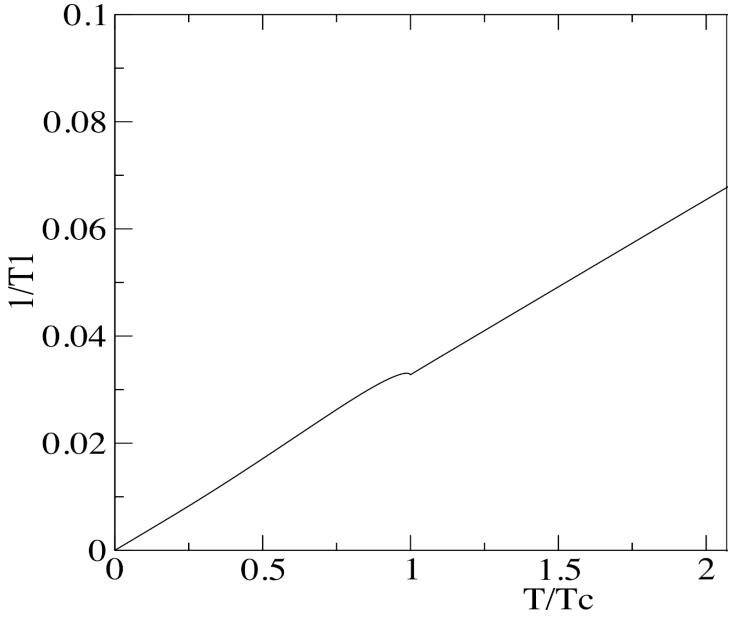

Figure 3.16 Plot of $1/T_1$ for the values of $J = 1.001$ and $g = 1.1$. The peak is difficult to see when not scaled with the normal state, but there is a 7% enhancement here as the system becomes superconducting.

To connect with the experiments, Figure 3.16 shows a plot of $1/T_1$ without the normalizing factor. For the values of J and g used, the peak is about 7% above the normal state value, which is very small indeed. Comparison to experiments will be carried out in section 3.7.3 after the p-wave model is studied.

3.6.3 Electromagnetic absorption

The absorption of electromagnetic radiation by the coexistent system requires large frequencies that can create pairs of quasiparticles, not the low frequency probes of the previous two studies. We examine what happens at $T = 0$ where there are no thermally excited quasiparticles, so that the excitations will solely be due to external energy absorption. In a normal superconductor at $T = 0$, there are no excitations until a pair of quasiparticles is created when an incident energy of $\hbar\omega = 2\Delta$ is provided, which is the minimum energy to overcome the gap. Zero energy excitations exist in this model so the results will differ. The conductivity is the appropriate quantity to study and it is written as

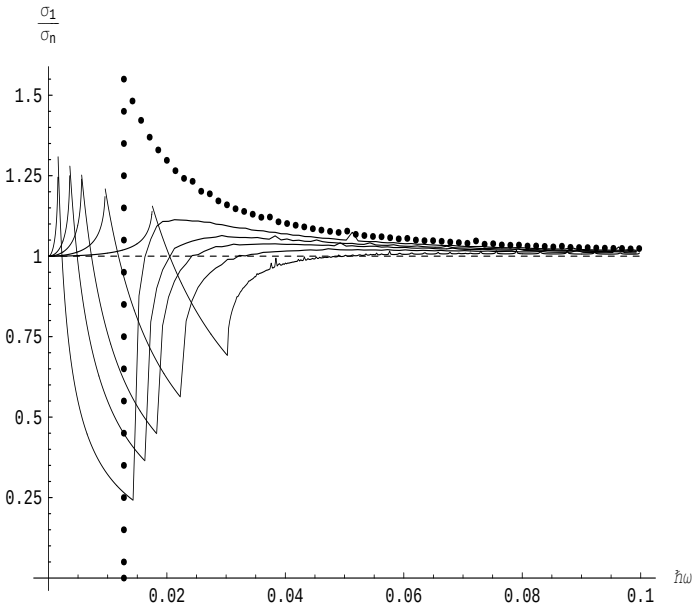

Figure 3.17 Conductivity for the case I coherence factors at $T = 0$. The solid line curves, in order of decreasing peak magnitude, have the values for the ratio of $JM/2\Delta$ given by 1.25, 1.6, 1.9, 2.5, 3.8. The dotted line, where the gap is quite visible, is for $JM/2\Delta = 1$. The horizontal dashed line is the normal state conductivity.

$$\frac{\sigma_1}{\sigma_n} = \frac{1}{\hbar\omega}\int\left(1 \mp \frac{\Delta^2}{(\frac{JM}{2} - E)(\frac{JM}{2} - E')}\right) \times \frac{N^i(E)}{N(0)}\frac{N^j(E')}{N(0)}dE, \tag{3.38}$$

where i, j corresponds to the energy bands in which one is interested. For example, for energies $\hbar\omega \leqslant JM/2 + \Delta$, only the beta band is important. The case I coherence factors for the absorption are plotted in Figure 3.17 for a full range of energies.

The various curves in Figure 3.17 are for different values of the ratio $JM/2\Delta$. The shifting of the conductivity maxima towards the y-axis ($\hbar\omega = 0$) corresponds to the *decrease* in this ratio. Changing this ratio effectively alters the range of the energy dispersions, in that it shifts them up or down, as depicted in Figure 3.12. For instance, if $JM = 0$, we have the usual BCS dispersions centered about the Fermi level. The steep drop in the conductivity immediately after the initial peak upon increasing the energy is due to the effect of the gap. This effect occurs at successively lower and lower frequencies upon reducing the value of $JM/2\Delta$, since there are fewer and fewer available scattering states as the gap approaches the Fermi level, so to speak. The dotted line in the

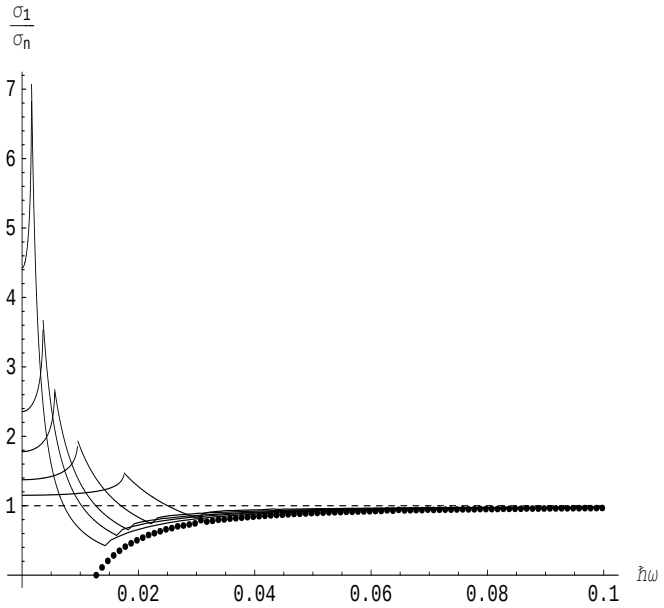

Figure 3.18 Case II conductivity. In order of increasing peak, the solid lines correspond to the value of the ratio $JM/2\Delta = 3.8$, 2.5, 1.9, 1.6, and 1.25. The dotted line is $JM = 2\Delta$, and is the BCS-*like* limit.

figure is for $JM/2\Delta = 1$, where the bottom of the energy gap is now exactly at the Fermi level, or, equally, the top of the beta band is at the Fermi energy (again, see Fig. 3.12). This corresponds to a BCS-like case. At zero temperature there is no coexistent state where Δ is larger than the magnetic energy, and therefore this is the lower limit.

The case II coherence factors calculation used for electromagnetic absorption is given in Figure 3.18. The overall behavior is similar to the previous case, and the increase in the peaks is related to a decrease in the ratio of the magnetic energy to the superconducting energy. The dotted line is what results for $JM = 2\Delta$, and it is similar to the BCS, non-magnetic, case. The gap is quite evident for this value of the ratio and the conductivity becomes finite only when $\hbar\omega = JM/2 + \Delta = 2\Delta$.

These five last figures are the predictions for the ultrasonic attenuation, nuclear relaxation, and electromagnetic absorption studies in the s-wave superconducting ferromagnetic model.

3.7 P-wave model

This section will follow somewhat closely the last section in that I present a calculation of the nuclear relaxation rate, but in a model with triplet pairing in the superconducting channel coexistent with ferromagnetism. There are differences of course with the s-wave model, but the main one is that the gapless excitations, which had such an important role in that model, do not occur in the p-wave case. Exploring a different model is important because there is data in UGe_2 for T_1, and a comparison among the s-wave, p-wave, and experimental data gives clues as to the nature of the pairing. It will be seen that through this analysis one is unable to rule out s-wave or p-wave, thus leaving the question open.

We begin from a triplet mean field model of coexistent superconductivity and magnetism from the work of Nevidomskyy [56]. The details of the derivation can be found in that paper, our paper [57], and in the thesis of Hari Dahal. The model is actually quite similar to that of Karchev [37], and I will start the analysis from the mean field equations.

3.7.1 Mean field equations

The model Hamiltionian for a p-wave superconducting ferromagnetic is similar to the Hamiltionian of the s-wave superconducting ferromagnet and will not be given here. The mean-field equations for the order parameters are derived from a saddle-point approximation. There are three order parameters in this model, two for the superconductivity $\Delta_{\pm}$ and one for the ferromagnetism M. Since the pairing is in the triplet state, there are three combinations possible. Only equal spin pairing states (ESP) up-up and down-down will be considered. All three order parameter equations are given as

$$\begin{aligned}
\Delta_-(\mathbf{k}) &= \frac{-1}{V}\sum_{\mathbf{k}'} V(\mathbf{k},\mathbf{k}')\frac{1-2f(E_-(\mathbf{k}'))}{2E-(\mathbf{k}')}\Delta_-(\mathbf{k}') \\
\Delta_+(\mathbf{k}) &= \frac{-1}{V}\sum_{\mathbf{k}'} V(\mathbf{k},\mathbf{k}')\frac{1-2f(E_+(\mathbf{k}'))}{2E+(\mathbf{k}')}\Delta_+(\mathbf{k}')
\end{aligned} \tag{3.39}$$

$$M = \frac{1}{V}\sum_{\mathbf{k}}\left\{\frac{\epsilon^{\uparrow}_{\mathbf{k}}[1-2f(E_-)]}{2E_-(\mathbf{k})} - \frac{\epsilon^{\downarrow}_{\mathbf{k}}[1-2f(E_+)]}{2E_+(\mathbf{k})}\right\}. \tag{3.40}$$

Δ_+ and Δ_- are the pairing gap functions for up-up and down-down spin states, respectively, $\epsilon_{\mathbf{k}^{\uparrow,\downarrow}} \equiv \epsilon_{\mathbf{k}} \pm \frac{IM}{2}$, and the equations are coupled to each other through the excitation energy spectrum

$$E_{\pm}(\mathbf{k}) = \sqrt{\left(\epsilon_{\mathbf{k}} \mp \frac{IM}{2}\right)^2 + |\Delta_{\pm}(\mathbf{k})|^2}. \tag{3.41}$$

One of the new features is that the gap function has a **k**-dependence, as does the pairing interaction function $V(\mathbf{k},\mathbf{k}')$. In the p-channel, these quantities are treated in a standard way, i.e., $V(\mathbf{k},\mathbf{k}') = g_{l=1}(k,k')\sum_{m=-1}^{1} Y_{1m}(\hat{\mathbf{k}})Y^*_{1m}(\hat{\mathbf{k}}')$, where g is zero everywhere except within a Debye energy of the Fermi surface, and $\Delta_{\pm}(\mathbf{k}) = \Delta_{0\pm}Y_1^{\pm 1}$. The spherical harmonics $Y_{lm}(\theta\phi)$ introduce a simple angular- dependence into the equations.

There are three coupled equations that are solved self-consistently as a function of temperature and/or coupling constants. At zero temperature, the paramagnetic state ($M = 0$) is achieved by setting the magnetic coupling $I \leq 1$, and in this case the superconducting order parameters are equal, $\Delta_+ = \Delta_-$. For a finite magnetization, these two spin pairing states (if finite) are not equal, and therefore M then a non-unitary triplet state.

The somewhat complicated temperature-dependent solutions from equations (3.39, 3.40) of the coupled order parameters are given in Figure 3.19. The ferromagnetic state with no superconductivity is given by the solid line, which displays simple mean-field behavior, ending at the Curie temperature T_m. The important features occur when g_1 is turned on to produce the coexistent regime. Firstly, when the parameters are such so that there is no down-down spin pairing or gap ($\Delta_- = 0$), the magnetization follows the dotted line, and the up-up spin gap (Δ_+) is as labeled.

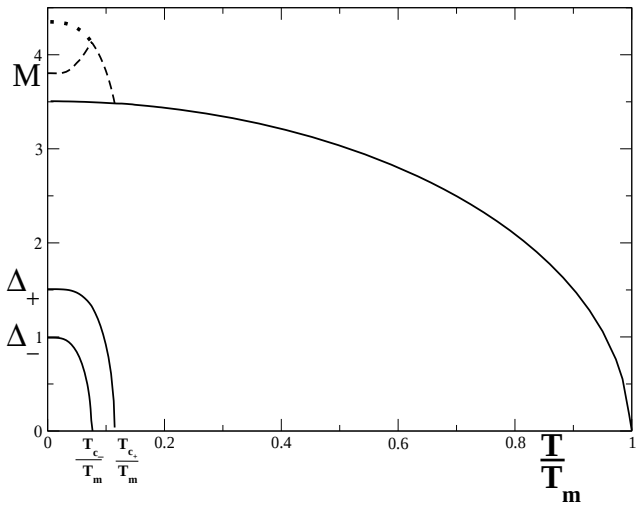

Figure 3.19 Order parameters vs. temperature (scaled by the Curie temperature T_m). The solid line is the pure ferromagnetic curve with $g = \Delta_{\pm} = 0$. The dashed line is M when $\Delta_+ > \Delta_- \neq 0$, and the dotted line is M for $\Delta_+ \neq 0$ but $\Delta_- = 0$. The values of the coupling are $I = 1.018$ and $g_1 = 0.95$.

It is evident that the existence of the up-up spin pairing enhances the magnetization, and when that pairing vanishes ($T = T_{c+}$), the magnetization falls back to its single phase value. Then, the system is fixed so that down-down spin pairing takes place along with up-up pairing, and study the magnetization. At very low temperatures, the magnetization (now the dashed line), which begins at a higher value than in the single phase case, actually increases with an increase in temperature. The cause of this is due to the sharp decrease of Δ_- with temperature. As the down spin pairs are being broken, they start to contribute to the magnetization upon flipping. At the down spin pairing transition temperature $T = T_{c-}$, the spin up gap is still finite since $T < T_{c+}$ and the magnetization is back on the dashed line from the previous scenario.

This behavior is intuitive and specifically the presence of two superconducting order parameters has important effects that did not arise in the s-wave case. This has consequences for the density of states and the nuclear relaxation rate.

3.7.2 Density of states

The single particle density of states can be calculated from the general expression

$$N_s^\sigma(E) = \frac{1}{(2\pi)^3}\int d\bar{p}\delta(E - E_p^\sigma), \tag{3.42}$$

where σ refers to the spin of the fermion, and the energies E_p^σ are given by (3.41). Carrying out the integration partly and using the delta function property gives

$$N_s^{\uparrow,\downarrow}(E) = \frac{1}{4\pi^2}\int_0^\pi d\theta \sin\theta \left(A^+ + A^-\right), \tag{3.43}$$

where

$$\begin{aligned} A^+ &= \frac{\sqrt{p_F^2 + 2m^*\left(\frac{\pm IM}{2} + \sqrt{E^2 - \Delta_\pm^2}\right)}}{\left|\frac{\sqrt{E^2-\Delta_\pm^2}}{2m^*E}\right|}, \\ A^- &= \frac{\sqrt{p_F^2 + 2m^*\left(\frac{\pm IM}{2} - \sqrt{E^2 - \Delta_\pm^2}\right)}}{\left|\frac{\sqrt{(E^2-\Delta_\pm^2)}}{2m^*E}\right|}. \end{aligned} \tag{3.44}$$

The $+$ sign is for the $\uparrow$ spin fermions and the $-$ sign is for $\downarrow$ spin fermions on $\Delta_\pm$, respectively. These two expressions converge to the density of states of the normal state at the Fermi level, $N(0) = \frac{m^* p_f}{\pi^2}$, in the limit of all order parameters equal to zero. For $M = 0$, the expressions correctly reduce to the density of states of the equal spin pairing triplet state superconductor, $N(E)/N(0) = E/2\int d\theta \sin\theta/\sqrt{(E^2 - \Delta^2)}$.

The $T = 0$ density of states (DOS) for positive excitation energies is plotted in Figure 3.20, where it is scaled with the normal state value $N(0)$. The inset A shows the DOS for just a triplet (ESP) superconductor when $M = 0$ and there is no difference between the up and down spins and the divergence occurs at the edge of the gap when $E = \Delta_- = \Delta_+$. The large body of the graph B shows the case when all three order parameters are nonzero, and the up and down spin curves have split to account for the internal field. The down spins DOS diverges at $E = \Delta_-$, and the up spin DOS at $E = \Delta_+$. Inset C shows the case when the down spin pairing is suppressed, and M

and Δ_+ are finite. The down spins show a normal state component which is constant with energy, since they remain unpaired and non-magnetic. The different cases of the density of states modify the nuclear relaxation rate accordingly.

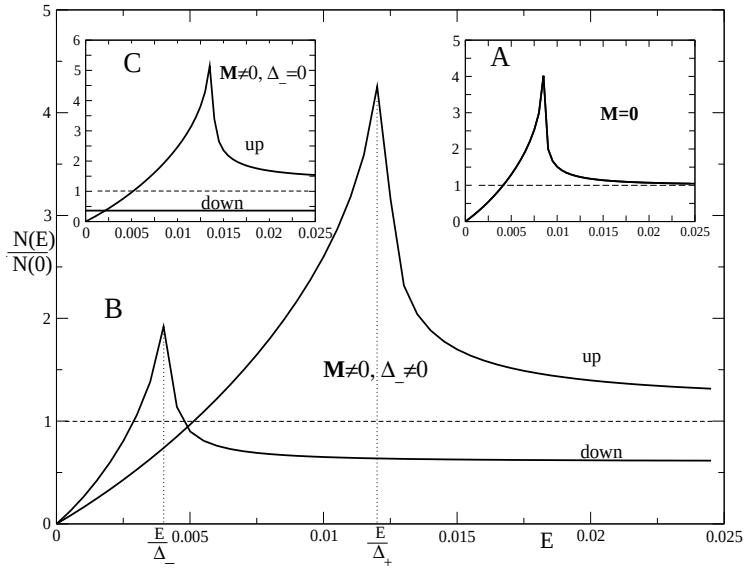

Figure 3.20 Density of states rescaled by $N(0)$ so that the horizontal dotted line corresponds to the normal state value. The different graphs are generated by varying I and g_1.

3.7.3 Nuclear relaxation rate

In general, the standard equation for nuclear relaxation in superconductors, which was not given in section 3.6.2 is

$$\frac{1}{T_1} \propto 2\int_0^\infty (N_s(E))^2 f(E)(1-f(E))dE, \tag{3.45}$$

where $N_s(E)$ is the density of superconducting states. As is the case in the s-wave coexistent formula, the magnetization changes things when introduced. Specifically, the spin up and spin down contributions to the relaxation rate will be different, and the integral will be split into two sums as

$$\frac{1}{T_1} \propto \int_0^\infty (N_s^\downarrow(E))^2 f(E_-)(1-f(E_-))dE + \int_0^\infty (N_s^\uparrow(E))^2 f(E_+)(1-f(E_+))dE. \tag{3.46}$$

The $\pm$ are the usual spin representations and the density of states equations have been derived above. The integration is carried out and the results of three different cases are shown in Figure 3.21.

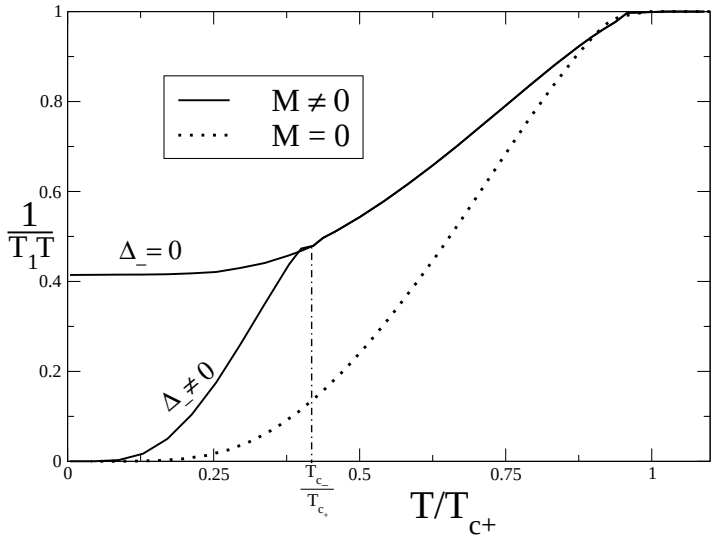

Figure 3.21 $1/T_1T$ vs. temperature scaled by the up spin transition temperature T_{c+}. The y-axis is scaled by the normal ferromagnetic state relaxation rate. The dotted line shown for reference is the non-magnetic p-wave result. The top solid line is when there is only up spin pairing, and the bottom solid line when both spin species pair, with the second transition labeled at $T = T_{c-}$. I and g are chosen so that $T_{c-}/T_c+ = 0.4$.

This plot shows all of the important features of p-wave relaxation rates. The dotted line is the curve for the non-magnetic p-wave superconductor. Below the critical temperature $T = T_{c+}$, a full gap opens up and the rate gets suppressed to zero, with no Hebel-Slichter peak, an important point, since s-wave superconductors show a very different behavior. The top solid curve is for finite M, but the down spin pairing is suppressed ($\Delta_- = 0$), and only the up spins participate in

the superconducting pairing and gapping. Thus, the effect of this gap is still prominent since the rate is moderately reduced as the temperature falls below T_c, but the magnetization and the down spins contribute a normal component to the system. The rate never gets suppressed to zero because there are states around the Fermi surface that act like a Fermi liquid ($1/T_1T \sim const$), as displayed in the s-wave case with the gapless excitations.

The bottom solid curve allows for the down spins to subsequently pair at a lower temperature ($\Delta_- \neq 0$). There is a second transition at $T_{c-}/T_{c+} = 0.4$, a second gap opens up, and the relaxation rate goes to zero at $T = 0$, following closely the non-magnetic case curve at very small temperatures. In all of these situations the absence of the Hebel-Slichter peak is expected because of the pairing, but the magnetization does not seem to be playing as large a role as it did previously for the s-wave case where it was the parameter that 'tuned' the size of the peak or even washed it out completely. There is no peak to begin with in this case, and the curves are just shifted slightly when M is finite and the temperatures are well below the Curie temperature.

Finally, Figure 3.22 is a plot of experimental data [6] taken at $13kbar$ in UGe_2, along with the curves of the s-wave and p-wave coexistent models. At this pressure the superconductivity appears below $1K$ in UGe_2. The data is not extremely consistent, particularly near T_c due to difficulties in the measurement.

Well above the critical temperature, yet still in the ferromagnetic state, the models agree relatively well with each other and with the experiment. The important regime is near and just below T_c however, and contrary to the claims of the authors of the experimental paper, a small peak is somewhat discernible. Near zero temperature, the s-wave model has much more weight than the other two since the gaplessness has a strong effect in that case. The experiments and the p-wave case display power law behavior. There does not seem to be a second transition in the experimental data, corresponding to a pairing of the minority spin species as predicted in the model, but the temperature at which this is predicted is about 5 times below those which were reached experimentally.

To conclude this section, a p-wave model was introduced into the overall analysis to set up a simple comparison scheme with experiment. However, from the data, no conclusions can be made

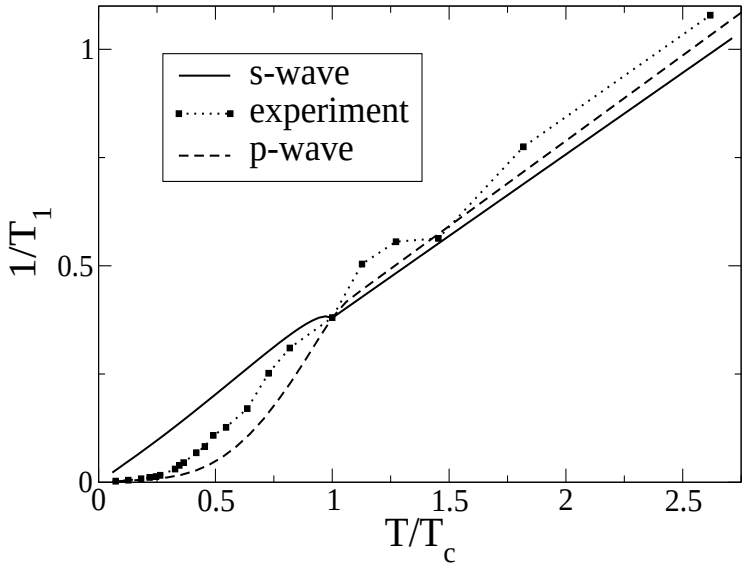

Figure 3.22 Comparison of s-wave and p-wave theoretical models with experimental data of UGe_2 [6]. The p-wave curve is calculated for only up-spin pairing, therefore only one transition occurs, at $T = T_c$.

at this point as to which pairing type is favored in the SC channel. S-wave pairing cannot be ruled out in UGe_2 from the data at hand. This is a significant point because ultimately what proves a theory is experimental verification. The data is inconclusive until further measurements are completed.

3.8 Discussion

As mentioned in the beginning of the chapter, the criticisms of the s-wave theory are due to the fact that the energy of the non-magnetic BCS superconducting state is always the lowest compared to the normal, ferromagnetic, and coexistent state. This criticism is given clearly in [53], and I have addressed this in the description of the model in this chapter. The main energy concern I have emphasized is the competition between the coexistent and the ferromagnetic states. It

was found that in a range of parameter space the FM/SC state is favored over the FM state. A glimpse of this solution was first seen in an older article by Lei *et al*.[29] in Figure 6 of that paper, where a subtle crossover of the energies is seen. We have zoomed in on that region and explored it more thoroughly. Another paper by Cuoco *et al*. [41] also studies a spin-singlet superconducting ferromagnet and finds that the FM/SC state has a lower energy than the FM state, where the renormalization of the band mass is responsible for an increase in the kinetic exchange and a lowering of the total energy. The basic model is exactly the same. By varying the coupling constants in our model, we do not know exactly what is changing physically, since the couplings could be related to many other properties like the effective mass. It very well could be that by varying g and J the system is changing in the same way as seen in that s-wave model [41].

An often used physical argument against the possibility of s-wave singlet pairing in UGe_2 is that since the spin-splitting (Zeeman energy) is about $70meV$ [15], there cannot be up-spin and down-spin fermions paired into a zero momentum state. That energy is just too large to overcome for pairing to occur. It is not clear if it is important that this energy splitting is larger than the Debye energy, since this superconductivity seems to be spin-mediated, not phonon-mediated. There are, though, other creative ways that two spins can pair. Consider Figure 3.23.

There are two ways in this figure which demonstrate momentum-space pairing. One way, labeled by **2**, is the conventional way as two opposite spins in their respective Fermi seas form a Cooper pair with with total momentum zero. The second, labeled by **1**, is the result of a low energy spin flip process that takes an up-spin from its (grey) Fermi sea and flips it, leaving behind a hole and putting the resulting down spin just above the Fermi surface. Then this down-spin at momentum $\vec{p}$ is able to pair with the appropriate up-spin at momentum $-\vec{p}$. The spin flip is a low energy, long wavelength process that has nothing to do with the Zeeman energy. Another way to understand this process is in a real-space representation, as in Figure 3.24.

If the spin flip occurs with a sufficiently large wavelength, then the magnetic correlations are not affected at all by this type of pairing, which is a collective effect. In the Figure 3.24, the up-spin on the far right is paired in a singlet with the down-spin on the far left, and the magnetization

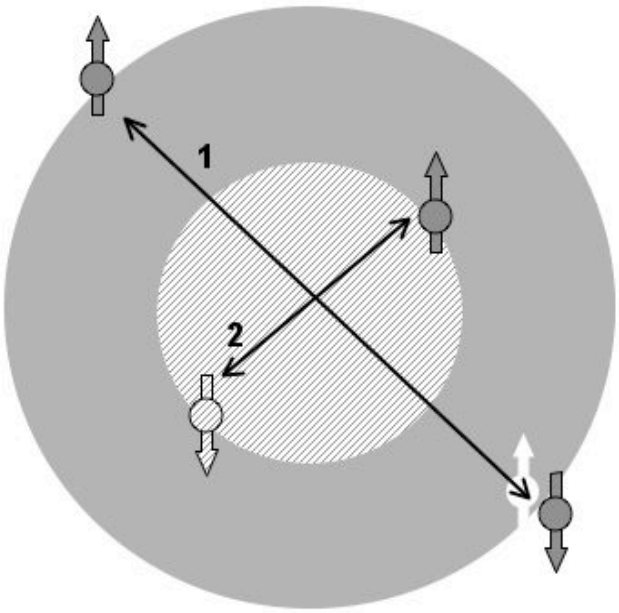

Figure 3.23 Momentum-space representation of 2 different ways for singlet pairing. The lightly shaded sphere is the down-spin Fermi sphere and the grey, larger one denotes the majority up-spin volume.

remains as long as the superconducting coherence length ξ_{SC} is larger than the ferromagnetic correlation length λ_F. In UGe_2, this seems to be the case, with $\xi_{SC} = 150-300\mathring{A}$ and $\lambda_F = 100\mathring{A}$.

Another, more technical criticism, concerns the use of a self-consistent, mean field approach (Hubbard-Stratonovich transformation) to derive coexistence in a single band model [58]. The authors of the critique show that this treatment, recast in a more transparent Hartree-Fock language,

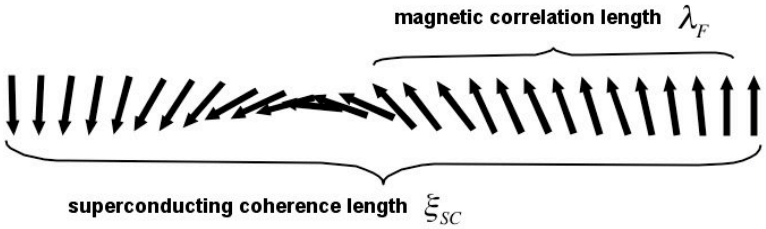

Figure 3.24 Real-space representation of the pairing in a superconducting ferromagnet.

yields a similar Hamiltonian but with just one effective coupling constant, not two. In light of this, there are only phase transitions between one state - either the SC or FM - and the other, and the coexistent state FM/SC never appears. It is argued that varying the single coupling constant only induces transitions from one single state to another. Technically, this criticism is valid, but as explained in a reply [59], it misses the point of the intent of these studies. As mentioned in this chapter, the original motivation was the fact that in a local Fermi liquid, an s-wave pairing instability was shown to exist in the ferromagnetic state. The mean field model was subsequently used to give a ferromagnetic state by a breaking of the spin symmetry, which is one of the only ways we know how to generate ferromagnetism analytically. The s-wave pairing is then introduced within this state. The rest of the calculations enable one to study the physics that comes out of the coexistent state. One may think of the two band models of Suhl [38] and Abrikosov [39] as being the correct microscopic derivation of the s-wave coexistent state, and the model studied in this chapter as the one more amenable to the analysis of the temperature-dependent physical properties. In conclusion, we feel that our contribution gives useful insight into the compex phenomenon of superconducting ferromagnets.

Chapter 4

First order phase transitions in weak ferromagnetic metals

In section 2.1.5 it was pointed out that the magnetic transitions near the critical point in UGe_2 have been confirmed to be of the first order [3], rather than second order as had been previously thought, and therefore there is no quantum critical point (QCP). There seem to be few, if any, theoretical calculations of a first order phase transition at zero temperature [60, 61]. In this chapter a theory is presented that explains the behavior of UGe_2 as a quantum fluctuation driven, first order phase transition that occurs around what we name a quantum triple point (QTP). Also suggested is a reason for why the superconductivity only appears on the ferromagnetic side of these phase transitions, as shown in the last chapter.

4.1 Induced interactions

To develop a theory that may explain why first order phase transitions occur in weak ferromagnets, we turn to work first carried out by Babu and Brown in the 1970's [62]. They developed what they called the 'Induced Interaction Model,' which was a theory to handle a many-body system of fermions, particularly used for the study of ^3He. This theory was later modified for more general cases by Bedell and collaborators ([63, 64] and the references therein). This theory will be explained briefly in the context of standard Fermi liquid theory, and I refer the reader to the original publications for full details.

The Landau Fermi liquid interaction f is an interaction between two fermionic quasiparticles. The induced interaction model makes the assumption that this can be split into a 'direct' term plus an 'induced' term, i.e., $f = f_{dir} + f_{ind}$. The induced interaction is the long range part of

the quasiparticle interaction, where one quasiparticle interacts with another via the many-body medium. Diagramatically, one way of looking at it is in Figure 4.1, where the induced interaction is derived by functionally differentiating the self-energy at the broken lines.

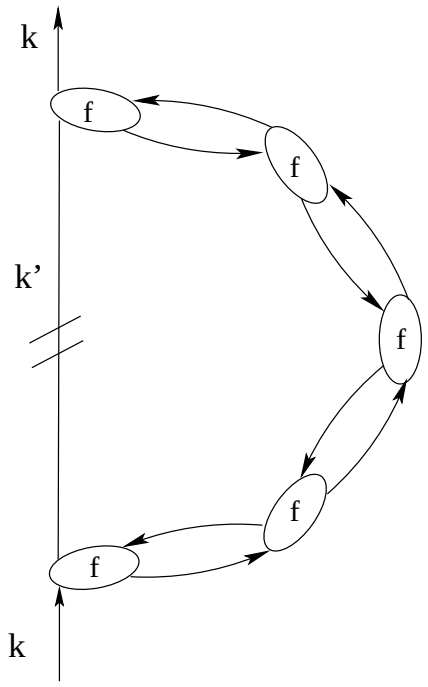

Figure 4.1 The self-energy diagram for multiple scattering can be differentiated at the broken lines to obtain the f_{ind} term.

The induced interaction is then defined as the interaction that is reducible by cutting a particle and a hole line, and this corresponds to the exchange of one collective excitation. The direct interaction is irreducible in any particle-hole channel and takes into account multi-exchange processes.

The ultimate goal of this procedure is to derive a properly antimsymmetrized scattering amplitude a. The induced term of the decomposition is an exchange term, actually, the Pauli exchange term of the particle-particle interaction [63], and if the scattering amplitude is to be antisymmetric, the direct term must also be made to be antisymmetric. In Fermi liquid language, this implies that $\sum_\ell^\infty (D_\ell^s + D_\ell^a) = 0$, where the $D_\ell^{s,a}$ denotes the direct interaction and the superscripts are the usual spin-symmetric and antisymmetric components. It is important to note that the direct interaction is model-dependent, it gives information on the underlying Hamiltonian. To be more

explicit, we will use a contact, Stoner-like or Hubbard-like repulsive interaction, which has zero range. It will also be a spatially symmetric interaction since only the $l = 0$ terms are kept.

The result of this construction is summarized nicely in Figure 4.2. The top diagram is the decomposition of f into the direct term and the induced term. The bottom diagram is the fully antisymmetrized scattering amplitude a. The induced part of a) is the exchange of all topologically equivalent diagrams of b). This implies that the induced interaction is a purely quantum effect (exchange), arising from the exchange diagrams that are required to antisymmetrize the effective two-body scattering amplitude. This is the source of the first order phase transition in the model.

The equations for the Fermi liquid parameters with which we are interested in working can now be taken from the diagrams of Figure 4.2. Remembering that the interaction in a Fermi liquid can be expressed as

$$F^{\sigma\sigma'}_{pp'} = F^{s}_{pp'} + F^{a}_{pp'}\vec{\sigma}\cdot\vec{\sigma}', \tag{4.1}$$

the final result, keeping just the $\ell = 0$ terms of the induced interactions are

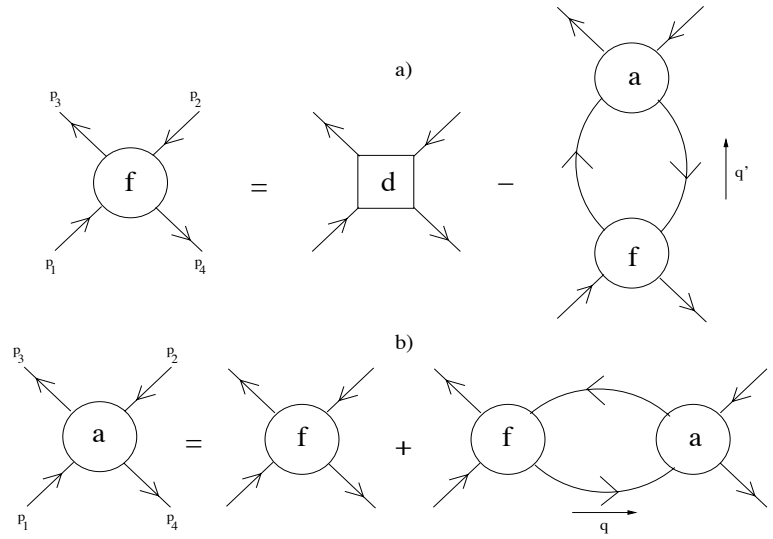

Figure 4.2 The schematic integral equations for the Fermi liquid parameter f and the scattering amplitudes a. The p's are the incoming and outgoing quasiparticle momenta. The direct term d is irreducible in the particle-hole channel while b) contains the fully reducible set of diagrams. q is the momentum transfer $q = p_1 - p_3$, while $q' = p_1 - p_4$ is the exchange momentum transfer in the induced interactions.

$$F^s_{pp'} = D^s_{pp'} + \frac{1}{2}\frac{F^s_0\chi_0(q')F^s_0}{1+F^s_0\chi_0(q')} + \frac{3}{2}\frac{F^a_0\chi_0(q')F^a_0}{1+F^a_0\chi_0(q')} \tag{4.2}$$

$$F^a_{pp'} = D^a_{pp'} + \frac{1}{2}\frac{F^s_0\chi_0(q')F^s_0}{1+F^s_0\chi_0(q')} - \frac{1}{2}\frac{F^a_0\chi_0(q')F^a_0}{1+F^a_0\chi_0(q')}. \tag{4.3}$$

As before, the Fermi liquid parameters are made dimensionless by multiplication by the density of states, so that $F = fN(0)$ where $N(0) = m^* p_F/\pi^2$. The exchange particle-hole channel momentum transfer is $\vec{q}'$, where $\vec{q}'^2 = |\vec{p} - \vec{p}'|^2 = k_F^2(1-\cos\theta_{pp'})$ and $\cos\theta_{pp'} = \hat{p}\cdot\hat{p}'$. The momenta from Figure 4.2 have been redefined so that $\vec{p} = \vec{p}_1$ and $\vec{p}' = \vec{p}_4$. The direct terms $D^{s,a}_{pp'}$ are defined in the next section where a specific microscopic model parameter is considered. The other model-dependent quantity in (4.2, 4.3) is the susceptibility $\chi_0(q')$, which is just the Lindhard function given by

$$\chi_0(q') = \frac{1}{2}\left[1 + \left(\frac{q'}{4k_F} - \frac{k_F}{q'}\right)\ln\left|\frac{k_F - q'/2}{k_F + q'/2}\right|\right]. \tag{4.4}$$

The expressions above can be extended up to any order, but only the $\ell = 0$ parameters are needed. Any higher order moment can be projected out of these expressions.

4.2 LFL and induced interactions

The induced interactions are a very general framework for calculating the Fermi liquid parameters. We are going to use them here in the context of the ferromagnetic local Fermi liquid (LFL) that was studied in the previous chapter. The LFL itself cannot give information based on physical input parameters because it is derived from phenomenological considerations and sum rules. It also tells us nothing about phase transitions. That is where the induced interaction model comes in because it has some microscopic foundation and model-dependence. It will be useful to remember the solutions in the LFL: for the ferromagnetic case (as written below (3.7)) $F^s_0 \to -1^+$ and $F^a_0 \to -1^-$; for the paramagnet, $F^s_0 \to \infty$ and $F^a_0 \to -1/2$.

To describe a LFL using the induced interaction theory, we first suppress all Fermi liquid parameters for $\ell > 0$.[1], This simplifies the calculation but also gives non-trivial results. Then the momentum transfer in the exchange particle-hole channel, $\vec{q'}$, is set to zero, and (4.4) just becomes $\chi_0(q' = 0) = 1$. The direct interaction is defined as the Hubbard U, which is a postive, repulsive contact interaction. The direct interaction is given formally as

$$D_0^s = -D_0^a = \frac{N(0)}{2}U = \frac{\bar{U}}{2}, \tag{4.5}$$

which is antisymmetric; thus $D_0^{\uparrow\uparrow} = D_0^s + D_0^a = 0$. This definition of the direct interaction is similar to that of the Stoner model, however, in that model there is no induced interaction terms which deal with longer range interactions. Having adapted the induced interactions to the LFL, a simple set of coupled equations from (4.2, 4.3) arise which can be written as

$$\begin{aligned} F_0^s &= D_0^s + \frac{1}{2}F_0^s A_0^s + \frac{3}{2}F_0^a A_0^a \\ F_0^a &= D_0^a + \frac{1}{2}F_0^s A_0^s - \frac{1}{2}F_0^a A_0^a. \end{aligned} \tag{4.6}$$

From (3.2), the scattering amplitudes are defined by $A_0^{s,a} = F_0^{s,a}/(1 + F_0^{s,a})$. These two equations are just algebraic and thus very simple to solve for F_0^s and F_0^a. For large U, the solutions are exactly what was found in the LFL! The results are shown succinctly in Figure 4.3. What is happening is that the effective field theory, which contains quantum exchange diagrams (and fluctuations), reproduces exactly the results of the LFL [65].

There are three solutions to (4.6), shown graphically in Figure 4.3.

1. The paramagnetic solution where, for large $\bar{U}$, $F_0^s \cong \bar{U}$ and $F_0^a \cong -1/2$. This is the only real solution at $\bar{U} = 0$ (left panel).

2. The ferromagnetic solution, where, as seen before $F_0^s \cong -1^+$ and $F_0^a \cong -1^-$ as $\bar{U} \to \infty$. This solution is imaginary at $\bar{U} = 0$ and remains so until about $\bar{U} \approx 10$ (middle panel).

[1]Technically, this means 'projecting out' the $l = 0$ moments of (4.2, 4.3). This is done by multiplying both sides by $\frac{2l+1}{2}\int_{-1}^{-1} P_l(x)$ with $l = 0$, where $P_l(x)$ are the Legendre polynomials and $x = \cos\theta_{pp'}$. Carrying out the simple integration in this case gives $F_0^{s,a}$ on the left side of the equations.

3. A 3^{rd} solution which corresponds to $F_0^s \cong -1/2$ and $F_0^a \approx -\bar{U}/3$ for large $\bar{U}$ (right panel). It is also imaginary for small $\bar{U}$, but then becomes real where the ferromagnetic solution becomes real. This solution might correspond to a large moment ferromagnet, but this hypothesis will be examined in a future publication and not in this thesis.

4.3 Phase transition in the induced interactions

To sketch the preliminary qualitative evidence of the phase transition, one can imagine the system at some certain large value of U to be in a certain state, for example, the ferromagnetic state. Since the system can be in any one of three states at this U, it can jump from the ferromagnetic state to the paramagnetic state, for instance, for a small change of U. This is an abrupt change in the system, and it is in fact a first order phase transition. To study this in a quantitative way, we must look at the energy of each phase to determine which one is lowest. In fact, it will be the chemical potential that will be the important quantity, and where the chemical potentials of each

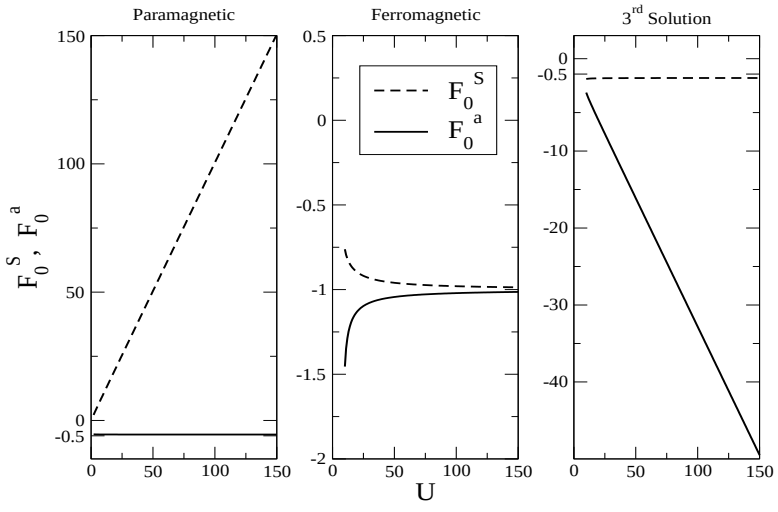

Figure 4.3 The three solutions to (4.6). The x-axis is $\bar{U} = N(0)U$ for all three plots. In some plots the y-axis is rescaled for clarity. In the two rightmost panels, the Fermi liquid parameters do not have real values until $\bar{U} \approx 10$. The dotted line in each panel is F_0^s, and the solid line is F_0^a.

respective phase cross is where the first order phase transition occurs. It will also be shown that at zero temperatures and small, finite temperatures, the magnetization shows a discontinuous jump.

The method used to carry out this analysis will employ aspects of spin-polarized Fermi liquid theory [66, 67]. This theory examines the magnetization dependence of the Fermi liquid parameters, which is important in the ferromagnetic phase, and can produce a number of useful relations from the thermodynamic considerations of the system.

4.3.1 Chemical potential

So far all that has been done is a sketch of a method that calculates the Fermi liquid parameters in the induced interactions as a function of U. It is important to connect the Fermi liquid parameters to physical quantitites so that we can drive the quantities through a phase transition as described above. In a spin-polarized Fermi liquid, the change in the chemical potential can be expressed, using thermodynamic considerations [66] as $\delta\mu = (1/2)(C^{\uparrow\uparrow} - C^{\downarrow\downarrow})\delta m$, where $C^{\sigma\sigma} = 1/N^{\sigma}(0) + \tilde{f}_0^{\sigma\sigma}$. $N^{\sigma}(0) = k_F^{\sigma} m_{\sigma}^{*}/2\pi^2$ is the density of the states at the Fermi surface of spin σ. The tilde distinguishes that the Landau parameters are in the polarized state, and are given (to quadratic order) by

$$\begin{aligned} \tilde{f}_0^{\sigma\sigma} &= f_0^{\uparrow\uparrow}(1 - b_0\sigma\Delta + b_1\Delta^2) \\ \tilde{f}_0^{\uparrow\downarrow} &= f_0^{\uparrow\downarrow}(1 + c_1\Delta^2), \end{aligned} \tag{4.7}$$

where Δ, the polarization, is m/n, and the b_i and c_i are coefficients that can be determined from sum rules and physical considerations.

The chemical potential is now a function of the parameters of the theory, and a general Taylor expansion can be done around the critical chemical potential μ_c in the vicinity of a critical U_c for each phase where the phase transition takes place, as

$$\mu_F(U) \approx \mu_c(U_c) + (U - U_c)\frac{d\mu_F}{dU}|_{U=U_c} \tag{4.8}$$

$$\mu_P(U) \approx \mu_c(U_c) + (U - U_c)\frac{d\mu_P}{dU}|_{U=U_c}. \tag{4.9}$$

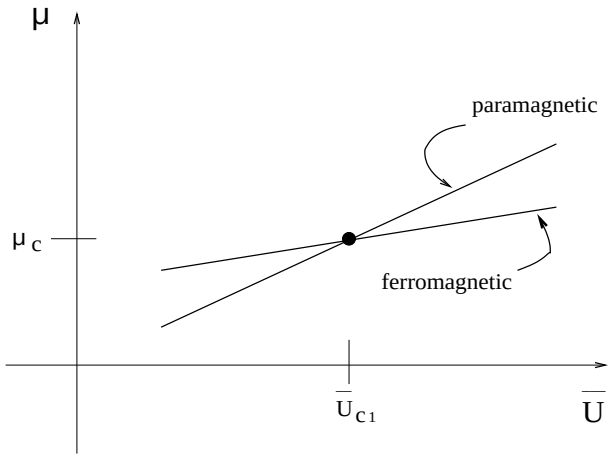

Figure 4.4 The chemical potentials expanded about the critical U_c. The paramagnet, which is favored energetically at small U, gives way to the ferromagnet at $U = U_c$.

The chemical potential is differentiated in the ferromagnetic state implicitly through the magnetization, which is defined for a weak ferromagnet as $m \sim |1 + F_0^a(U)|^\alpha$. The exponent α depends on the order to which the Ginzburg-Landau expansion in the free energy is carried out. In this case we stop at m^4 and still derive a first order transition, and therefore $\alpha = 1/2$ (for m^6, $\alpha = 1/4$, etc.).

The one extreme, for $U = 0$, is known to be a paramagnet. In fact, in this model, the only real solution of the induced interactions is the paramagnetic one. For very large U, $F_0^a \to -1$ (Fig. 4.3), so the magnetization goes to zero and the paramagnetic state is once again favored. The transitions from one to the other in the vicinity of the critical point are shown in Figure 4.4 where the chemical potentials are plotted. The plot is the results of the calculations in equation (4.9). The crossing of the chemical potentials is a clear indication of a first order transition, and the ferromagnetic state has the lower energy at the higher U values. At a much larger U the paramagnetic state is again favored as the magnetization goes to zero.

4.3.2 Magnetization

There is a zero-temperature first order phase transition that must be driven by the quantum fluctuations in the induced interactions. What happens at small but finite temperatures? To answer

this, some basic Maxwell relations are used within the polarized Fermi liquid language. Much of the details have been carried out in [66, 67].

The first step is to integrate the Maxwell relation $-(\partial s/\partial n)_{T,m} = (\partial\mu/\partial T)_{n,m}$ with respect to temperature to get the finite-magnetization, finite-temperature chemical potential:

$$\mu(m,T) = \mu(m,T=0) - \frac{\partial N(0)}{\partial n}\frac{\pi^2}{6}T^2 + E_1 m^2 \frac{\pi^2}{6}T^2 + E_2 m^4 \frac{\pi^2}{6}T^2, \tag{4.10}$$

where some of the coefficients are functions of the density of states and the parameters of (4.7). A similar procedure is used to develop the finite-temperature free energy (up to fourth order in the magnetization) which is given as

$$f(m,T) = f(0,0) + \frac{1}{2}A_1 m^2 + \frac{1}{4}A_2 m^4 - N(0)\frac{\pi^2}{6}T^2 + \frac{1}{2}D_1 m^2 \frac{\pi^2}{6}T^2 + \frac{1}{4}D_2 m^4 \frac{\pi^2}{6}T^2. \tag{4.11}$$

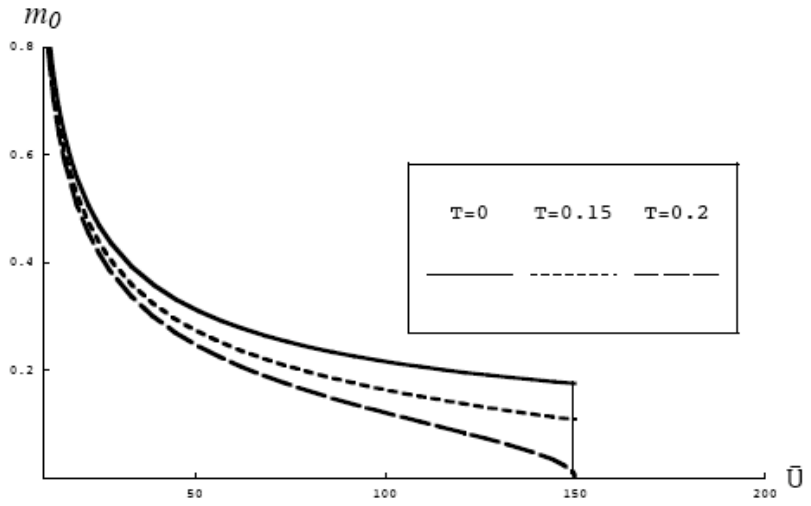

Figure 4.5 The magnetization as a function of the effective interaction $\bar{U} = N(0)U$ for different T. The temperatures in this model are scaled by the spin fluctuation temperature, which is about $1/100$ of the Fermi temperature for these interaction strengths. The moment drops discontinuously to zero for the top two curves, shown by the vertical line, indicating first order behavior. At a critical temperature $T_c = 0.2$, the magnetization goes continuously to zero. Above this temperature all of the transitions are of second order. The magnetization for small values of $\bar{U}$ is not relevant since the paramagnet is energetically favored there, and can be ignored.

This expression can then be differentiated to find the magnetization as a function of temperature in zero external field. The temperature-dependence of the magnetization is calculated to see what becomes of the first order transition as the temperature is increased. Initially, at zero temperature, the magnetization drops discontinuously to zero at some U_c. This is dictated by the chemical potential. As the temperature is increased, one expects to eventually see the system slowly exhibit a continuous transition as dictated by the free energy. Then the magnetization would be suppressed to zero without a discontinuity. This is exactly what is seen in Figure 4.5. The $T = 0$ behavior is shown by the top curve. It drops discontinuously to zero where the chemical potentials cross, and the vertical line depicts this. At a small but finite temperature, the transition remains first order. The temperature is then raised slightly more to a critical temperature $T_c = 0.2$ (the scaled temperature is explained in the caption) where the transition is now a continuous second order one. Any temperature greater than this critical T thus gives a second order transition.

4.4 Phase diagram

Having studied the zero temperature and the small temperature behavior of the order parameter, it is inmportant to look at the whole phase diagram in $T - P$ space. To do this, an expression is needed for the pressure that connects with the physical parameter U using thermodynamical relations as was done for the free energy and chemical potential. Since $P = -f + \mu n + Hm$, the necessary tools are in place, and following [66], one finds

$$\begin{aligned} P(m,T) = P(0,0) \quad &+ \quad N(0)\frac{\pi^2}{6}T^2 - n\frac{\partial N(0)}{\partial n}\frac{\pi^2}{6}T^2 + G_1 m^2 + G_2 m^4 \\ &+ \quad G_3 m^2 \frac{\pi^2}{6}T^2 + G_4 m^4 \frac{\pi^2}{6}T^2, \end{aligned} \tag{4.12}$$

the coefficients defined in the references. Using this result a phase diagram is mapped out and presented in Figure 4.6. The region of interest is near what we call the quantum triple point (QTP). The high temperature behavior is extrapolated from previous theories since this model is not necessarily valid at such high temperatures. Also, the superconductivity shown in the figure is not produced explicitly by this model, although the local Fermi liquid model, to which this theory

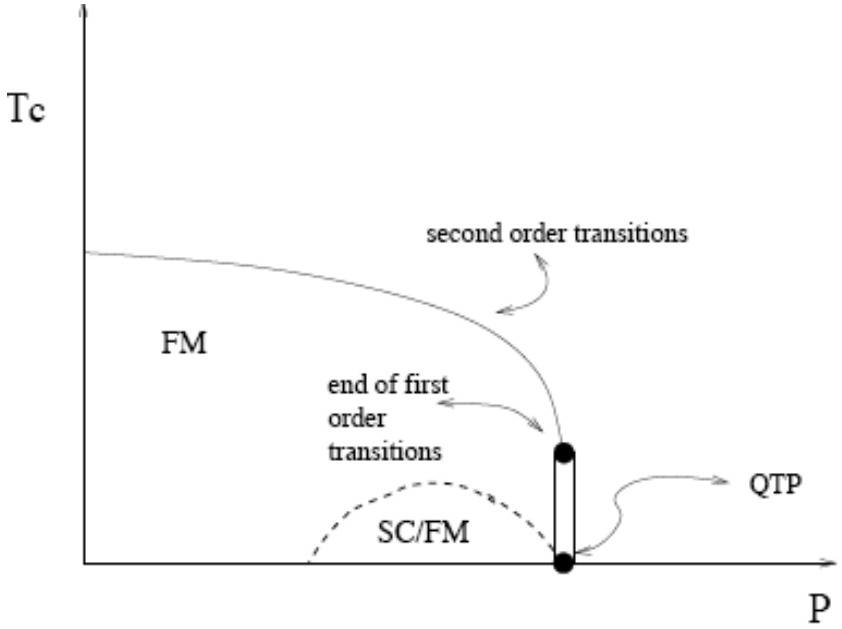

Figure 4.6 T_c vs P phase diagram generated in this model. The double line indicates the line of first order transitions, which ends at a finite T as shown in the text and figure 4.5. The SC dome is taken from [5, 7].

is related, does give superconductivity near the ferromagnetic-paramagnetic transition (Chapter 3, [5]).

Notice the steep slope of the line of first order transitions which is due to the fact that the latent heat of the transitions, which is zero at $T = 0$, is also zero or nearly zero at small temperatures. This is because the entropy difference between the FM and PM states is proportional to the density of states difference on each side, which to leading order is zero in this model, and to next order is $O(m^2)$ with m small. Thus these transitions are weakly first order, as seen experimentally.

Comparing this to UGe_2 which has a strikingly similar phase diagram, we can study the energy scales. The effective chosen $\bar{U}_c = N(0)U_c = 150$ where the first order transitions occur. From a calculation of the density of states of UGe_2 [40] it is found that at the Fermi level $N(0) \sim 20/eV$. This gives a U in the range of $10eV$, a typical value for correlated electron systems. The (scaled) critical temperature of $T_c = 0.2$ gives, when a typical Fermi temperature of $1eV$ is used, a real critical temperature of about $1meV$, or about $10K$. This is the same temperature at which the first order transitions end and the second order ones begin in UGe_2.

4.5 Conclusions

It has been shown that including the quantum fluctuations of the induced interactions drives a first order phase transition in the itinerant weak ferromagnets. In fact, if the quantum induced terms are turned off, a simple second order magnetic (Stoner) phase transition is recovered [65]. An interesting point can be made thermodynamically to explain why there is no phase observed on the paramagnetic side even though much theoretical work has predicted a superconducting phase there. The QTP has three phases ending at it at zero temperature (see Figure 4.6). According to the Gibbs phase rule [68], a single component system, which we have here in zero external field, can only accomodate a maximum of three phases coexisting at a point. This restriction explains why there is only superconductivity on one side of the QPT. In fact, it is becoming clearer that the transitions into the superconducting state may also be of first order, and although this point is still not completely verified [69], it is consistent with the theory in this chapter since the diverging length scales are suppressed by the magnetic first order transitions. Therefore, possibly all divergences in the system are suppressed and the superconductivity is discontinuous as well.

There have been other attempts at examining theoretically first order phase transitions in itinerant ferromagnets [70, 71, 47], but the theory presented in this chapter is the only one in which the transitions are driven solely by quantum fluctuations, and the results of this calculation are in general agreement with other field-theoretical treatments.

Chapter 5

Spin-density wave transition in weak ferromagnetic metals

As noted in section 2.1.3, UGe_2 has a curious anomaly in the phase diagram where the resistivity changes from having Fermi liquid exponents to non-Fermi liquid exponents as the temperature is increased in most of the pressure range. Even though it has been thought for some time that this was a signature of a possible weak spin-density wave crossover, ordering at a finite wavevector was never observed in neutron experiments. This artifact has remained a mystery up until very recently, but new experiments have shown evidence for a real spin-density/charge-density wave transition in the specific heat at ambient pressure in UGe_2 [8].

In this short, penultimate chapter, I simply demonstrate how a spin-density wave (SDW) or charge-density wave (CDW) phase transition can occur in general in a weak ferromagnet, and I particularly focus on the (SDW) transition, noting that the same arguments below apply to a (CDW) as well. In fact, these two transitions occur at the same wavevector, so for simplicity, I only mention the SDW. The main results of the calculation will be summarized, and the reader is referred to an upcoming publication for the full treatment [44].

5.1 Accidental discovery

The original motivation for this work stems from a calculation attempted several years ago. The problem at the outset was to study the pairing amplitudes in a ferromagnet in the local limit, but with finite-q scattering. Whereas it was known that the singlet channel was attractive and the triplet amplitude was strictly zero for $q = 0$ (Chapter 3), it was hypothesized that the inclusion

of these corrections would lead to an attractive triplet state, which would eventually even be more favorable than the singlet as more phase space was allowed for the scattering.

When calculating the finite-q contributions to the local Fermi liquid, integrals for the Fermi liquid parameters take a schematic form given as

$$F_0^{s,a} \sim \int_{q=0}^{2k_F} \frac{dq}{1 + F_0^a \chi_0(q)}. \tag{5.1}$$

In the ferromagnetic state, $F_0^a \lesssim -1$, and the Lindhard function $\chi_0(q)$ varies between $-1/2 \lesssim \chi_0(q) \leqslant 1$ as q is integrated over the limits shown above. Therefore, for some q, as long as the system is in the weak ferromagnetic limit there is a divergence and the integral is indeterminate. This frustrating result was the conclusion of that endeavor.

Two years later, an experiment of the specific heat in UGe_2 gave strong evidence of a true spin-density wave transition at low pressures and $T \approx 22K$ (the original SDW 'crossover' was thought to be at $T \approx 30K$; see Figure 2.2). This had never been observed before because no one had done the slow-cooling technique that was used in the measurement of Figure 5.1. It was then

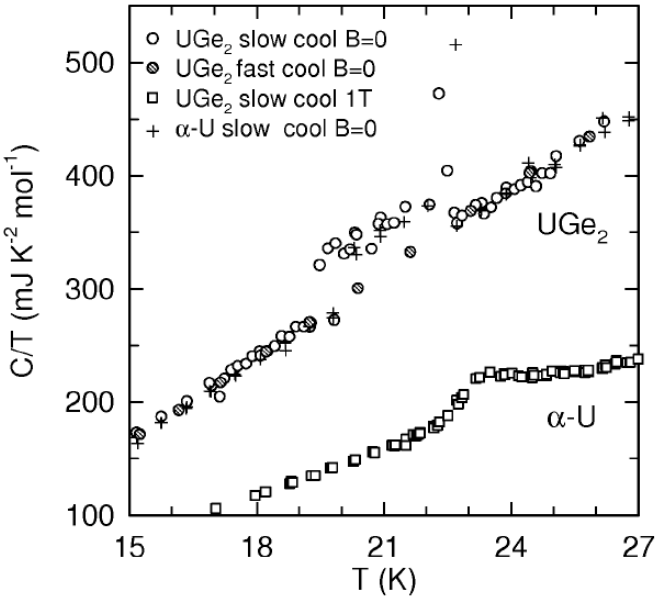

Figure 5.1 Specific heat at ambient pressure from [8]. The $\alpha-$U measurement is shown for comparison, since that material is known to have an SDW transition. Only the slow-cool method yields a phase transition signature.

realized that the divergence that occurs in the integrals of the Fermi liquid parameters also occurs in the scattering amplitudes, and could very well be a signature of a phase transition–the very phase transition we had almost discovered two years earlier.

5.2 Derivation of SDW temperature and wavevector

It can be shown without much difficulty that the q-dependent scattering amplitudes in the local Fermi liquid theory are given as

$$A_0^s(q) = \frac{F_0^s(q)}{1 + F_0^s(q)\chi_0(q)} \tag{5.2}$$

$$A_0^a(q) = \frac{F_0^a(q)}{1 + F_0^a(q)\chi_0(q)}. \tag{5.3}$$

According to this set of equations, the SDW and CDW transitions occur at the same q. For simplicity, the q-dependence of F_0^a is ignored and the focus will be on the spin-antisymmetric term, $A_0^a(q)$. Another valid approximation is to expand the Lindhard function to quadratic order in q and T, which can be carried out to give [72]

$$\chi_0(q,T) \approx 1 - \left(\frac{q}{k_F}\right)^2 \left[\frac{1}{12} + \gamma_1 \left(\frac{T}{T_F}\right)^2\right] - \gamma_2 \left(\frac{T}{T_F}\right)^2, \tag{5.4}$$

where T_F is the Fermi temperature, $\gamma_1 = \pi^2/96$, and $\gamma_2 = \pi^2/24$. The first thing that can be calculated is the Curie temperature T_c at which the ferromagnetism develops, by setting the denominator in (5.3) to zero, i.e.,

$$1 + F_0^a \chi_0(q = 0, T = T_c) = 0, \tag{5.5}$$

since the ferromagnetic transition occurs for $q = 0$. Solving for the Curie temperature gives

$$T_c^2 = \frac{1 + F_0^a}{\gamma_2 F_0^a} T_F^2. \tag{5.6}$$

Note that as $F_0^a \to -1$, $T_c \to 0$ as expected. Now one can find the SDW transition temperature T_x at some critical wavevector q_c by setting the denominator to zero accordingly as

$$1 + F_0^a \chi_0(q = q_c, T = T_x) = 0. \tag{5.7}$$

Solving for T_x gives

$$T_x^2 = \frac{T_c^2 - \frac{2}{\pi^2}\frac{q_c^2}{k_F^2}T_F^2}{1 + \frac{q_c^2}{4k_F^2}}. \tag{5.8}$$

The very important result of (5.8) is that the SDW transition temperature T_x is less than the Curie temperature as seen experimentally. Naturally, the ferromagnetic state is required to produce the SDW in this theory.

5.3 Comments

This chapter presents a short and sweet derivation of a SDW transition in a local ferromagnetic Fermi liquid in a general way. In fact, one conclusion that can be drawn is that a transition should not be observed in a somewhat strong ferromagnet since in that case, F_0^a will be more negative, and the divergence criterion of the scattering amplitudes might not be satisfied. Of course, for large moment systems, the theory might not be valid and would have to be re-derived and re-examined for these instabilities.

Equation (5.8) can be used to map out the $T_x(p)$ line at finite pressures by including the pressure-dependence of the Curie temperature, and using the pressure-dependence of q_c as a fitting parameter in the theory [44]. The fact that such a simple derivation can produce such non-trivial results, close to those measured, leads one to believe that UGe_2 can be described quite well by a local Fermi liquid.

As mentioned in the introduction to this chapter and elsewhere, a true SDW/CDW phase transition had not been verified until recently in UGe_2. Ironically, a 'slow' specific heat measurement has given the verification, not a neutron scattering experiment. The theory above can give a good reason as to why this is the case: the neutrons were looking in the wrong place. Equation (5.8)

can be inverted to get the critical wavevector at ambient pressure. Plugging in the experimental values for UGe_2 gives a q_c that is about an order of magnitude less than the q's that have been used in experiments [42, 73]. Thus, this is a very long wavelength ($\sim 35\mathring{A}$) phenomenon, apparently much longer than predicted.

Chapter 6

Atomic Fermi gases

In this final chapter I look at the recently discovered dilute Fermi gases that exhibit two interesting and exculsive phenomena: Bose-Einstein condensation (BEC) and BCS superconductivity. The crossover from one of these states to the other is obtained simply by changing the magnetic field. The physics is studied by assuming a Fermi liquid, and then applying the induced interaction framework developed in the previous chapter. In the region where the crossover occurs, the many body effects are very important and cannot be ignored as is sometimes done in the literature. We show that by taking into consideration the strong fluctuations built into the theory one can explain many experimental results that have until recently seemed somewhat anomalous.

The chapter begins with a short introduction to the experimental properties of the gases, followed by an explanation of the induced interactions as applied to them. I show why some other theories fail to give good results in this fermionic system, and prove a useful theorem along the way (Levinson). The calculations are then explained and compared to the experimental observations. The chapter is concluded with a synopsis of some ongoing and future directions of this research. [1]

[1] Much of this analysis will subsequently appear in the thesis of Sergio Gaudio with whom I have collaborated on this topic [74].

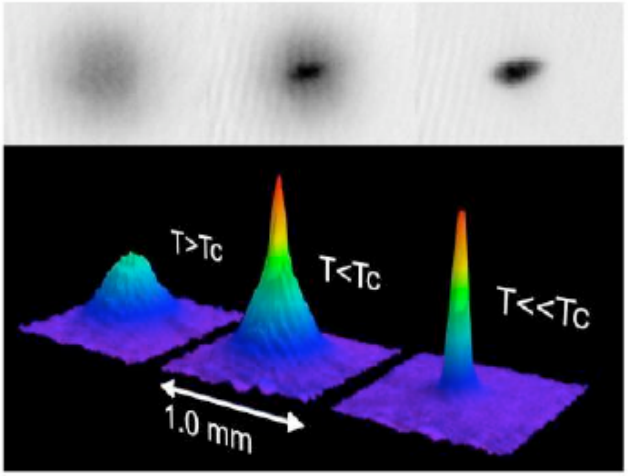

Figure 6.1 Observation of BEC in ^6Li from W. Ketterle's website. Each panel is a time of flight measurement, and what is shown is that well below the critical temperature, there are many molecules at the same point in space.

6.1 Introduction

Laser cooling advances have revolutionized research on ultracold atomic systems in recent years. Since most of the fundamental quantum physical properties of atomic gases require extremely low temperatures, a wealth of never before observed phenomena have lately been confirmed. With the help of laser cooling, Bose-Einstein condensation of bosonic atoms was observed about 10 years ago (for a nice review, see [75]).

It has been demonstrated that *bosons* may *bose*-condense, but the cooling of fermions to very low temperatures poses a problem. The only way to cool is through collisions, and identical fermions are not allowed to collide because of Pauli. Furthermore, we are taught that identical fermions cannot be in the same quantum state, a necessary condition for condensation.

This problem is circumvented in several ways. One way is to not have *identical* fermions at all, but rather fermions in two different hyperfine states. Then they can collide and lower the temperature effectively, and even form bound molecules. Another way is to consider the BCS theory of superconductivity. Imagine two fermions pairing in a Cooper pair, forming a composite *boson*, and then all of the composite bosons condensing into a common state.

In fact, this is exactly what is being discovered [76] now in certain dilute atomic Fermi gases, particularly in ^{40}K and ^{6}Li, both atomic fermions (e.g., ^{40}K has 19 protons, 19 electrons, and 21 neutrons, or 59 fermions, an odd number). These Fermi systems, at very low temperatures, display on one side of a crossover a condensed molecular bound state, and on the other side, signatures of BCS superfluidity. An example of each is shown in Figures 6.1 and 6.2.

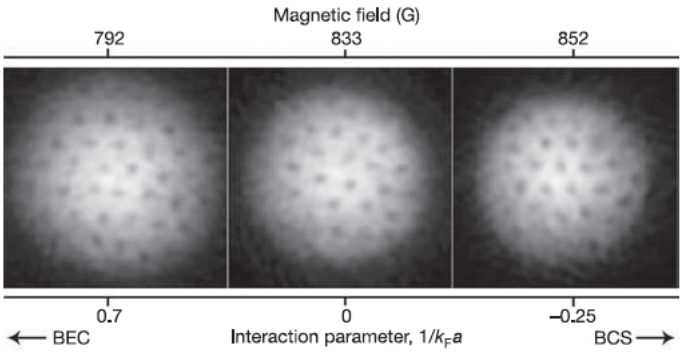

Figure 6.2 Observation of superfluidity in ^{6}Li on the BEC and BCS side [9]. What is shown is a vortex lattice, an unambiguous signature of superfluidity.

One of the basic underlying properties of these systems, one in which is of great practical interest, is the s-wave scattering length. A schematic of the scattering length in these systems is given in Figure 6.3. The crossover mentioned above is really the change in the sign of the interactions between the particles as the magnetic field sweeps through a Feshbach resonance.

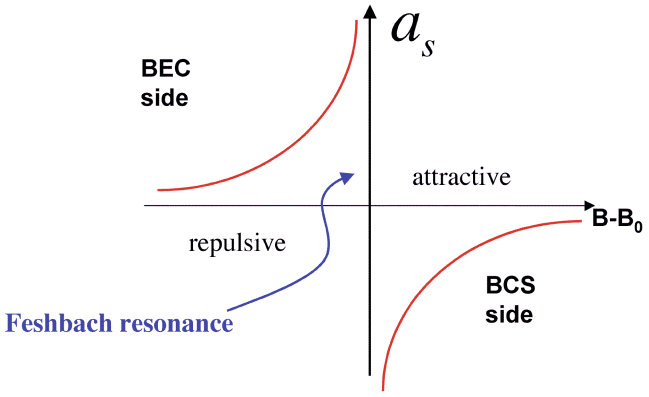

Figure 6.3 The s-wave scattering length on either side of a Feshabach resonance which is driven by an external magnetic field.

On one side (BEC), the s-wave scattering length a_s is positive, and on the other side (BCS), it is negative. Thus the interactions are repulsive and attractive respectively. The Feshbach resonance can be thought of as the situation when two colliding particles have the same energy as that of a virtual bound state. In a mean field view, near the resonance on both sides, the two-body scattering length is seen to diverge, as depicted in Figure 6.3. It diverges according to the mean field equation

$$a_s = a_{bg}\left(1 - \frac{\Delta B}{B - B_0}\right), \tag{6.1}$$

where B_0 is the value of the magnetic field at resonance, ΔB is the width of the resonance, and a_{bg} is a background scattering length given as $a_{bg} = 174 a_{Bohr}$.

A typical experimental plot of a_s is shown in Figure 6.4. A mean field line is shown in the data which characterizes a diverging scattering length. Notice that the data points do not diverge near the resonance, but seem to level off somewhat. This chapter shows that the effect of many-body exchange fluctuations, near the Feshbach resonance, suppress this mean field divergence. Away from the resonance, the system is quite dilute, and only two-body interactions are important. As one approaches the resonance however, the density increases, and many-body effects modify the interactions substantially, not allowing a divergence in the system. To show this below the induced interaction framework of Chapter 4 will be utilized.

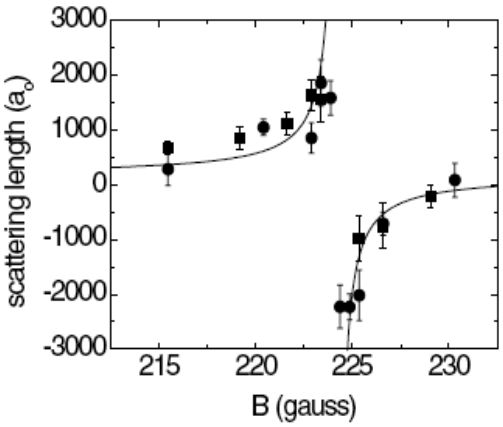

Figure 6.4 Data from a measurement of the scattering length in ^{40}K [10].

An important consequence of a finite scattering length is that the binding energy of the molecules on the BEC (repulsive) side also remains finite, which can be seen from the simple formula relating the two: $E_b = -\hbar^2/ma_s^2$. Finite binding energies are seen at the resonance, and molecules have been observed recently extending even on the attractive side [12]. The binding energies we can calculate are not only finite at resonance, but also fit nicely the magnitude of the data.

Another interesting aspect of these Fermi gases theoretically is the existence of superfluidity, and the BCS side will be examined in this chapter. It has been confirmed that the temperatures now available to experimentalists are below a critical temperature for the onset of superfluidity as evidenced by the vortex lattice and other signatures. Since we are considering the non s-wave effects in the scattering processes involved, the possibility of non s-wave pairing is very relevant to this discussion. It can be shown by including exchange effects, that a triplet superfluid is quite possible.

6.2 Induced interactions for the ultracold Fermi gases

The basic ideas of the induced interactions are explained in Chapter 4. However, as a reminder for this section I will reproduce equations (4.2, 4.3) here:

$$F^s_{pp'} = D^s_{pp'} + \frac{1}{2}\frac{F^s_0\chi_0(q')F^s_0}{1+F^s_0\chi_0(q')} + \frac{3}{2}\frac{F^a_0\chi_0(q')F^a_0}{1+F^a_0\chi_0(q')} \tag{6.2}$$

$$F^a_{pp'} = D^a_{pp'} + \frac{1}{2}\frac{F^s_0\chi_0(q')F^s_0}{1+F^s_0\chi_0(q')} - \frac{1}{2}\frac{F^a_0\chi_0(q')F^a_0}{1+F^a_0\chi_0(q')}. \tag{6.3}$$

These equations are solved self-consistently for the $\ell = 0$ Fermi liquid parameters. Contrary to the case in the last chapter for UGe_2, we want to use a finite q' to allow for exchange momentum, so that the Lindhard function (4.4) $\chi_0(q')$ is not simply equal to one. Also, the $F_1^{s,a}$ will be projected out of the equations above. Remember that $q'^2 = k_F^2(1-\cos\theta_{pp'})$, and is the momentum transfer in the exchange particle-hole channel. This is a crucial point because it is by the inclusion of the fluctuations in this channel that the suppression of the divergence near resonance is achieved.

The direct term will be defined as before, namely $D_0^s = -D_0^a = N(0)U/2$. Higher momentum channel terms are zero, and again, the direct term is antisymmetric because it satisfies the Pauli principle $D_0^{\uparrow\uparrow} = D_0^s + D_0^a = 0$.

The direct term plays an especially important role in the modeling here, because it is directly related to the s-wave scattering length a_s introduced earlier. Since a_s changes sign at the resonance, so will U: the sign denoting the attractively interacting regime or the negative one. The exact relation between these two quantities is simply [2]

$$U = \frac{8\pi\hbar^2}{m} a_s. \tag{6.4}$$

A distinction can be made between what is called the 'bare' scattering length, a_s in equation (6.4), and the 'effective' scattering length, which can be calculated through the whole machinery of the induced interactions. It is effective because it takes into account the whole many-body system on the two-particle scattering processes.

The effective s-wave scattering length, denoted as a_s^{eff}, is 'extracted' from the singlet scattering amplitude A_s^{eff}. This amplitude is defined in terms of the Fermi liquid parameters through use of the so called s-p approximation (for a discussion of this see [51]). The singlet scattering amplitude in this approximation is

$$A_s^{eff} = A_0^s - 3A_0^a - (A_1^s - 3A_1^a), \tag{6.5}$$

where

$$A_\ell^{s,a} = \frac{F_\ell^{s,a}}{1 + F_\ell^{s,a}/(2\ell+1)}. \tag{6.6}$$

Of course, A_s^{eff} is a unitless number. To extract a length from it, a_s^{eff}, it is written as

$$A_s^{eff} = N(0)a_s^{eff} = \frac{m^* k_F}{\pi^2\hbar^2} \cdot \frac{8\pi\hbar^2}{m^*} \cdot a_s^{eff} = \frac{8}{\pi}\frac{m^*}{m} k_F a_s^{eff}, \tag{6.7}$$

[2] One generally sees this written with a 4 in the numerator, not an 8 (see [77], page 37). This comes about here because of the definition of the direct term. a_s is literally the s-wave (singlet) scattering length, and the left hand side has to reflect that. In our language, the LHS is defined as $d^{singlet} = d_0^s - 3d_0^a = 2U$. Therefore, we pick up a factor of 2.

so that solving for the a_s^{eff} we get the required unit of length:

$$a_s^{eff} = \frac{\pi}{8}\frac{m}{m^*}\frac{1}{k_F}A_s^{eff}. \tag{6.8}$$

The procedure for the calculation should be clear. First, equations (6.2, 6.3) are solved self-consistently for $F_0^{s,a}$ at a certain value of U. Then calculate $F_1^{s,a}$ by projecting them out of these equations. The bare scattering length, equation (6.4), is immediately found and then the effective scattering amplitudes are computed using (6.5, 6.6, 6.8) to give the many-body result, a_s^{eff}. Finally, since the point is to look at the magnetic field dependence of the scattering lengths, (6.1) is used to go back and forth between U and B by plugging a_s from (6.4) into the LHS of (6.1) and solving for B as a function of U. Then one can compare $a_s(B)$ and $a_s^{eff}(B)$.

There are some important points to make about the algorithm described above. The first thing to note is the presence of the effective mass m^* in the effective terms. It does not appear in the bare terms, and in a many-body treatment of the interactions it should be somewhat important in the strongly interacting regime. We assume for its form the Fermi liquid relation: $m^*/m = 1 + F_1^s/3$.

Another point is the appearance of the Fermi momentum k_F. Since the systems being studied are quite dilute, away from the resonance this quantity plays a role. Fortunately, the experimental values for it are easily added into the calculation.

Finally, I note that both positive and negative values of U need to be considered when solving the induced interaction equations. In the prior chapter we were only interested in repulsive interactions. What is done here for attractive U is to follow the paramagnetic solution for positive U (see Figure 4.3) into the negative side and use those solutions. So, whereas on the positive side $F_0^s \sim U$ and $F_0^a \sim -1/2$ for large U, the opposite occurs on the negative side and $F_0^s \sim -1/2$ and $F_0^a \sim U/3$. (The values actually deviate slightly from these since we are not strictly in the local limit in this case.)

6.3 RPA and scattering lengths

Another many-body approach that has proved worthy in many instances is the random phase approximation (RPA). The RPA takes into account particle-hole scattering bubbles, consistent with the direct term of the induced interaction model, and represented diagrammatically as in Figure 6.5. However, it is well known that the scattering amplitudes in the RPA are not properly antisymmetrized, and thus leave out the crucial exchange fluctuations that dominate near the resonance.

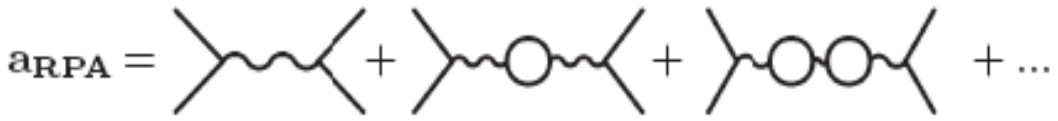

Figure 6.5 RPA scattering amplitude. The wiggly line is the bare scattering length a_s^{bare}, and the bubbles are the particle-hole propagators $\chi_0(q)$.

Consequently, the RPA predicts ground states that are spurious even before the Feshbach resonance is reached, on both sides. On the BEC side, RPA gives a ferromagnetic instability of the Stoner type in a metal, and the scattering amplitude diverges well before reaching the resonance, as will be seen below. On the BCS side, the result of RPA is phase separation of the particles and there will therefore be no superfluid pairing at all.

First I examine how RPA compares with the mean-field bare result (6.1). a_s^{bare} is antisymmetric because it is just the solution to the two-body scattering problem: but we stress that it does not take any quantum fluctuations into account. Figure 6.6 shows the typical behavior of these two quantities. For the purposes of this paper I only consider the BEC side, since it conveys all of the ideas mentioned above. I will go over this first plot in detail. The scattering length is measured in Bohr radii which is common in the literature, and the x-axis is presented as the distance from the Feshbach resonance B_0. Far away from the resonance (smaller U), the molecular bound state is very strong, and two-body processes are the dominant scattering mechanisms in the system. Agreement between the curves is both expected and observed, however, as the resonance is approached, the RPA scattering length diverges well before a_s^{bare} does. Therefore, we conclude that the RPA is insufficient in the vicinity of the resonance. In fact, a simple RPA approach to the study of the

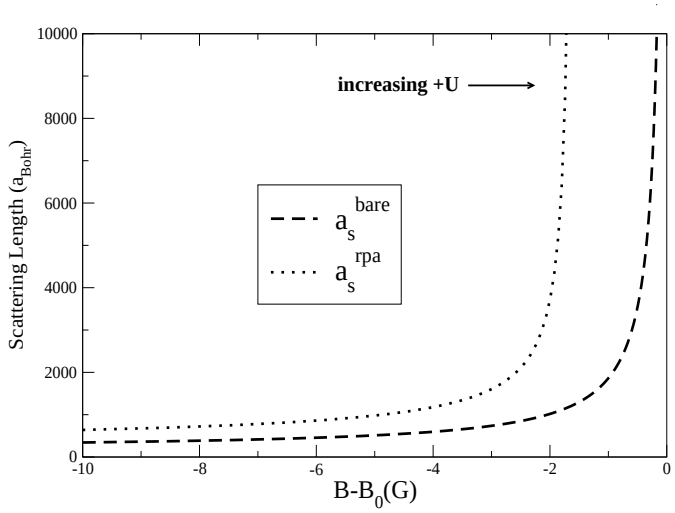

Figure 6.6 The RPA (dotted) and bare (dashed) scattering lengths as a function of magnetic field on the BEC side. The Feshbach resonance is at $B = B_0 = 0$. The driving term U is labeled just to point out that larger and larger values are needed to get nearer to the resonance.

collective modes in the system seems to come to the same conclusion in the strongly interacting regime [78].

All three scattering lengths on the BEC side are shown in Figure 6.7. The effective one (solid line), calculated with all of the tools of the induced interactions, and a characteristic k_F, does not diverge at the resonance. It approaches a constant value as seen, and differs greatly from a_s^{bare}. Back away from resonance, the RPA and effective lengths converge as they should, again because the fluctuations that the induced interactions calculate are greatly reduced in the dilute limit. The divergence is thus suppressed, in a somewhat similar fashion to what happened in the last chapter, i.e., when the induced term is turned off, a divergence appears. Turning off the induced term here would give back the RPA result, 'recovering' the divergence.

The data of a typical scattering length experiment is plotted in Figure 6.8, along with the theoretical bare and effective scattering lengths. Notice that both the BEC and the BCS sides are explored, so that the negative U solutions of the induced interactions are used.

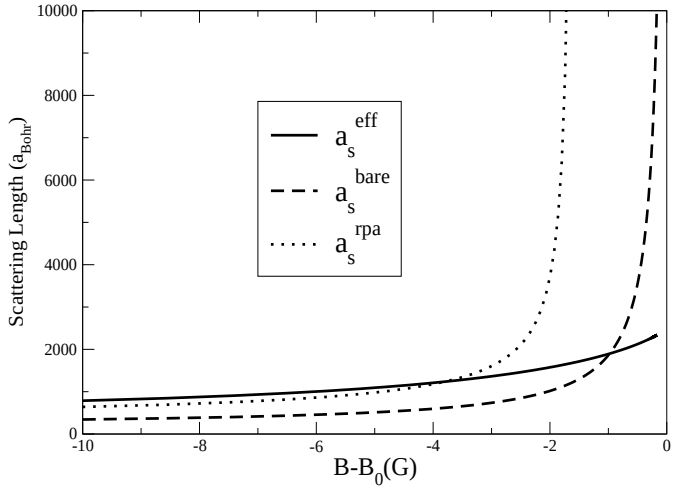

Figure 6.7 The three theoretical scattering lengths on the BEC side of the Feshbach resonance.

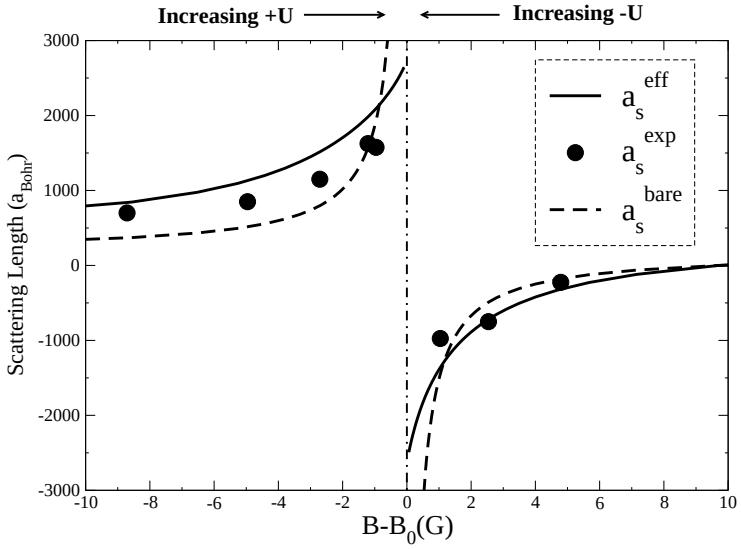

Figure 6.8 Theoretical and experimental scattering lengths. The experimental data [11] is for ^{40}K with a density of $5.8 \times 10^{13}/cm^3$, which gives a $k_F = 1.2 \times 10^{-3}\dot{A}^{-1}$. The vertical line marks the Feshbach resonance.

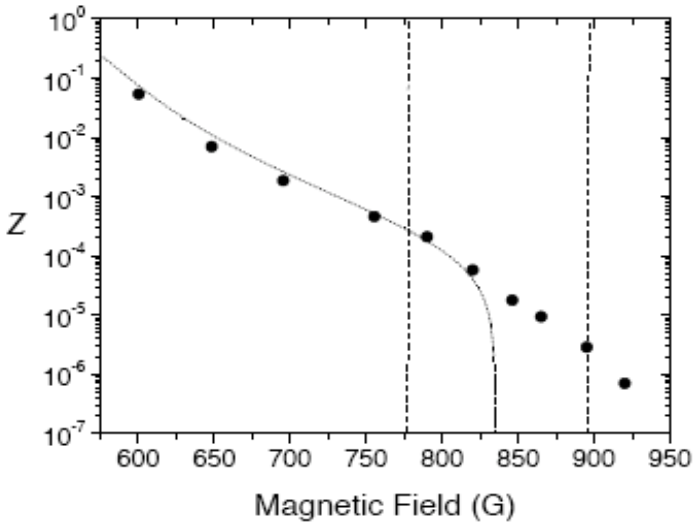

Figure 6.9 Plot taken from [12] that demonstrates the finite density of molecules through a broad Feshbach resonance in ^6Li. The lines are described in the text.

It is clear that the experimental data and a_s^{eff} do not diverge and agree quite well near resonance, which is where this theory is most relevant. The magnitudes are similar, and the discrepancy between them might be explained by other many-body effects that we are not able to calculate at present. In fact, the experimental points have about 50% error bars [11].

6.4 Binding energy

In the last section it was shown that the effective and experimental scattering lengths remain finite at resonance, whereas the bare scattering length diverges. This has important consequences for the binding energy E_b of the singlet molecular bound state on the BEC side because they are related, as mentioned before, by $E_b = -\hbar^2/ma_s^2$. Therefore, a non-divergent scattering length implies a finite binding energy, which is relevant because recently it has been observed that there are a finite number of molecules that persist throughout a broad Feshabach resonance, and even survive shortly into the BCS side before exponentially disassociating [12].

To get a clear picture of this, the data is reproduced in Figure 6.9. The y-axis can be regarded as the fraction or density of bound molecules in the system as a function of B-field. The resonance is predicted to be at $B \sim 850(G)$, and the vertical dashed lines mark the strongly interacting regime

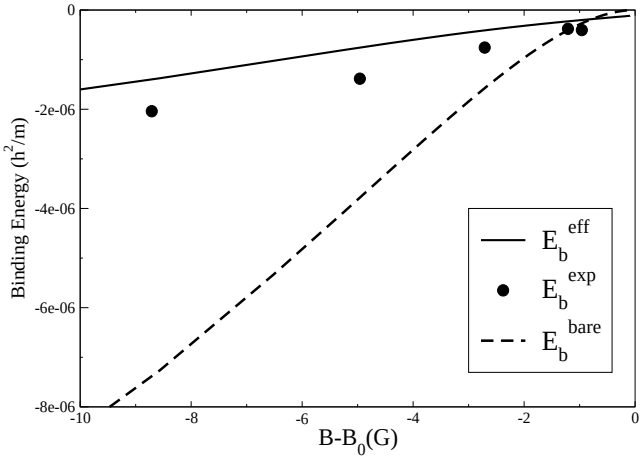

Figure 6.10 Binding energies in units shown. The experimental ones are calculated using the data for the scattering length [11] and then plugged into the bare binding energy formula given in the text.

(where $k_F|a| > 1$). A portion of the BCS side is shown, and one sees that the molecules do not completely disappear right before the resonance on the BEC side. The dotted line is a theoretical curve of an exact two-body calculation in a coupled channels model. It works well in the weak regime, but predicts *no* molecules at resonance. The molecules 'live' right up to the resonance, through it, and into the attractive side briefly.

Our theory predicts weakly bound molecules at the resonance since the scattering amplitude is finite. Since there are molecules in the vicinity, we argue that they do not play an important role in the physics. First of all, even though there is a finite density of molecules at resonance, it is a very small number $\sim 10^{-5}$ that is insufficient to alter the calculations appreciably. Therefore, the dominant contributions in the scattering near the resonance are the fluctuations and exchange of the fermions, which is all that is required to suppress the divergence. In the language of the atomic physicists, the open channel dominates over the closed channel, and therefore a single channel model is quite appropriate for the properties we are interested in.

Finally, the effective binding energy from the theory is compared with the experimental data. The effective binding energy equation is somewhat modified from the bare case to take into account the effective mass, i.e., $E_b^{eff} = -\hbar^2/m^* a_s^{eff^2}$. The results are shown in Figure 6.10. Near resonance there is good agreement between the effective and experimental values since they are both finite. Even away from resonance the slopes are very similar in magnitude.

6.5 Pairing and superfluidity on the BCS side

Recently, the apparent verification of superfluidity in the alkali atom gases of ^6Li [79, 80, 81, 9] and ^{40}K [82] has been achieved. It is generally believed that a superfluid occuring on the BCS side will pair in the s-wave singlet channel because of the diluteness of the systems. However, by the same arguments used throughout this chapter, namely that the inclusion of many-body effects gives more angular momentum channels for the fermions to sample, it follows that it is quite possible that a p-wave triplet could be formed at some low temperature because of the fluctuation effects.

This possibility can be quantitatively studied in the framework derived for the induced interactions, and in a way we already have looked at the singlet pairing on the BCS side. We calculate scattering amplitudes and subsequently pairing amplitudes and can also look at different channels in the s-p approximation. The singlet scattering amplitude is given by (6.5), and the triplet one similarly can be shown to be

$$A_t^{eff} = A_0^s + A_0^a - A_1^s - A_1^a. \tag{6.9}$$

The solutions on the BCS side can again be generated to study the pairing amplitudes as a function of the magnetic field, as in Figure 6.11. The plot shows the BCS side, where the y-axis is the Fermi momentum times the appropriate scattering length, given in the legend. The triplet amplitude (dotted line) is of course negative, attractive, and of the same order of magnitude as the singlet amplitude. Therefore, at low enough temperature, a triplet superfluid and a singlet superfluid are expected to compete. The critical temperature at which one might expect a superfluid transition in the ℓ^{th} momentum channel T_c^ℓ is given by the relation

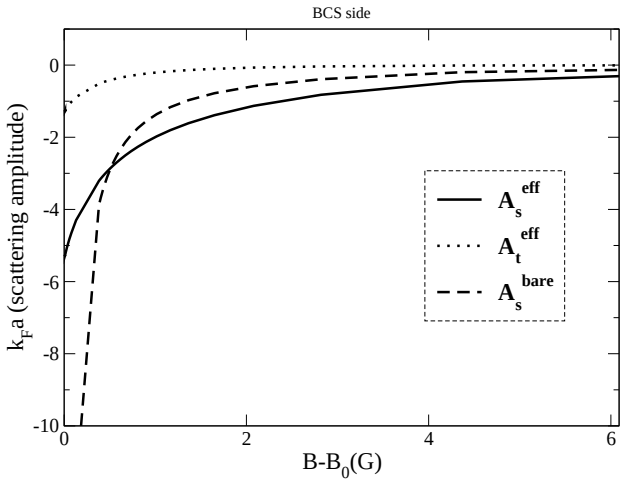

Figure 6.11 Scattering amplitudes in the singlet and triplet channels, and also the bare s-wave scattering length for comparison.

$$T_c^{(\ell)} \approx T_F e^{\frac{4(2\ell+1)}{\lambda_\ell}}, \tag{6.10}$$

where λ_ℓ is the the pairing strength (scattering amplitude) in the ℓ^{th} channel. We find by carrying out this quick calculation that $T_c^s \approx 0.7T_F$ and $T_c^t \approx 0.2T_F$ for the singlet and triplet respectively. A recent experiment that studies radial breathing modes finds that there are two discontinuities at two separate temperatures in the damping rates of the frequencies of these modes [80], which the authors claim are transitions into the superfluid. The temperatures they measure are $T_{c1} \approx 0.8T_F$ and $T_{c2} \approx 0.3T_F$. It will take further experimental investigation to determine if these two temperatures are in fact two separate superfluid transitions, and we are not claiming that this is the case. Our prediction is that the p-wave could occur at an experimentally accessible temperature, and should compete with the singlet superfluid.

6.6 A Levinson theorem

One final amusing result accidentally came out of the study of these systems in the induced interaction model. It turns out that in the local limit ($\ell = 0$ Fermi liquid parameters), one recovers

Levinson's theorem. Levinson's theorem connects the phase shift of the scattering event to the number of bound states expected (at $k = 0$) resulting from the scattering. It can be written for the ℓ^{th} channel as

$$\delta^{\ell}(k = 0) = \pi n_{\ell}, \tag{6.11}$$

so that n_ℓ, the number of bound states in the ℓ^{th} channel, can be determined from the calculation of the phase shift. The phase shift in our case is written $\delta^{\ell=0} = (k_F a_s^- - k_F a_s^+)$, where the $\pm$ denotes immediately above or below the resonance (threshold) respectively (unitary limit).

In the local limit, this calculation can be done analytically. Starting from equation (6.8), one can write

$$k_F a_s^{eff} = \frac{\pi}{8} A_s^{eff}, \tag{6.12}$$

since the effective mass is the same as the mass. In the local limit, the scattering amplitudes are related trivially to the Fermi liquid parameters as $A_0^{s,a} = F_0^{s,a}/(1 + F_0^{s,a})$ and from Pauli it is true that $A_0^s = -A_0^a$. Therefore, $A_s^{eff} = A_0^s - 3A_0^a = -4A_0^a$. On the BEC side for infinite U, $F_0^a \to -1/2$ and so $A_0^a \to -1$. Thus, $A_s^{eff} = 4$, and from (6.12), the 'phase' on the BEC side is $\pi/2$.

On the BCS side, when U is infinite, $F_0^a \to \infty$, $A_0^a \to 1$, and then $A_s^{eff} = -4$. The phase on this side is thus $-\pi/2$. The phase shift is the difference of these, or π, so Levinson (6.11) says there must be one bound state, which in fact there is on the BEC side. Some discussion of the many-body implications of Levinson's theorem are given in [83], and the results found above are shown in Figure 6.12 upon approaching the resonance, from the numerical calculation.

6.7 Conclusions

In this chapter I presented a method in the induced interaction language for calculating the scattering length and pairing amplitudes in atomic Fermi systems. It was found that the non-divergence of the experimental scattering length is handled by the theory quite well. The theory

also predicts a strong possibility of the existence of p-wave triplet superfluidity on the attractive side of the resonance. These results are due to the inclusion of strong exchange fluctuation effects.

Future work includes a study of the collective modes (sound) of the systems using the same general framework. The collective modes are important because they indicate phase transitions and are currently under intense experimental investigation. Another calculation will be carried out to determine the behavior of the specific heat across the resonance which is also being investigated [81]. Many new predictions are expected to come from this theoretical approach.

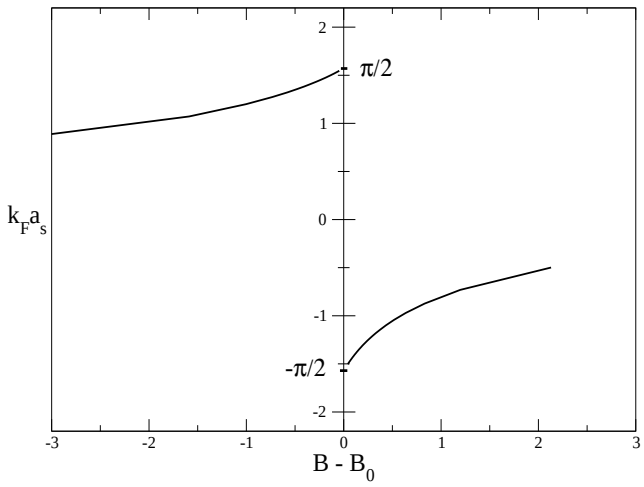

Figure 6.12 The phase shift in the local limit of the induced interactions at the Feshbach resonance, defined as $k_F a_s$.

LIST OF REFERENCES

[1] Shick, A. B. and Pickett, W. E., Magnetism, spin-orbit coupling, and superconducting pairing in UGe_2. *Phys. Rev. Lett.*, **86**, 300 (2001).

[2] Tateiwa, N., Kobayashi, T. C., Hanazono, K., Amaya, K., Haga, Y., Settai, R., and Onuki, Y., Pressure-induced superconconductivity in a ferromagnet UGe_2. *J. Phys. Cond. Matt.*, **13**, L17 (2001).

[3] Pfleiderer, C. and Huxley, A. D., Pressure dependence of the magnetization in the ferromagnetic superconductor UGe_2. *Phys. Rev. Lett.*, **89**, 147005 (2002).

[4] Pfleiderer, C., Uhlarz, M., Hayden, S. M., Vollmer, R., v. Löhneysen, H., Bernhoeft, N. R., and Lonzarich, G. G., Coexistence of superconductivity and ferromagnetism in the d-band metal $ZrZn_2$. *Nature (London)*, **412**, 58 (2001).

[5] Blagoev, K. B., Engelbrecht, J. R., and Bedell, K. S., S-wave superconductivity in weak ferromagnetic metals. *Phil. Mag. Lett.*, **78**, 169 (1998).

[6] Kotegawa, H., Harada, A., Kawasaki, S., Kawasaki, Y., Kitaoka, Y., Haga, Y., Yamamoto, E., Onuki, Y., Itoh, K., Haller, E., and Harima, H., Evidence for uniform coexistence of ferromagnetism and unconventional superconductivity in UGe_2: A ^{73}Ge-NQR study under pressure. *J. Phys. Soc. Jpn.*, **74**, 705 (2005).

[7] Blagoev, K. B., Engelbrecht, J. R., and Bedell, K. S., Effect of ferromagnetic spin correlations on superconductivity in ferromagnetic metals. *Phys. Rev. Lett.*, **82**, 133 (1999).

[8] Lashley, J., Fisher, R., Flouquet, J., Hardy, F., Huxley, A., and Phillips, N., Ambient-pressure specific heat of single-crystal UGe_2. *to be published* (2005).

[9] Zwierlein, M., Abo-Shaeer, J., Schirotzek, A., Schunck, C., and Ketterle, W., Vortices and superfluidity in a strongly interacting Fermi gas. *Nature*, **435**, 1047 (2005).

[10] Regal, C. A., Ticknor, C., Bolton, J. L., and Jin, D. S., Creation of ultracold molecules from a Fermi gas of atoms. *Nature*, **424**, 47 (2003).

[11] Regal, C. and Jin, D., Measurement of positive and negative scattering lengths in a Fermi gas of atoms. *Phys. Rev. Lett.*, **90**, 230404 (2003).

[12] Partridge, G., Strecker, K., Kamar, R., Jack, M., and Hulet, R., Molecular probe of pairing in the BEC-BCS crossover. *cond-mat/0505353* (2005).

[13] Bardeen, J., Cooper, L., and Schrieffer, J., Theory of superconductivity. *Phys. Rev.*, **108**, 1175 (1957).

[14] Ginzburg, V. L., Ferromagnetic superconductors. *Sov. Phys. JETP*, **4**, 153 (1957).

[15] Saxena, S. S., Argarwal, P., Ahllan, K., Grosche, F. M., Hasselwimmer, R. K. W., Steiner, M. J., Pugh, E., Walker, I. R., Julian, S. R., Monthoux, P., Lonzarich, G. G., Huxley, A., Shelkin, I., Braithwaite, D., and Flouquet, J., Superconductivity on the border of itinerant-electron ferromagnetism in UGe_2. *Nature (London)*, **406**, 587 (2000).

[16] Aoki, D., Huxley, A., Ressouche, E., Braitwaite, D., Flouquet, J., Brison, J.-P., Lhotel, E., and Paulsen, C., Coexistence of superconductivity and ferromagnetism in $URhGe$. *Nature (London)*, **413**, 613 (2001).

[17] Mathur, N., Grosche, F., Julian, S., Walker, I., Freye, D., Hasselwimmer, R., and Lonzarich, G., Magnetically mediated superconductivity in heavy fermion compounds. *Nature (London)*, **394**, 39 (1998).

[18] London, F., *Superfluidity*. Wiley, New York (1950).

[19] London, F., *Superfluids vol. I*. Wiley, New York (1950).

[20] Ginzburg, V. L. and Landau, L. D., To the theory of superconductivity. *Zh. Eksperim. i. Teor. Fiz.*, **20**, 1064 (1950).

[21] Clogston, A. M., Upper limit for the critical field in hard superconductors. *Phys. Rev. Lett.*, **9**, 266 (1962).

[22] Berk, N. F. and Schrieffer, J. R., Effect of ferromagnetic spin correlations on superconductivity. *Phys. Rev. Lett.*, **17**, 433 (1966).

[23] Doniach, S. and Engelsberg, S., Low-temperature properties of nearly ferromagnetic Fermi liquids. *Phys. Rev. Lett.*, **17**, 750 (1966).

[24] Enz, C. P. and Matthias, B. T., P-state pairing and the ferromagnetism of $ZrZn_2$. *Science*, **201**, 828 (1978).

[25] Fay, D. and Appel, J., Coexistence of p-state superconductivity and itinerant ferromagnetism. *Phys. Rev. B*, **22**, 3173 (1980).

[26] Hertz, J. A., Quantum critical phenomena. *Phys. Rev. B*, **14**, 1165 (1976).

[27] Millis, A. J., Effect of a nonzero temperature on quantum critical points in itinerant fermion systems. *Phys. Rev. B*, **48**, 7183 (1993).

[28] Abrikosov, A. A., *Fundamentals of the Theory of Metals*. North Holland, New York (1988).

[29] Lei, X. L., Ting, C. S., and Birman, J. L., Theoretical investigation of superconductivity in itinerant ferromagnets. *Phys. Rev. B*, **29**, 2483 (1984).

[30] Wang, Z., Mao, W., and Bedell, K., Superconductivity near itinerant ferromagnetic quantum criticality. *Phys. Rev. Lett.*, **87**, 257001 (2001).

[31] Roussev, R. and Millis, A. J., Quantum critical effects on transition temperature of magnetically mediated p-wave superconductivity. *Phys. Rev. B*, **63**, 140504 (2001).

[32] Monthoux, P. and Lonzarich, G. G., Magnetically mediated superconductivity in quasi-two and three dimensions. *Phys. Rev. B*, **63**, 054529 (2001).

[33] Kirkpatrick, T. R., Belitz, D., Vojta, T., and Narayanan, R., Strong enhancement of superconducting T_c in ferromagnetic phases. *Phys. Rev. Lett.*, **87**, 127003 (2001).

[34] Kirkpatrick, T. R. and Belitz, D., Coexistence of ferromagnetism and superconductivity. *Phys. Rev. B*, **67**, 024515 (2003).

[35] Machida, K. and Ohmi, T., Phenomenological theory of ferromagnetic superconductivity. *Phys. Rev. Lett.*, **86**, 850 (2001).

[36] Walker, M. B. and Samokhin, K. V., Model for superconductivity in ferromagnetic $ZrZn_2$. *Phys. Rev. Lett.*, **88**, 207001 (2002).

[37] Karchev, N. I., Blagoev, K. B., Bedell, K. S., and Littlewood, P. B., Coexistence of superconductivity and ferromagnetism in ferromagnetic metals. *Phys. Rev. Lett.*, **86**, 846 (2001).

[38] Suhl, H., Simultaneous onset of ferromagnetism and superconductivity. *Phys. Rev. Lett.*, **87**, 167007 (2001).

[39] Abrikosov, A. A., Superconductivity due to ferromagnetically ordered localized spins. *J. Phys. Cond. Matt.*, **13**, L943 (2001).

[40] Bauer, E. D., Dickey, R. P., Zapf, V. S., and Maple, M. B., Coexistence of superconductivity and ferromagnetism in polycrystalline UGe_2. *J. Phys. Cond. Matt.*, **13**, L759 (2001).

[41] Cuoco, M., Gentile, P., and Noce, C., Coexistence of ferromagnetism and singlet superconductivity via kinetic exchange. *Phys. Rev. Lett.*, **91**, 197003 (2003).

[42] Huxley, A., Sheikin, I., Ressouche, E., Kernavanois, N., Braithwaite, D., Calemczuk, R., and Flouquet, J., UGe_2: A ferromagnetic spin-triplet superconductor. *Phys. Rev. B*, **63**, 144519 (2001).

[43] Watanabe, S. and Miyake, K., Coupled CDW and SDW fluctuations as an origin of anomalous properties of ferromagnetic superconductor UGe_2. *cond-mat/0110492* (2001).

[44] Jackiewicz, J., Lashley, J., Bedell, K. S., Blagoev, K. B., and Littlewood, P., SDW/CDW phase transition in weak ferromagnetic metals. *in preparation* (2005).

[45] Mackenzie, A. P., Haselwimmer, R. K. W., Tyler, A. W., Lonzarich, G. G., Mori, Y., Nishizaki, S., and Maeno, Y., Extremely strong dependence of superconductivity on disorder in Sr_2RuO_4. *Phys. Rev. Lett.*, **80**, 161 (1998).

[46] Tinkham, M., *Introduction to Superconductivity*. McGraw-Hill, New York (1996).

[47] Sandeman, K. G., Lonzarich, G. G., and Schofield, A. J., Ferromagnetic superconductivity driven by changing Fermi surface topology. *Phys. Rev. Lett.*, **90**, 167005 (2003).

[48] Flouquet, J. and Buzdin, A., Ferromagnetic superconductors. *Physics World*, **January 2002** (2002).

[49] Matsuda, T. D., Ikeda, S., Haga, Y., Yamamoto, E., Hedo, M., Uwatoko, Y., and Ōnuki, Y., Electrical resistivity of single-crystal $URhGe_2$ under high pressure. *J. Phys. Cond. Mat.*, **15**, S2019 (2003).

[50] Engelbrecht, J. R. and Bedell, K. S., Robustness of a local fermi liquid against ferromagnetism and phase separation. *Phys. Rev. Lett.*, **74**, 4265 (1995).

[51] Baym, G. and Pethick, C., *Landau Fermi Liquid Theory*. Wiley, New York (1991).

[52] Jackiewicz, J. A., Blagoev, K. B., and Bedell, K. S., A model for coexistent superconductivity and ferromagnetism. *Phil. Mag.*, **83**, 3247 (2003).

[53] Shen, R., Zheng, Z., Liu, S., and Xing, D., Breakdown of the coexistence of spin-singlet superconductivity and itinerant ferromagnetism. *Phys. Rev. B*, **67**, 024514 (2003).

[54] Shen, R., Zheng, Z., and Xing, D., Is there coexistence of itinerant ferromagnetism and s-wave superconductivity? *Phys. Rev. Lett.*, **91**, 069702 (2003).

[55] Dahal, H., Jackiewicz, J., and Bedell, K. S., Physical properties of superconducting-ferromagnetic coexistent system. *Phys. Rev. B*, **71**, 184518 (2005).

[56] Nevidomskyy, A. H., Coexistence of ferromagnetism and superconductivity near quantum phase transition: the Heisenberg to Ising-type crossover. *cond-mat/0412247* (2004).

[57] Dahal, H., Jackiewicz, J., and Bedell, K. S., Pairing symmetry signatures of T_1 in superconducting ferromagnets. *cond-mat/0507212* (2005).

[58] Joglekar, Y. N. and MacDonald, A. H., Comment on "Coexistence of superconductivity and ferromagnetism in ferromagnetic metals". *Phys. Rev. Lett.*, **92**, 199705 (2004).

[59] Blagoev, K. B., Bedell, K. S., and Littlewood, P. B., Blagoev et al. reply. *Phys. Rev. Lett.*, **92**, 199706 (2004).

[60] Brazovskii, S., Phase transition of an isotropic system to a nonuniform state. *Sov. Phys. JETP*, **41**, 85 (1975).

[61] Schmalian, J. and Turlakov, M., Quantum phase transitions of magnetic rotons. *Phys. Rev. Lett.*, **93**, 036405 (2004).

[62] Babu, S. and Brown, G., Quasiparticle interaction in liquid ^3He. *Ann. Phys.*, **78**, 1 (1973).

[63] Ainsworth, T., Bedell, K., Brown, G., and Quader, K., A model for paramagnetic Fermi systems. *Journal of Low Temp. Phys.*, **50**, 319 (1983).

[64] Quader, K., Bedell, K., and Brown, G., Strongly interacting fermions. *Phys. Rev. B*, **36**, 156 (1987).

[65] Jackiewicz, J. and Bedell, K. S., Quantum fluctuation driven first order phase transition in weak ferromagnetic metals. *Phil. Mag.*, **85**, 1755 (2005).

[66] Sanchez-Castro, C., Bedell, K. S., and Wiegers, S., Spin-polarized Fermi liquids: Applications to liquid ^3He. *Phys. Rev. B*, **40**, 437 (1989).

[67] Petkova, P., unpublished.

[68] Callen, H., *Thermodynamics*. Wiley, New York (1960).

[69] Chubukov, A., Finkel'stein, A., Haslinger, R., and Morr, D., First-order superconducting transition near a ferromagnetic quantum critical point. *Phys. Rev. Lett.*, **90**, 077002 (2003).

[70] Beltiz, D., Kirkpatrick, T., and Vojta, T., First order transitions and multicritical points in weak itinerant ferromagnets. *Phys. Rev. Lett.*, **82**, 4707 (1999).

[71] Kirkpatrick, T. and Belitz, D., Nature of the quantum phase transition in clean itinerant Heisenberg ferromagnets. *Phys. Rev. B*, **67**, 024419 (2003).

[72] Kim, J. G., Choi, Y.-H. S., Lee, E. K., and Lee, S., Temperature-dependent free-electron susceptibility for one, two, and three dimensions. *Phys. Rev. B*, **59**, 3661 (1999).

[73] Aso, N., Motoyama, G., Uwatoko, Y., Ban, S., Nakamura, S., Nishioka, T., Homma, Y., Shiokawa, Y., Hirota, K., and Sato, N., Stoner gap in the superconducting ferromagnet UGe_2. *cond-mat/0505266* (2005).

[74] Gaudio, S., Jackiewicz, J., and Bedell, K. S., Many-body exchange effects close to the s-wave Feshbach resonance: Is a triplet superfluid possible? *cond-mat/0505306* (2005).

[75] Ketterle, W., Nobel lecture: When atoms behave as waves: Bose-Einstein condensation and the atom laser. *Rev. Mod. Phys.*, **74**, 1131 (2002).

[76] Greiner, M., Regal, C., and Jin, D., Emergence of a molecular Bose-Einstein condensate of a Fermi gas. *Nature*, **426**, 537 (2003).

[77] Abrikosov, A., Gorkov, L., and Dzyaloshinskii, I., *Methods of Quantum Field Theory In Statistical Physics*. Dover, New York (1963).

[78] Bruun, G., Collective modes of trapped Fermi gases in the normal phase. *Phys. Rev. A*, **63**, 043408 (2001).

[79] Kinast, J., Hemmer, S., Gehm, M., Turlapov, A., and Thomas, J., Evidence for superfluidity in a resonantly interacting Fermi gas. *Phys. Rev. Lett.*, **92**, 150402 (2004).

[80] Kinast, J., Turlapov, A., and Thomas, J., Two transitions in the damping of a unitary Fermi gas. *cond-mat/0502507* (2005).

[81] Kinast, J., Turlapov, A., Thomas, J. E., Chen, Q., Stajic, J., and Levin, K., Heat capacity of a strongly interacting Fermi gas. *Science*, **307**, 1296 (2005).

[82] Regal, C., Greiner, M., and Jin, D., Observation of resonance condensation of Fermionic atom pairs. *Phys. Rev. Lett.*, **92**, 040403 (2004).

[83] Brand, J., Haring, I., and Rost, J., Levinson-like theorem for scattering from a Bose-Einstein condensate. *Phys. Rev. Lett.*, **91**, 070403 (2003).

[84] Press, W. H., Teukolsky, S. A., Vetterling, W. T., and Flannery, B. P., *Numerical Recipes in C*. Cambridge University Press (1992).

Appendix A: Newton-Rhapson method for solving multidimensional nonlinear equations

I would like to give a brief synopsis of the method used to solve the coupled equations of the mean field model from Chapter 3. The equations to be solved at finite temperature are (3.19) and (3.20), and the zero temperature equations are (3.23) and (3.25). A formal account of this method is given in section 9.6 of Press *et al.* [84], and the code used for this calculation is given in Appendix B.

The basic problem is to find the zeroes of 2 nonlinear functions and two variables:

$$\begin{aligned} F_1(M_0, \Delta_0) &= 0 \\ F_2(M_0, \Delta_0) &= 0, \end{aligned} \tag{A.1}$$

where F_1 and F_2 are the two mean field equations, and the subscripts on the order parameters denote the values which give the zeroes of the two functions. In general, this may not be a very complex problem, but in our case there are 2 difficulties. One is that the same variables occur in both equations, and thus need to be solved self-consistently. The other is that both of the equations are integral equations (actually, in the zero temperature solution, there is another difficulty which will be mentioned below).

Let the entire set of solutions be given by a vector $\mathbf{x}$, which of course is not known initially. Denoting also the functions F_1 and F_2 by a vector $\mathbf{F}$, a Taylor expansion is computed about an initial guess $\mathbf{x}$, and one may write

$$\mathbf{F}(\mathbf{x} + \delta\mathbf{x}) = \mathbf{F}(\mathbf{x}) + \mathbf{J} \cdot \delta\mathbf{x}, \tag{A.2}$$

where the quadratic corrections are ignored, and $\mathbf{J}$ is the Jacobian given by

$$J_{ij} = \frac{\partial F_i}{\partial x_j}. \tag{A.3}$$

So, for example, $J_{11} = \partial F_1/\partial M$, $J_{12} = \partial F_1/\partial \Delta$, etc. To approach closer to the zeroes of the functions, one sets $\mathbf{F}(\mathbf{x} + \delta\mathbf{x}) = 0$ and what remains is the matrix equation $\mathbf{J} \cdot \delta\mathbf{x} = -\mathbf{F}$, which

I solve by a simple matrix inversion to find the $\delta\mathbf{x}$. This solution is then added to the initial guess $\mathbf{x}_{new} = \mathbf{x}_{initial} + \delta\mathbf{x}$, to find a value which is closer to the correct answer, and the process is repeated with $\mathbf{x}_{new}$ until convergence. The code given in the appendix follows this procedure.

I mentioned above that in the zero temperature case there is a small complexity that had to be considered. It comes from the fact that in equation (3.25), the order parameters are not only in the integrand, but also in the limits of integration (see also (3.22)). Thus, when calculating the Jacobian partial derivatives, the limits come into play.

I owe the solution of this problem to Professor Andrzej Herczynski, who thankfully somewhere, in one of his old books, found an identity that I could use. The problem for this specific case is

$$F = \int_{p_F^-(M,\Delta)}^{p_F^+(M,\Delta)} f(p,\Delta)d^3p, \tag{A.4}$$

and we want to find the partial derivative, say, $\partial F/\partial\Delta$. The answer can be written as

$$\frac{\partial F}{\partial\Delta} = f(p_F^+)\frac{\partial p_F^+}{\partial\Delta} + \int_{p_F^-}^{p_F^+}\frac{\partial f}{\partial\Delta}d^3p - f(p_F^-)\frac{\partial p_F^-}{\partial\Delta}. \tag{A.5}$$

Thanks Andrzej.

Appendix B: Code for solutions of M and Δ at finite temperatures

The code that I have written and reproduced below gives solutions for the magnetization and superconducting order parameters from reference [37], equations (6) and (7), given in this thesis as (3.19) and (3.20). These are two coupled, nonlinear, integral equations that had to be solved self-consistently at finite temperatures, with variations in the coupling constants J and g. The method used to do this is a variant of the Newton-Rhapson method which can be found in reference [84], and a short description is above in Appendix A. At very low temperatures, this code encounters a divergence because of the Fermi functions, and there I use a zero temperature code. The intermediate temperatures not handled by either code are found by extrapolation.

```
#include <iostream.h>
#include <iomanip.h>
#include <math.h>
#include <fstream.h>

ofstream outfleet ("piece-coex2.dat");

double const PI = acos(-1.0);
double const a = pow(10,-4);
double const b = pow(10,-2);
double const c = pow(10,-2);

double delta; double m;
double J; double g;
double cutoff;
double T;

double sech(double y)
{
  return 1.0/cosh(y);
}

double Ealpha(double p)  //this is beta Ealpha / 2
{
  return (4.0*PI*PI*a*J*m + sqrt((p*p-1.0)*(p*p-1.0)+b*b*delta*delta))*0.5/c/T;
}
```

```
double Ebeta(double p) //this is beta Ebeta / 2
{
  return (4.0*PI*PI*a*J*m - sqrt((p*p-1.0)*(p*p-1.0)+b*b*delta*delta))*0.5/c/T;
}

double com(double p) //this is what appears inside the root
{
  double x = (p*p-1.0)*(p*p-1.0) + b*b*delta*delta;
  return pow(x, -0.5);
}

//*********************************
//these are the functions that occur from the various terms in the jacobian
//the partial derivatives of the 2 F's with respect to M and DELTA ********************

double f1(double p)
{
  return p*p*(sech(Ealpha(p))*sech(Ealpha(p)) + sech(Ebeta(p))*sech(Ebeta(p)));
}

double f2(double p)
{
  return p*p*(sech(Ebeta(p))*sech(Ebeta(p)) - sech(Ealpha(p))*sech(Ealpha(p)))*com(p);
}

double f3(double p)
{
  return p*p*(tanh(Ealpha(p)) - tanh(Ebeta(p)))*com(p);
}

double f4(double p)
{
  return p*p*(sech(Ealpha(p))*sech(Ealpha(p)) + sech(Ebeta(p))*sech(Ebeta(p)))*com(p)*co
}

double f5(double p)
{
  return p*p*(tanh(Ealpha(p)) - tanh(Ebeta(p)))*com(p)*com(p)*com(p);
}

double f6(double p)
```

```
{
  return p*p*(tanh(Ealpha(p)) + tanh(Ebeta(p)));
}
//*********  END of the 6 'functions' ********************************


// Jacobian elements ###########################################################

double dF1_dm(double value1)
{
  return 1.0 - J*0.25/c/T*value1;
}

double dF1_ddelta(double value2)
{
  return b*b*delta/16.0/PI/PI/a/c/T*value2;
}

double dF2_dm(double value2)
{
  return 5.0*g*delta*a*J/c/T*value2;
}

double dF2_ddelta(double value3, double value4, double value5)
{
  return 1.0 - 2.5*g/PI/PI*value3 - 1.25*g*b*b*delta*delta/pow(PI,2)/c/T*value4
    + 2.5*g*b*b*delta*delta/pow(PI,2)*value5;
}

// End Jacobian elements#########################################################

// Integration Voids ***********************************************************

void integral1(double *value1)
{
  const int n = 100000;
  double dp = (1.0+cutoff - (1.0-cutoff))/(n+1.0);
  double z = 0.0;
  double p = 0.0;

  p = 1.0 - cutoff;
  z = 1/3*f1(p) + 4/3*f1(p+dp) + 1/3*f1(p+2*dp);
```

```
  for (int k=1; k<=n; k++)
    {
      p = p + dp;
      z = z + 1/3*f1(p) + 4/3*f1(p+dp) + 1/3*f1(p+2*dp);
    }
  z = z*dp;

  *value1 = z;
  // cout<<z<<endl;
}

void integral2(double *value2)
{
  const int n = 100000;
  double dp = (1.0+cutoff - (1.0-cutoff))/(n+1.0);
  double z = 0.0;
  double p = 0.0;

  p = 1.0 - cutoff;
  z = 1/3*f2(p) + 4/3*f2(p+dp) + 1/3*f2(p+2*dp);
  for (int k=1; k<=n; k++)
    {
      p = p + dp;
      z = z + 1/3*f2(p) + 4/3*f2(p+dp) + 1/3*f2(p+2*dp);
    }
  z = z*dp;

  *value2 = z;
  // cout<<z<<endl;
}

void integral3(double *value3)
{
  const int n = 100000;
  double dp = (1.0+cutoff - (1.0-cutoff))/(n+1.0);
  double z = 0.0;
  double p = 0.0;

  p = 1.0 - cutoff;
  z = 1/3*f3(p) + 4/3*f3(p+dp) + 1/3*f3(p+2*dp);
  for (int k=1; k<=n; k++)
    {
```

```
      p = p + dp;
      z = z + 1/3*f3(p) + 4/3*f3(p+dp) + 1/3*f3(p+2*dp);
    }
  z = z*dp;

  *value3 = z;
  // cout<<z<<endl;
}

void integral4(double *value4)
{
  const int n = 100000;
  double dp = (1.0+cutoff - (1.0-cutoff))/(n+1.0);
  double z = 0.0;
  double p = 0.0;

  p = 1.0 - cutoff;
  z = 1/3*f4(p) + 4/3*f4(p+dp) + 1/3*f4(p+2*dp);
  for (int k=1; k<=n; k++)
    {
      p = p + dp;
      z = z + 1/3*f4(p) + 4/3*f4(p+dp) + 1/3*f4(p+2*dp);
    }
  z = z*dp;

  *value4 = z;
  // cout<<z<<endl;
}

void integral5(double *value5)
{
  const int n = 100000;
  double dp = (1.0+cutoff - (1.0-cutoff))/(n+1.0);
  double z = 0.0;
  double p = 0.0;

  p = 1.0 - cutoff;
  z = 1/3*f5(p) + 4/3*f5(p+dp) + 1/3*f5(p+2*dp);
  for (int k=1; k<=n; k++)
    {
      p = p + dp;
      z = z + 1/3*f5(p) + 4/3*f5(p+dp) + 1/3*f5(p+2*dp);
```

```
    }
  z = z*dp;

  *value5 = z;
  // cout<<z<<endl;
}

void integral6(double *value6)
{
  const int n = 100000;
  double dp = (1.0+cutoff - (1.0-cutoff))/(n+1.0);
  double z = 0.0;
  double p = 0.0;

  p = 1.0 - cutoff;
  z = 1/3*f6(p) + 4/3*f6(p+dp) + 1/3*f6(p+2*dp);
  for (int k=1; k<=n; k++)
    {
      p = p + dp;
      z = z + 1/3*f6(p) + 4/3*f6(p+dp) + 1/3*f6(p+2*dp);
    }
  z = z*dp;

  *value6 = z;
  //  cout<<z<<endl;
}
// End integration Voids ***************************************************

// Other voids ^^^^^^^^^^^^^^^^^^^^^^^^^^^^^^^^^^^^^^^^^^^^^^^^^^^^^^^^^^^^^^

void EvaluationF(double F[2], double *value3, double *value6)
{
  F[0] = m - 1/8.0/a/pow(PI,2)**value6;
  F[1] = 1.0*delta - 2.5*g*delta/pow(PI,2)**value3;
}

void Jacobian(double Jac[2][2], double *value1, double *value2, double *value3, double *
      double *value5)  //the jacobian from newton's method
{
  Jac[0][0] = dF1_dm(*value1);
  Jac[0][1] = dF1_ddelta(*value2);
  Jac[1][0] = dF2_dm(*value2);
```

```
  Jac[1][1] = dF2_ddelta(*value3, *value4, *value5);
}

void JacobianInverse(double Jac[2][2], double JacInv[2][2])
{
  double det = Jac[0][0]*Jac[1][1] - Jac[0][1]*Jac[1][0];

  JacInv[0][0] = Jac[1][1]/det;
  JacInv[0][1] = -1.0*Jac[0][1]/det;
  JacInv[1][0] = -1.0*Jac[1][0]/det;
  JacInv[1][1] = Jac[0][0]/det;
}
// End other voids^^^^^^^^^^^^^^^^^^^^^^^^^^^^^^^^^^^^^^^^^^^^^^^^^^^^^^^^^^^^^^^^^^^^^^

int main()
{

  double value1;
  double value2;
  double value3;
  double value4;
  double value5;
  double value6;
  double F[2];
  double Jac[2][2];
  double JacInv[2][2];
  double x[2];
  double y[2];
  double dT;
  double dJ;
  double dg;
  double error = 0.0001;

  J = 1.001;
  g = 2.95;
  cutoff = 0.15;
  T =  0.07;

  dT = 0.01;
  dJ = 0.001;
  dg = 0.05;
```

```
  double initmag = 10.0;
  double initdelta = 1.0;

  x[0] = initmag;      //m
  x[1] = initdelta;       //delta

  while(T<=22.37)
    {
      cout<<"m=  "<<x[0]<<"  delta=  "<<x[1]<<"   T=  "<<T<<"  J=  "<<J<<
"  g=  "<<g<<"  cut=  "<<cutoff<<endl;

      for (int k=1; k<=1000; k++)
{
  m     = x[0];
  delta = x[1];

  integral1(&value1);
  integral2(&value2);
  integral3(&value3);
  integral4(&value4);
  integral5(&value5);
  integral6(&value6);
  EvaluationF(F, &value3, &value6);
  Jacobian(Jac, &value1, &value2, &value3, &value4, &value5);
  JacobianInverse(Jac, JacInv);

  y[0] = -1.0*(JacInv[0][0]*F[0] + JacInv[0][1]*F[1]);
  y[1] = -1.0*(JacInv[1][0]*F[0] + JacInv[1][1]*F[1]);

  x[0] = x[0] + y[0];
  x[1] = x[1] + y[1];

  cout<<"m=  "<<x[0]<<"  delta=  "<<x[1]<<"   T=  "<<T<<
    "  J=  "<<J<<"  g=  "<<g<<endl;

  if (x[1]<0.0) x[1] = 0.0;
  if (x[0]<0.0) x[0] = 0.0;

  if(sqrt(y[0]*y[0] + y[1]*y[1]) < error) break;
}

      cout<<"*************************************************"<<endl;
```

```
      outfleet<<T<<"   "<<x[1]<<"   "<<x[0]<<"  "<<tinkham<<"   "
      <<deltazero<<endl;

      // J = J + dJ;       //choose which parameter needs to be incremented:T,J, or g.
      T = T + dT;
      // g = g + dg;
    }

}
```

Appendix C: Analytical derivation of the specific heat

In this appendix I would like to go through in some detail the relatively simple calculation which leads to equation (3.33). I will follow the general procedure of the calculation found in Tinkham [46] on pages 64-65, however, there is an added feature because of the magnetism.

As given by (3.32), the electronic specific heat is

$$C = T\frac{dS}{dT}. \tag{C.1}$$

In this case, there are two species of quasiparticles (α and β fermions), and the entropy S can be given in a general way by

$$S = -k_B \sum_p \left[n_p^\alpha \ln n_p^\alpha + (1-n_p^\alpha)\ln(1-n_p^\alpha) + n_p^\beta \ln n_p^\beta + (1-n_p^\beta)\ln(1-n_p^\beta) \right]. \tag{C.2}$$

As a reminder, note that

$$n_p^{\alpha,\beta} = \frac{1}{e^{\beta E_p^{\alpha,\beta}}+1}; \qquad E_p^{\alpha,\beta} = \frac{JM}{2} \pm \sqrt{\xi_p^2 + \Delta^2}. \tag{C.3}$$

After plugging everything into (C.1) and regrouping terms, we have[1]

$$C = \frac{1}{T}\sum_p \left[\frac{dn_p^\alpha}{d\beta} \ln \frac{n_p^\alpha}{1-n_p^\alpha} + \frac{dn_p^\beta}{d\beta} \ln \frac{n_p^\beta}{1-n_p^\beta} \right], \tag{C.4}$$

which follows the first line of equation (3.56) in [46]. I will now define the temperature derivatives of the distribution functions since there are many terms within them that we have to treat carefully. The tricky terms are

$$\frac{dn_p^{\alpha,\beta}}{d\beta} = -\frac{e^{\beta E_p^{\alpha,\beta}} \left(E_p^{\alpha,\beta} + \beta \frac{dE_p^{\alpha,\beta}}{d\beta} \right)}{\left(e^{\beta E_p^{\alpha,\beta}} + 1 \right)^2} = -\frac{1}{\beta}\frac{dn_p^{\alpha,\beta}}{dE_p^{\alpha,\beta}} \left(E_p^{\alpha,\beta} + \beta \frac{dE_p^{\alpha,\beta}}{d\beta} \right), \tag{C.5}$$

[1] Please do not be confused by the somewhat contradictory notation with the use of β. It generally just denotes the one species of quasiparticle as a superscript, but it also may mean inverse temperature, as $\beta = 1/k_B T$ in the equations above. It should be obvious from the context which is which.

where the last term can be rewritten as

$$\frac{dE_p^{\alpha,\beta}}{d\beta} = \frac{J}{2}\frac{dM}{d\beta} \pm \frac{1}{2E_p}\frac{d\Delta^2}{d\beta}. \tag{C.6}$$

A valid approximation one can make is to ignore the temperature-dependence of the magnetization near the superconducting critical temperature, which is evident from Figure 3.8(c). However, it turns out that later in the calculation, the $dM/d\beta$ terms are cancelled anyway, so I will set them to zero here. Another relation I will use which re-expresses the $\ln$ terms in (C.4) is simply

$$\ln \frac{n_p^{\alpha,\beta}}{1 - n_p^{\alpha,\beta}} = -\beta E_p^{\alpha,\beta}. \tag{C.7}$$

Using (C.5, C.6, and C.7), the full coexistent specific heat from (C.4) can be written as

$$C_{SC-FM} = -\frac{1}{T}\sum_p \left[\frac{dn_p^\alpha}{dE_p^\alpha} E_p^\alpha \left(E_p^\alpha + \frac{\beta}{2E_p}\frac{d\Delta^2}{d\beta} \right) + \frac{dn_p^\beta}{dE_p^\beta} E_p^\beta \left(E_p^\beta + \frac{\beta}{2E_p}\frac{d\Delta^2}{d\beta} \right) \right]. \tag{C.8}$$

We have arrived at the last line of (3.56) in Tinkham's book. Now to determine the jump in the specific heat, we need to look at the behavior right above T_c and right below T_c, where T_c refers to the superconducting transition, not the magnetic one.

C.1 $T = T_c^+$

At this temperature, the system is in the normal ferromagnetic state where $\Delta = d\Delta^2/d\beta = 0$ and $E_p^{\alpha,\beta} = JM/2 \pm |\xi_p|$. The normal state specific heat is given by

$$C_N = -\frac{1}{T}\sum_p \left[\frac{dn_p^\alpha}{d\left(\frac{JM}{2} + |\xi|\right)} \left(\frac{JM}{2} + |\xi|^2 \right)^2 + \frac{dn_p^\beta}{d\left(\frac{JM}{2} - |\xi|\right)} \left(\frac{JM}{2} - |\xi|^2 \right)^2 \right]. \tag{C.9}$$

Changing the sum over p to an integral over energy, and working out the derivative in the integrand, this becomes

$$C_N = \frac{N(0)}{T}\int d\xi \left[\beta x^{+2} \frac{e^{\beta x^+}}{\left(e^{\beta x^+} + 1\right)^2} + \beta x^{-2} \frac{e^{\beta x^-}}{\left(e^{\beta x^-} + 1\right)^2} \right], \tag{C.10}$$

where $x^{\pm} = JM/2 \pm |\xi|$ and $N(0) = m^* p_F/\pi^2$. Multiplying top and bottom by a β and making a change of variables to $z^{\pm} = \beta x^{\pm} = z$, we get two identical integrals which gives a factor of 2 when added, and the final integral is

$$C_N = \frac{2N(0)}{\beta^2 T} \int_{-\infty}^{+\infty} dz \frac{z^2 e^z}{(e^z+1)^2}. \tag{C.11}$$

The value of this integral is $\pi^2/3$, so that the final normal state specific heat is $C_N = \frac{2\pi^2}{3} N(0) k_B^2 T$, which is equation (3.57) of [46]. I must note that the 'normal' state here actually has background ferromagnetism, and at temperatures near zero, the density of states expression changes (see eq.(28) in ref.[37]). Near T_c however, the effects of the magnetization are buried in the effective mass since the gap is nearly zero.

C.2 $T = T_c^-$

At temperatures right below T_c, $\Delta \to 0$, but now $d\Delta^2/d\beta \neq 0$, and this term is partly what gives rise to the specific heat jump. We can now work with the change in specific heat upon going through the transition given as $\Delta C = C_{SC} - C_N$, where again it is understood that the magnetization is finite, and important. Keeping in mind the limits and subtracting the normal state contribution (C.9) from (C.8), it follows that

$$\Delta C = -\frac{\beta}{2T} \frac{d\Delta^2}{d\beta} \sum_p \left[\frac{x^+}{|\xi|} \frac{dn_p^\alpha}{dx^+} - \frac{x^-}{|\xi|} \frac{dn_p^\alpha}{dx^-} \right]. \tag{C.12}$$

One observes that $dn_p^\alpha/dx^+ = dn_p^\alpha/d|\xi|$ and $dn_p^\beta/dx^- = -dn_p^\beta/d|\xi|$. Now the integral form can be used once again, and several of the terms can be calculated right away to give

$$\Delta C = -\frac{\beta}{4T} \frac{d\Delta^2}{d\beta} JM \left[-\frac{4N(0)}{JM} + N(0) \int \frac{d\xi}{\xi} \left(\frac{dn^\alpha}{d\xi} + \frac{dn^\beta}{d\xi} \right) \right]. \tag{C.13}$$

The first term of this equation is the BCS specific heat jump, given in Tinkham by equation (3.58). Therefore, the rest must be due to the magnetization which is unique to this coexistent model. Let us for the moment only consider the terms within the parentheses.To cast these terms into a more tractable form, the first step is to note that

$$\frac{dn^{\alpha,\beta}}{d\xi} = \mp\beta \frac{e^{\beta(JM/2\pm\xi)}}{\left(e^{\beta(JM/2\pm\xi)}+1\right)^2}. \tag{C.14}$$

The next step is to then to get a common denominator of the fraction by multiplying the denominators in (C.14) together. The result is somewhat messy, but the trick is to note that in the mess, a simple relation is used, e.g.,

$$e^{\beta\left(\frac{JM}{2}-\xi\right)}+1 = e^{\frac{\beta}{2}\left(\frac{JM}{2}-\xi\right)}\left(e^{\frac{\beta}{2}\left(\frac{JM}{2}-\xi\right)}+e^{-\frac{\beta}{2}\left(\frac{JM}{2}-\xi\right)}\right). \tag{C.15}$$

This simplifies everything into hyperbolic functions and what remains of the terms in parentheses is

$$\frac{1}{4}\frac{\cosh^2\frac{\beta}{2}\left(\frac{JM}{2}-\xi\right)-\cosh^2\frac{\beta}{2}\left(\frac{JM}{2}+\xi\right)}{\cosh^2\frac{\beta}{2}\left(\frac{JM}{2}+\xi\right)\cdot\cosh^2\frac{\beta}{2}\left(\frac{JM}{2}-\xi\right)} = \frac{1}{4}sech^2\frac{\beta}{2}\left(\frac{JM}{2}+\xi\right)-\frac{1}{4}sech^2\frac{\beta}{2}\left(\frac{JM}{2}-\xi\right). \tag{C.16}$$

Plugging this result into (C.13) and rearranging a bit gives equation (3.33) that we set out to derive.